

ABSTRACT

LAGRANGIAN KINEMATICS IN THE PLANE-STRAIN EXTRUSION OF
A REAL METAL

by

William Herbert Ginman

Co-Chairmen: Robert M. Caddell, Thomas A. Despres

This dissertation presents a kinematic investigation of the direct cold plane-strain extrusion process. The deformations are described in terms of the differences in the path lines for the flow of 6061-0 aluminum through tapered dies as compared to an ideal flow. Actual deformations are also compared to the deformations predicted by the slip line theory.

The deformations are determined experimentally by examining the changes in a grid pattern that is marked on the halves of a split billet before extrusion. Two different die angles and reductions in area are investigated. A measure of the rotationality of the aluminum flow field is determined, and an analytical model is created for the actual velocity field. The deformations predicted by the analytical model of the actual velocity field are compared to the actual deformations.

LAGRANGIAN KINEMATICS IN THE PLANE-STRAIN EXTRUSION OF
A REAL METAL

by

William Herbert Ginman

A dissertation submitted in partial fulfillment
of the requirements for the degree of
Doctor of Philosophy
(Mechanical Engineering)
in The University of Michigan
1974

Doctoral Committee:

Professor Robert M. Caddell, Co-Chairman
Professor Thomas A. Despres, Co-Chairman
Professor Anthony G. Atkins
Professor Joseph Datsko
Professor William F. Hosford
Professor Tsung Y. Na

Engin
UMR
1515

ACKNOWLEDGEMENTS

I wish to express my appreciation to the people and organizations which contributed to the success of this research:

To Professors Robert M. Caddell and Thomas A. Despres, Co-Chairmen of my doctoral dissertation committee, for their guidance and valuable advice.

To the members of my doctoral dissertation committee, Professors Anthony G. Atkins, Joseph Datsko, William F. Hosford, and Tsung Y. Na for their interest, participation and cooperation.

To members of the Mechanical Engineering Instrument Shop, James Allen, William Galer, Donald Haidys and Arnold Solstad.

To the National Science Foundation and the Horace H. Rackham School of Graduate Studies Graduate Student Research Fund for financial support of this project.

To the Mechanical Engineering Department for providing computer time.

To my wife and family for their faith in me.

TABLE OF CONTENTS

	Page
ACKNOWLEDGEMENTS.....	iii
LIST OF TABLES.....	vi
LIST OF FIGURES.....	vii
LIST OF SYMBOLS.....	x
 Chapter	
I. INTRODUCTION.....	1
Object of Investigation.....	4
Historical Review.....	4
Scope of Investigation.....	10
II. EXPERIMENTAL PROCEDURE, TEST EQUIPMENT, AND EXPERIMENTAL RESULTS.....	13
Introduction.....	13
Test Equipment.....	15
Extrusion Billet.....	20
Lubrication.....	22
Grid System.....	24
Experimental Results.....	26
Experimental Capabilities.....	31
III. ANALYTICAL PROCEDURE FOR MODELING REAL METAL DEFORMATION FIELDS IN DIRECT TWO DIMENSIONAL COLD EXTRUSION OF ALUMINUM.....	34
Introduction and Assumptions.....	34
Reference Frame and Normalization.....	35
Reference Continuum.....	42
Path Lines, Time Lines, and Strain Ellipses.....	45
Computer Implemented Model of Perfect Fluid Deformation Field in the Selected Reference Frame.....	52
Comparison of the Perfect Fluid Deformation Field with the Real Metal Deformation Field.....	60
Modeled Real Metal Path Lines.....	63
Modeled Real Metal Velocity Fields.....	75
Computer Implemented Model of Real Metal Deformation Fields.....	81
Slip Line Generated Deformation Fields.....	85

Chapter	Page
IV. COMPARISON AND DISCUSSION OF MODELED DEFORMATION FIELDS AND EXPERIMENTAL RESULTS.....	88
Comparison of the Perfect Fluid Deformation Fields with the Real Metal Deformation Fields.....	88
Modeled Real Metal Velocity Fields.....	95
Comparison of Perfect Fluid Deformation Fields with Modeled Real Metal Deformation Fields.....	96
Comparison of Modeled Real Metal Deformation Fields with Real Metal Deformation Fields.....	98
Comparison of Slip Line Deformation Fields with Real Metal Deformation Fields.....	102
Perturbations of the Developed Model for the Real Metal Deformation Fields.....	105
Potential Flow and Plane-Strain Extrusion	110
Conclusions	110
Future Applications	111
APPENDIX A. SELECTED PROPERTIES OF 6061-0 ALUMINUM.....	112
Hardness.....	112
Yield Strength Versus Percent Cold Work.....	113
Tensile Behavior.....	113
Modeled Tensile Behavior.....	113
Anisotropic Behavior.....	114
APPENDIX B. RAM LOADS AND VELOCITIES DURING THE DIRECT TWO DIMENSIONAL COLD EXTRUSION PROCESS.....	115
APPENDIX C. THE SCHWARZ CHRISTOFFEL TRANSFORMATION FOR THE GENERAL QUADRILATERAL WITH TWO VERTICES EXTENDED, OF THE EXTENDED VERTICES, ONE CONTAINS A SOURCE AND THE OTHER CONTAINS AN EQUAL SINK.....	118
APPENDIX D. COMPUTER AIDED ANALYSES AND PLOTTING PROGRAMS.....	127
General Purpose Subprograms.....	127
Orthogonal Curvilinear Coordinate Computation and Plot....	136
Perfect Fluid Deformation Field Computation and Plot.....	138
Experimental Modeling Coefficients Computation.....	146
Experimental Function Definition Using a Cubic Spline Fit.....	148
Modeled Real Metal and Perfect Fluid Velocity Hodograph Plots.....	152
Modeled Real Metal Deformation Field Computation and Plot.....	154
BIBLIOGRAPHY.....	162

LIST OF TABLES

	Page
TABLE I	GEOMETRIES INVESTIGATED.....11
TABLE II	PRESS SPECIFICATIONS.....15
TABLE III	MARKING EQUIPMENT SPECIFICATIONS.....20
TABLE IV	LUBRICANT SPECIFICATIONS.....23
TABLE V	FORESHORTENING RATIOS.....31
TABLE VI	EXPERIMENTAL POINTS FOR DETERMINING MODEL COEFFICIENTS.....72
TABLE VII	MODEL COEFFICIENTS.....73
TABLE VIII	EXPERIMENTAL POINTS FOR DETERMINING MODEL COEFFICIENTS.....92
TABLE IX	MODEL COEFFICIENTS.....93
TABLE X	SELECTED MECHANICAL PROPERTIES 6061-0 ALUMINUM.....112
TABLE XI	YIELD STRENGTH VERSUS PERCENT COLD WORK.....113
TABLE XII	FIN THICKNESSES.....117

LIST OF FIGURES

Figure	Page
1. Two dimensional extrusion through tapered dies.....	10
2. Exposed internal view of the extrusion machine.....	16
3. Die pieces for altering extrusion geometry.....	17
4. Essential elements of ram travel control.....	18
5. Clamps on assembled extrusion machine.....	19
6. Extrusion billet. Material 6061-0 aluminum.....	21
7. Lubrication for extrusion billet.....	23
8. Real metal deformation field. Material 6061-0 aluminum.....	25
9. Real metal deformation field.....	28
10. Real metal deformation field.....	29
11. Real metal deformation field.....	30
12. Orthogonal curvilinear coordinate systems showing two different spacings.....	36
13. Physical plane.....	37
14. The Schwarz Christoffel upper half plane where point D is extended and contains sink.....	38
15. The rationalizing plane. Point C is extended.....	39
16. The complex potential plane where p_2 equal to a constant is a streamline and p_1 equal to a constant is a potential line. Points A and D are extended.....	40
17. The velocity plane. Point C is extended.....	44
18. Images of an array of perfect fluid path lines in the perfect fluid velocity plane.....	44
19. Schematic distortion of ellipse showing important parameters...	47
20. Local coordinate systems ζ and μ ; Intermediate transformation coordinate system η	49

Figure	Page
21. Incremental array of perfect fluid path lines used to define the time function in the physical plane.....	54
22. Example array of $z(I,J)$ and $z(I,K)$ positions.....	57
23. Perfect fluid deformation field.....	58
24. Perfect fluid deformation field superimposed on the real metal deformation field.....	61
25. Schematic representation of perfect fluid potential lines, real metal path lines, and perfect fluid path lines in the z , p , and r planes.....	64
26. Schematic representation of the difference between the perfect fluid path lines and the real metal path lines ΔP	68
27. Schematic synthesis of function A	69
28. Schematic synthesis of function ΔP_m	69
29. Model coefficients versus real metal path line.....	74
30. Images of an array of modeled real metal path lines in the modeled velocity plane.....	79
31. Images of an array of modeled real metal path lines in the perfect fluid velocity plane.....	79
32. Modeled real metal deformation field.....	84
33. Slipline field and velocity hodograph.....	86
34. Deformation field of a perfectly plastic solid.....	86
35. Perfect fluid deformation field superimposed on the real metal deformation field.....	89
36. Perfect fluid deformation field superimposed on the real metal deformation field.....	90
37. Orthogonal curvilinear coordinate system.....	91
38. Model coefficients versus real metal path line, r_2	94
39. Images of an array of modeled real metal path lines in the modeled real metal velocity plane v	95
40. Images of an array of modeled real metal path lines in the perfect fluid velocity plane q	96

Figure	Page
41. Perfect fluid deformation field superimposed on the modeled real metal deformation field.....	97
42. Perfect fluid deformation field superimposed on the modeled real metal deformation field.....	98
43. Modeled real metal deformation field superimposed on the real metal deformation field.....	100
44. Modeled real metal deformation field superimposed on the real metal deformation field.....	101
45. Slip line deformation field superimposed on the real metal deformation field.....	102
46. Slip line deformation field superimposed on the real metal deformation field.....	103
47. Slip line deformation field superimposed on the real metal deformation field.....	104
48. Modification 1, model coefficients versus real metal path line r_2	106
49. Modeled deformation field based on Modification 1 superimposed on the modeled deformation field developed in Chapter III.....	107
50. Modification 2, model coefficients versus real metal path line, r_2	108
51. Modeled deformation field based on Modification 2 superimposed on the modeled deformation field developed in Chapter III.....	109
52. True stress versus true plastic strain.....	114
53. Ram loads and velocities during the direct cold two dimensional extrusion of 6061-0 aluminum.....	115
54. Physical plane z	119
55. The Schwarz Christoffel upper half plane.....	121
56. The complex potential plane.....	122
57. The velocity plane, q	122
58. The rationalizing plane, s	124
59. Two additional equivalent physical configurations for the Schwarz Christoffel transformation.....	126

LIST OF SYMBOLS

<u>Symbol</u>	<u>Description</u>
A	Model coefficient in Equation 71
A	Defined by Equation 71
A_0, A_1	Differential areas at times t_0 and t_1 , respectively
a	Model coefficient in Equation 71
a_T	First transformation constant
B	Model coefficient in Equation 72
B	Defined by Equation 72
b	Model coefficient in Equation 72
b_T	Second transformation constant
c	Constant defined by Equation 46
c_1	Skew symmetry coefficient in Equation 71
c_2	Skew symmetry coefficient in Equation 72
\vec{D}	Displacement vector
d_1, d_2	Semi-major diameter and semi-minor diameter, respectively
\vec{e}	Vector describing strain ellipse
\vec{e}_{nq}	Unit vector normal to a perfect fluid path line
\vec{e}_q	Unit vector tangent to a perfect fluid path line
H	Outlet to inlet dimension ratio
H_i	Inlet dimension to extrusion dies
H_o	Outlet dimension to extrusion dies
I	Index identifying a particular path line
i	The imaginary constant from complex variables ($\sqrt{-1}$)

it	An integer derived from time function
J	Index identifying a particular position on a path line
K	Constant in plastic stress, strain equation
K_1, K_2	Constants in Equation 51
K_3	Constant in Equation 52
\vec{k}_1, \vec{k}_2	Unit vectors in the z plane
\vec{k}_3	Unit vector normal to the z plane
L	Effective foreshortening ratio
L_0, L_1	Differential lengths at times t_0 and t_1 , respectively
M	Integer
\vec{l}_1, \vec{l}_2	Unit vectors in the ζ local coordinate system
\vec{m}_1, \vec{m}_2	Unit vectors in the η intermediate transformation coordinate system
N	Integer
n	Constant in plastic stress strain equation
\vec{n}_1, \vec{n}_2	Unit vectors in the μ local coordinate system
p	Potential plane
p_1, p_2	Dimensions in the potential plane or the potential function and the stream function, respectively
p'_1 (I)	Selected starting position on a perfect fluid path line
$p_2(1)$	Perfect fluid path line that coincides with a real metal path line in the limit up and down stream from the tapered die section
ΔP	Represents the difference in position in the complex potential plane between the real metal path line and a perfect fluid path line

ΔP_m	The model for ΔP
ΔP_{max}	The maximum deviation
ΔP_{min}	The minimum deviation
q	Velocity plane
q_1, q_2	Dimensions in velocity plane for velocity components of a perfect fluid particle
\vec{q}	Perfect fluid velocity vector
R	Reduction in area
\vec{R}	Position vector
\vec{R}_0	Position when time is zero
r	Modeled real metal path plane
r_1, r_2	Dimensions in the modeled real metal plane or the potential function and the modeled real metal path line function, respectively
r'_1 (I)	Selected starting position on a modeled real metal path line
S	Distance
s	Rationalizing plane
s_1, s_2	Dimensions in rationalizing plane
t	Time
Δt	Time interval
V	Magnitude of velocity
V_0, V_1	Magnitudes of velocities at times t_0 and t_1 , respectively
\vec{V}_i	Inlet velocity
\vec{V}	Velocity vector
V_A	Normalized velocity in the limit up stream from the tapered die section
\vec{v}	Modeled real metal velocity vector

v_1, v_2	Components of the modeled real metal velocity vector
w	Schwarz Christoffel upper half plane
w_1, w_2	Dimensions in Schwarz Christoffel upper half plane
x	Dimension
x_1, x_2	Dimensions in plane of measurement for billet
x ref.	Reference dimension
z	Physical plane
z_1, z_2	Dimensions in the physical plane

Greek Letters

<u>Symbol</u>	<u>Description</u>
α	Model coefficient in Equation 71
β	Model coefficient in Equation 72
Γ	Constant in Equation 47
γ	Semi-die angle
δ	Differential length
ϵ	True plastic strain
ϵ_1, ϵ_2	Maximum and minimum principal natural strains
ζ	Local coordinate system
ζ_1, ζ_2	Dimensions in local coordinate system
η	Intermediate transformation coordinate system
η_1, η_2	Dimensions in intermediate transformation coordinate system
θ	Constant in Equation 47
θ	Angle between x_1 axis and path line

θ_w	Angle in the w plane using polar representation
μ	Local coordinate system
μ_1, μ_2	Dimensions in local coordinate system
E	Constant in Equation 47
ρ	Density
σ	Tensile stress
σ_w	Stress in the x direction
σ_y	Stress in the y direction
\uparrow	Angle in the ζ local coordinate system
ϕ	Shear angle
ψ	Angle between maximum principle strain axis and path line
$\vec{\omega}$	Vorticity vector

Chapter I

INTRODUCTION

This dissertation presents a kinematic investigation that begins to answer a question that arose during a graduate seminar on metal forming. This discussion may have transpired as follows:

Professor: Today's topic will be slip line theory as applied to non-homogeneous plane strain deformations of rigid-perfectly plastic isotropic solids.

Questioning Student: From our studies of the mechanical properties of metals, we learned that for many annealed materials such as brass, aluminum and low carbon steel, the yield strength could change by a factor of two within 10 percent cold work. How well does the slip line theory apply to forming these materials, considering that a perfectly plastic material has a constant yield strength?

Professor: Given the differences between the more common metals and the perfectly plastic solid, slip line theory has proved to be a surprisingly useful concept that has led to a better understanding of many metal forming processes. But before answering your question, let us review some properties of slip lines. Slip lines can be considered curvilinear coordinates that coincide with the directions of the planes acted upon by the maximum shear stresses. When substituting (1) expressions for the stresses into the stress equilibrium equations,

$$\frac{\partial \sigma_x}{\partial x} + \frac{\partial \tau_{yx}}{\partial y} = 0 = \frac{\partial \sigma_y}{\partial y} + \frac{\partial \tau_{xy}}{\partial x}$$

an expression for the yield strength is included. If the shear yield strength is a constant, the partial differentiations in the stress equilibrium equations are performed easily, resulting in the commonly accepted slip line relations. These relations are derived from kinetical considerations together with the material model for the perfectly plastic solid. The kinetical expression of stress equilibria and selection of a curvilinear coordinate system coincident with the maximum shear stress planes are equally valid and useful when analyzing deformations of work hardenable materials. However the material models employed for work hardening metals usually require the deformation histories. Deformation histories imply the ability to identify material particles and determine the strain state as a function of time along the particle's path during the forming process.

Questioning Student: Wouldn't this introduce enormous complexities when trying to perform the indicated partial differentiations from the stress equilibrium equations?

Professor: Precisely. A general problem statement for this slip line approach for work hardenable materials has been made,⁽²⁾ but solutions are difficult.

Student: It appears that a somewhat general kinematical model that is stated in terms of a particle's path could be useful when trying to analyze the forming of work hardening materials from this generalized slip line approach.

Professor: Perhaps a research project studying the kinematical relations of a specific metal forming process in terms of the

particles' path line would be fruitful.

As a result of this discussion, the extrusion process was selected for investigation and presentation in this dissertation.

The parameters completely characterizing extrusion can be classified as belonging to two groups:

- (1) The parameters characterizing the extrusion process.
- (2) The parameters characterizing the extruded product.

The forces, energies, powers required, etc. for the process are directly related to extruded material. The hardness distribution, inhomogeneity in the yield strength, residual stresses, etc. in extruded product are directly related to the extruded material. The analysis of the extrusion process, therefore, depends on the accuracy of the material model.

The analysis of the problem can be thought to have three parts:

1. the kinematical part
2. the kinetical part
3. the material model part which relates the kinematics to the kinetics for the extrusion problem.

For material models that depend on the previous deformation, a particle's deformation history must be part of the analysis. The particle's path line must be determined and the deformation of a particle as a function of time relative to the path line is required to meet this historical requirement. Prandtl⁽³⁾ points out that this type of problem statement has been a traditional source of difficulty.

The kinematical relationships of a flow can be described from two points of view:

- (1) The Eulerian point of view, which is to describe the flow in the neighborhood of a fixed point in space.

- (2) The Lagrangian point of view, which is to identify a neighborhood of particles at some time, t_0 , and describe the neighborhood and its path through space as a function of time.

OBJECT OF INVESTIGATION

The object of this investigation is to provide a kinematic modeling method for the flow of a work hardenable material during the extrusion process; the method must be Lagrangian and give path lines, velocity fields, and deformations relative to path lines as a function of time for various die geometries.

Flow fields can be classified as either irrotational or rotational, the flow of a real metal in an extrusion process being rotational. A Lagrangian measure of this rotationality is defined by the modeling method and the rotationality is characterized by this measure.

In addition, the kinematic modeling method must be adaptable to further work relating the kinetics and kinematics through a material model that depends on deformation history.

HISTORICAL REVIEW

The extrusion process is studied using the analytic principles of plasticity. With the exception of shop practice, the history of the analytic investigations in plasticity started with M. H. Tresca in 1864, when he^(4,5) attempted to answer the question, "What is the stress state under which a metal begins to plastically deform?" The maximum shear stress theory for the yielding of ductile metals was the result of his investigation. Saint-Venant,⁽⁶⁾ in applying this theory to the problem of determining stresses in a partly plastic cylinder, recognized there is no one-to-one relationship between stress and plastic strain. Levy,⁽⁷⁾ adopting a Saint-Venant concept of an ideal plastic material, proposed three dimensional relations between stress and plastic strain

rate, while Guest⁽⁸⁾ investigated the yielding of materials under combined stresses obtaining results broadly agreeing with Tresca's maximum shear stress theory. These are the major accomplishments in the 19th Century in attempting to develop a plasticity theory for ductile metals.

By the beginning of the 20th Century, the directions for future investigations had been charted:

- (1) Refinement of the yield criteria.
- (2) Continued material studies.
- (3) Differentiating between small scale and large scale deformations.
- (4) Solutions to specific problems or approximate solutions to specific problems.

von Mises⁽⁹⁾ proposed a yield criterion that is analytically more tractable than Tresca's, with experimental data usually bounded by these two yield criteria. Hencky⁽¹⁰⁾ interpreted von Mises' yield criterion to be a maximum distortion energy theory, while Nadai⁽¹¹⁾ interpreted this yield criterion in terms of octahedral shear stresses. Although Lode's⁽¹²⁾ experimental results were in agreement with von Mises to a first approximation, Taylor and Quinney⁽¹³⁾ examined some of the deviations in Lode's experimental work and determined that real metals have regular deviations from the von Mises theory. Yoshimura and Takeda⁽¹⁴⁾ in their paper propose a theory that is an extension of the von Mises' theory of plasticity, for isotropic work-hardening materials. This recent theory accounts for some of the regular deviations as observed by Taylor and Quinney, however, it doesn't include the effects of temperature or strain rate which can be important at high temperatures and strain rates. This is not mentioned as serious criticism, but to indicate the complexities encountered describing material properties under all environmental conditions.

With the advent of dislocation theory by G. I. Taylor et al. in the 20's and early 30's, investigations in material behavior have proceeded from two points of view. The yielding phenomenon and the plastic behavior of metals can be viewed as either macroscopic or microscopic. The dislocation theory uses dislocation mechanics to explain the microscopic behavior of individual crystals. On a sufficiently large scale with proper averaging to account for the polycrystalline nature of metals, the microscopic and macroscopic points of view in the limit should be the same. Unfortunately, at present the respective points of view have not developed to this level. Common metals and alloys are susceptible to work hardening as judged by the tabulated results of yield strength versus amount cold work in the Metals Handbook.⁽¹⁵⁾ The current state of the art in material science is such that the material model must be judiciously selected when specific plasticity problems are investigated.

The history of plasticity problems starts in 1920 and 1921 when Prandtl⁽¹⁶⁾ showed that the two dimensional plastic problem for a perfectly plastic solid is hyperbolic. The general theory underlying Prandtl's special solutions was supplied by Hencky⁽¹⁷⁾ in 1923. During this time, Nadai investigated the plastic zones in a twisted prismatic bar of arbitrary contour both experimentally and theoretically. This work by Nadai is best summarized in his book.⁽¹¹⁾ In 1925, von Karman⁽¹⁸⁾ analyzed the state of stress in rolling using approximate techniques. Siebel and then Sachs soon followed with a similar analysis for wire drawing.^(19,20) The analysis of plasticity renewed interest in the concept of strain.

P. Ludwik⁽²¹⁾ used Hencky's concepts of natural or logarithmic⁽²²⁾ strain to compare tensile test and compressive test curves on the basis of natural strains. He found that the stress strain relationships are

nearly coincident. This was the first modification of the concept of strain to come into general use. Prior to this time the accepted theory of strain was Cauchy's infinitesimal strain theory. Cauchy's equations together with Cauchy's other analytical work in the 1820's form the elastic theory now admitted for isotropic solid bodies with small deformations. (Reference 23) Love⁽²³⁾ references the history of the development of strain theory for general displacement while summarizing the results in his book. Green and Zerna⁽²⁴⁾ also summarize the theory of strain for general displacements emphasizing the general curvilinear tensoral properties of the theory.

There is an important analytical distinction between plasticity problems that can be characterized as involving small deformations, such as the yielding of bars, and problems characterized by large plastic deformations, such as extrusions. The plasticity problems characterized by small deformations have plastic and elastic strains of approximately the same order of magnitude. Reuss⁽²⁵⁾ produced a general plasticity theory, to allow for both components of strain. Plasticity problems characterized by large deformations usually consider the elastic strain negligible; this invokes the assumption that the material is incompressible. Prandtl used this last assumption together with the isotropic, rigid, plastic, and non-hardening material to describe large deformation plasticity problems as hyperbolic. The characteristics of the solution of these hyperbolic plasticity equations are called slip lines. Geiringer⁽²⁶⁾ developed the equations governing the variation of velocity along these slip lines.

Since the slip line theory of Prandtl, Hencky, and Geiringer, several other ways have been suggested for the analysis of plastic processes with large deformations. These methods are sometimes classified as follows:⁽²⁷⁾

- a. The Siebel energy method.⁽¹⁹⁾
- b. The Sachs slab method.⁽²⁰⁾
- c. The Johnson-Kudo-Kobayaski upper-bound method. ^(28,29,30)
- d. The Thomsen visioelasticity method.⁽³¹⁾

When compared to experiment, slip line and the first three methods predict power requirements and forming forces that were within engineering accuracy, provided appropriate values for the effective stresses have been chosen.⁽²⁷⁾ These methods have been modified to approximate the variation in the effective yield stress (the Sachs method), or predict a stress distribution (the slip line method). Those parameters characterizing the process can be modeled quite accurately. On the other hand, the accurate prediction of the distribution of deformations cannot be made for many plastically deformed products.

The Thomsen visioelasticity method is a thorough experimental examination of a plastic process which is capable of correlating the process variables to the yield strength distribution after the fact. However, it is not predictive. This method consists of measuring the deformation and calculating the strain field by using a split billet; with the assumption of steady state operation, the strain rate field is determined and with the aid of a material model, the stress field can be determined from the strain and/or the strain rate field. This can then be compared with experimentally measured loads.

In the plastic analysis of large deformations, the material model provides the means of relating the mechanics of deformation to loading. Bridgman,⁽³²⁾ in his survey of material models, discusses the constraints a model must exhibit if it is to display realistic behavior. At present, a general model does not exist. Therefore, the material model selected

must be in agreement with observed behavior of the test material in the range of process variables that are encountered in the specific plastic process studied. The elevated temperatures and high strain rates of many commercial processes are those very conditions where a rigid-plastic material model can be effectively used. On the other hand, at lower temperatures and slower strain rates the work hardening behavior of materials can predominate.

The work hardening behavior of metals is complex, yet reasonable approximations have been developed. Hodierne,⁽³³⁾ for example, using the well known power law, found that

$$\sigma = K(\epsilon)^n ,$$

is a good approximation for the plastic portion of the stress strain behavior of 15 different metals. Barclay⁽³⁴⁾ in 1965 used the same relationship in the experimental examination of hardening mechanisms in AISI type 301 stainless steel. Datsko⁽³⁵⁾ uses this power law in the elementary analysis of forming operations. Caddell and Atkins,^(36,37) in a study of redundant work factors for rod drawing, found that the redundant work factor can be related to the strain hardening characteristics of the metal being drawn. Caddell, Needham, and Johnson⁽³⁸⁾ cold rolled rings of aluminum and compared experimentally determined yield strengths in three mutually perpendicular directions to the response of the annealed metal if it were given equivalent uniaxial reductions. Avitzur⁽³⁹⁾ includes effective strain hardening in an upper bound solution of plastic flow through conical converging dies.

The cold extrusion of metals requires the analysis of the deformation histories, if an accurate material model is to be included; such models

are required to relate deformations to product properties. Because of engineering interest in product properties, the Lagrangian point of view for kinematic analysis of the cold extrusion of aluminum is used. This analysis of the extrusion process is explicitly related to deformation histories.

SCOPE OF INVESTIGATION

The extrusion process used in this investigation is the direct cold plane strain extrusion through tapered dies; The work hardenable material used in this investigation is 6061-0 aluminum. (See Appendix A.) Die angles and reductions in area used in this study exclude those that would form dead metal regions within the die cavity. In this dissertation the phrases "plane-strain extrusion" and "two-dimensional extrusion" will be used interchangeably.

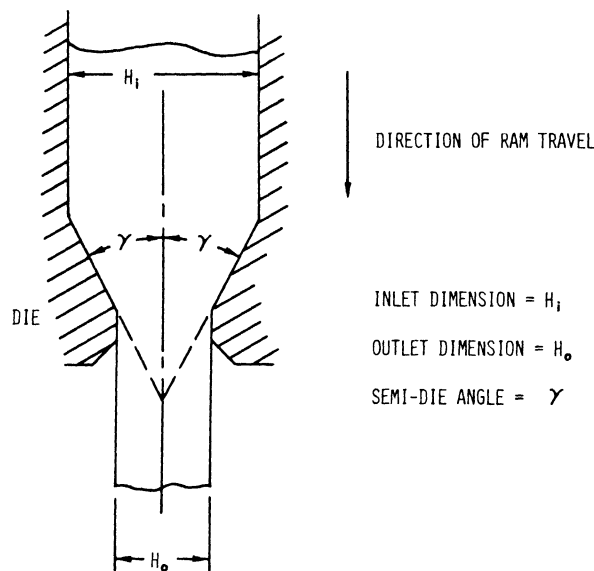


Figure 1 Two dimensional extrusion through tapered dies.

The reduction in area,

$$R = (H_i - H_o)/H_i, \quad (1)$$

and the semi-die angle, γ , are investigated for values shown in Table I.

The outlet to inlet dimension ratio,

$$H = H_o/H_i \quad (2)$$

is related to the reduction in area,

$$H = 1 - R. \quad (3)$$

TABLE I
GEOMETRIES INVESTIGATED

Semi-die Angle γ	Reduction in Area (R)	Dimension Ratio (H)
22.5°	0.276	0.724
22.5°	0.451	0.549
45.0°	0.449	0.551

Within the limitations of these constraints, the kinematic modeling of the direct two dimensional extrusion process takes the following steps:

1. A split billet is steadily extruded for the geometries listed in Table I.

2. A reference frame or coordinate system is created for the geometries listed in Table I.
3. A reference continuum is chosen and the path lines and deformation field are determined for the steady flow through the geometries listed in Table I. The reference continuum chosen is the perfect fluid. The deformation field of a perfect fluid is the result of an irrotational flow field.
4. The real metal deformation field is compared to the perfect fluid deformation field. The term real metal is used to indicate a direct relation to the experimentally determined kinematic information.
5. The selected measure of real metal rotationality is the differences between real metal path lines and perfect fluid path lines.
6. The measure of rotationality for the real metal flow is modeled.
7. Using stream function theory and the modeled measure of rotationality, the modeled velocity field is determined.
8. The modeled real metal deformation fields are determined from the modeled path lines and velocity field.
9. The modeled real metal deformation field is compared to the real metal deformation field.
10. The slip line theory deformation field is compared to the real metal deformation field.

These steps are taken to meet the objective of providing a kinematic modeling method for the flow of a work hardenable material during the extrusion process.

EXPERIMENTAL PROCEDURE, TEST EQUIPMENT, AND EXPERIMENTAL RESULTS.

INTRODUCTION

It seems that small changes in system geometry can result in large changes in the entire flow pattern during plastic deformation processes. These small changes in system geometry can make the difference between:

- (1) Die break through during stamping or no die break through.
- (2) Columnar plastic instability during cold heading or no columnar instability.
- (3) Dead metal region formation during extrusion or no dead metal region formation.

It is nearly impossible to predict flow patterns for all conditions from theoretical considerations alone; other approaches are needed.

One of the most effective methods of approach is flow visualization. Such direct observation of the internal flow in metals is in conflict with metallic opaqueness, but the split billet technique partially overcomes this difficulty for the steady two dimensional extrusion of metals. In this technique, the billet is split normal to the third dimension and a lattice is marked on these internal surfaces. The split billet is then extruded as a single billet.

Two dimensional extrusion assumes no deformation gradient in the third dimension. During the extrusion process the billet is contained in a die cavity, so there is inevitable contact between the billet and the outer die wall. As the extrusion process proceeds, the frictional effects between the outer die wall and the billet can introduce deformation gradients in the third dimension. Proper experimental techniques and lubrication can minimize these frictional effects, but if any plane in the

third dimension is to be considered representative of the flow, a negligible deformation gradient in the third dimension must be demonstrated experimentally. To do this, different splitting planes relative to the third dimension in the billet to be extruded are selected. The deformations of the lattices marked on these different planes are compared and the magnitude of the deformation gradient in the third dimension is assayed.

Flow visualization is an important tool for establishing flow models as a basis for mathematical models. But in order to interpret pictures of the flow field, it is necessary to understand four concepts that relate the pictures to the kinematic description of the flow field. These four concepts, from continuum mechanics, are:

- (1) Path lines; the path a particle takes through space.
- (2) Streak lines; the locus, at a given instant, of all particles which have passed through or will pass through a fixed point in space (coincident with (1) for steady state (s.s.)).
- (3) Stream lines; the curves in space always tangent to the velocity vectors of the flow field (coincident with (1) for s.s.).
- (4) Time lines; the level curves of a time function defined for the flow by identifying particles passing a particular line in space. These lines and curves are surfaces in general three dimensional flows.

In general, the time function is a path dependent function and the time lines are most useful when the particles are identified at a particular line normal to the flow directions. For steady flows, the path lines, streak lines and stream lines are coincident, that is, the paths do not change with time. All particles passing a particular point continue on

the same path and, consequently, if the particles stay on the same path the velocity must always be tangent to that path.

TEST EQUIPMENT

The equipment used to implement the experimental investigation can be related to three areas: (1) that used to perform the extrusion process, (2) that used to prepare the extrusion billets, (3) that used to mark the lattices on the internal surfaces of the split plane in the billets. The specific extrusion process used requires a press and an extrusion machine. The specifications for the press are tabulated in Table II.

TABLE II
PRESS SPECIFICATIONS

Company:	Forney's Incorporated, New Castle, Pennsylvania
Model Number:	QC-500
Serial Number:	62175
Operation:	Hydraulic
Daylight Distance:	The maximum distance between the lower platen and upper frame cross member is 22-1/2 inches.
Load Range:	0 to 500,000 pounds
Load Indicator:	Bourbon Tube type, 1,000 pound increments from 0 to 500,000 pounds.
Piston Velocity Range:	0 to 0.5 inches per minute.
Maximum Piston Stroke:	3 inches

The extrusion machine, Figure 2, was developed specifically for the split billet technique of flow visualization as applied to the direct two dimensional cold extrusion of aluminum. The final design of the machine can be characterized as having met the following constraints:

- (1) It fits within the 22-1/2 inches maximum daylight clearance in the press.
- (2) Allowance is made for ram travel, space for the billet before extrusion, and space for the extruded product without requiring modification of press cross members.
- (3) It is easily modified with respect to reduction in area and semi-die angle.
- (4) Ram travel is controlled accurately.
- (5) The machine is easily disassembled for removal of the partially extruded billet without damage.
- (6) It withstands the loads during the extrusion of 6061-0 aluminum.

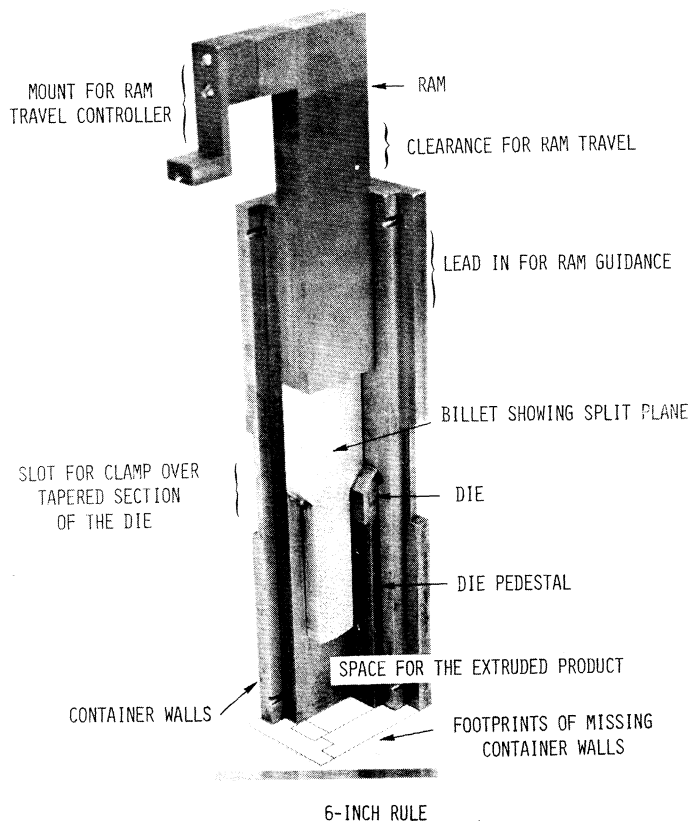


Figure 2 Exposed internal view of the extrusion machine

The relationships between the extrusion machine elements for changing extrusion geometry are shown in Figure 3, where it can be seen that two new die pieces are required to change extrusion geometry. While the scope of this investigation is limited to tapered die geometries, the possible die geometries to be studied are limited only by fabrication techniques.

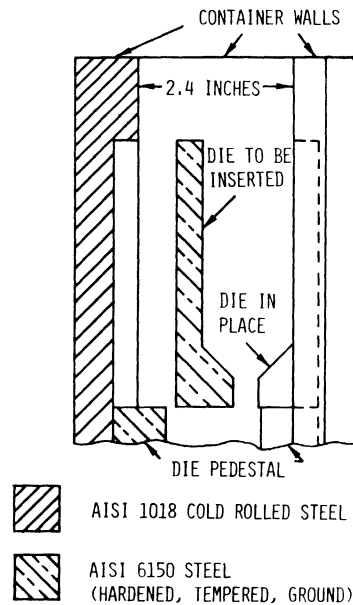


Figure 3 Die pieces for altering extrusion geometry

The control of ram travel (as shown in Figure 4) is required because the piston travel is limited to three inches. As indicated in Figure 2, the billets are fabricated so as to originally fill the tapered portion of the die cavity before extrusion. In the first stage of extrusion, the ram travel is limited to clearing the tapered section of the die of original material and establishing a steady flow. The length of ram travel required to establish steady flow is determined by a previous visual

observation of the path lines on the split plane of an extruded billet downstream from the tapered section. After the first stage the press is stopped. After placing a spacer block between the ram and press cross-head, the second stage of the extrusion is now accomplished. This produces a steadily extruded billet within the piston travel limitation of three inches.

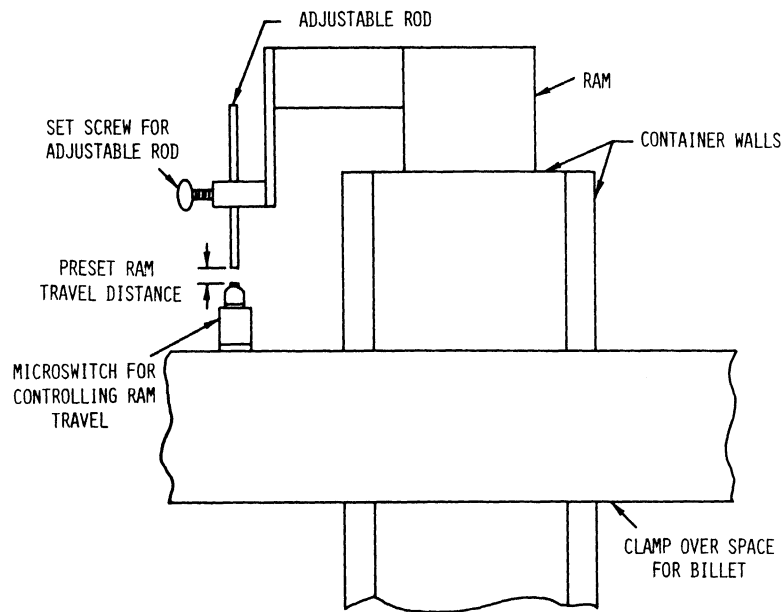


Figure 4 Essential elements of ram travel control

Clamping on the extrusion machine is shown in Figure 5. The clamp over the lead-in region for ram guidance is held together with tapered pins. This provides added rigidity to the container walls in the lead-in region, but low clamping pressure so as to minimize binding the ram. Tapered pins are threaded to accommodate a pin removal nut. The clamps over the space for the billet and over the tapered die section are held together with two, two-inch diameter threaded studs. Through the use of

the threaded tapered pins and threaded studs, the extrusion machine can be disassembled without damaging the partially extruded billet. Large clamping forces on the container walls are produced by the clamps over the space for the billet and over the tapered die section. These forces are the result of evenly tightening the nuts on the threaded studs to withstand over two thousand foot pounds of tightening torque. The clamping forces must be larger than the extrusion forces, which tend to separate the container walls, if finning of the billet into the spaces between the container walls is to be prevented. During the development of the extrusion machine, the magnitude of the required clamping forces was initially underestimated. However, with the present setup, the extrusion machine can withstand the loadings during the extrusion of 6061-0 aluminum. (See Appendix B.)

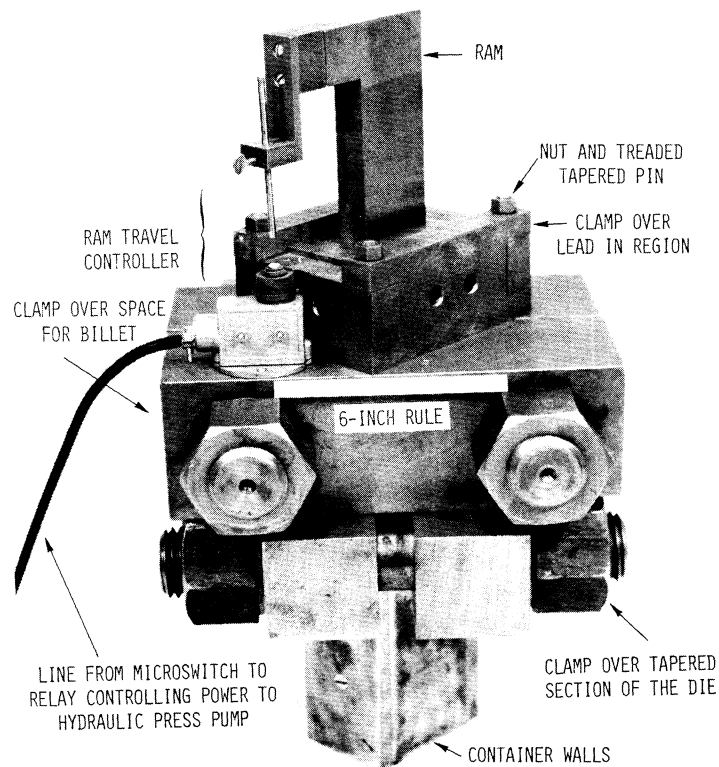


Figure 5 Clamps on assembled extrusion machine

EXTRUSION BILLET

The billets are annealed, machined on a vertical milling machine, then the surfaces of the billet are finished by hand with a single cut mill smooth file. Finally, the process used to mark the lattice on the billets is electrochemical marking and is accomplished with commercially available equipment. The specifications of the marking equipment are tabulated in Table III.

TABLE III

MARKING EQUIPMENT SPECIFICATIONS

Company:	The Lectroetch Company, East Cleveland, Ohio
Power Unit:	Model V45A with heavy duty cord set (nominally 0-25 volts AC/DC, 0-45 amperes)
Power Unit Serial Number:	274
Rocker Pad Assembly:	Model 3-1/2" x 7" RP3
Stencil:	Model 3L25055, 5" x 9" Heavy Duty.
Stencil Cleaner:	Type 3L
Electolyte:	Type #210A
Cleaner:	Type #3

The space for the billet in the extrusion machine is nominally 1 inch by 2.4 inches wide by 6 inches long, and the billet shown in Figure 6 is half as thick as the billet cavity. Two halves, as shown in Figure 6, are required to make up the split billet for the flow visualization study.

The bar stock is originally in a T-6511 temper condition. The 6061 Aluminum is heated at 775°F for 3 hours and then cooled at a maximum of 50°F/Hr until 500°F to give it an "0" temper designation as specified in the Metals Handbook.⁽¹⁵⁾ The "0" temper designates a full anneal.

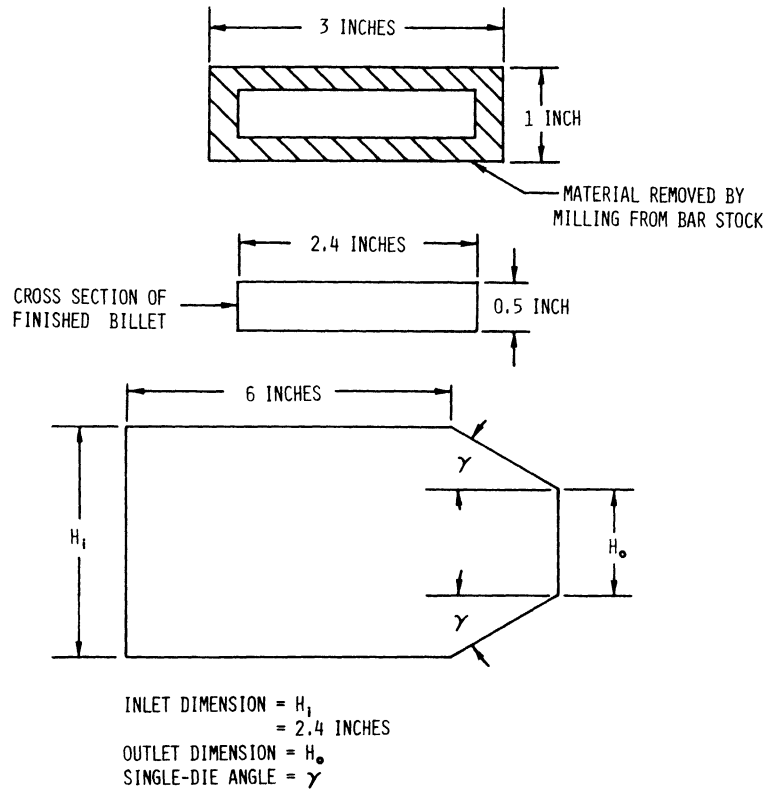


Figure 6 Extrusion Billet. Material: 6061-0 aluminum

Material is removed from the billet as shown in Figure 6 on a vertical mill with successively smaller cuts, the final cut always being less than 0.003 inches. This machining procedure is adopted to minimize the material affected by deformation during machining.

The objects of the finishing procedure are:

- (1) to further remove material deformed by machining and the milling marks
- (2) to prepare a surface that can be electrochemically marked by the marking equipment
- (3) to prepare a surface that can be photographed well to record the visual flow pattern.

The billets are hand finished with a file; this is followed by light buffing with crocus cloth. The draw filing procedure meets all three objectives, however two hours of filing time are required for each billet prepared for extrusion.

LUBRICATION

The effect of lubrication is twofold; both extruded product and the loads during the extrusion process are influenced. Three different types of lubricants, as specified in Table IV, are used and Figure 7 shows the areas of application for the lubricants.

Inadequate lubrication can result in a poor surface finish on the extruded product and is indicative of frictional effects that can cause deformation gradients in the third dimension. The sacrificial lead foil together with coatings of lubricant types A and B effectively reduces the frictional effects in the third dimension.

The diminished frictional effects reduce the ram load and the extrusion forces on extrusion machine container walls, the latter leading to

easier restraint by the clamping forces. More effective clamping forces tend to reduce finning and increase overall quality of the extruded product.

TABLE IV
LUBRICANT SPECIFICATIONS

Lubricant A:	A grease gear lubricant (Mobil Oil, Mobilplex)
Lubricant B:	Mixture by volume:
	i) 5 parts, Gear Lube (Mobilplex)
	ii) 2 parts, Vinyl Stearate Powder
	iii) 1 part, Flake Graphite
Lead Foil:	Commercially pure lead billet rolled to 0.008 inch foil

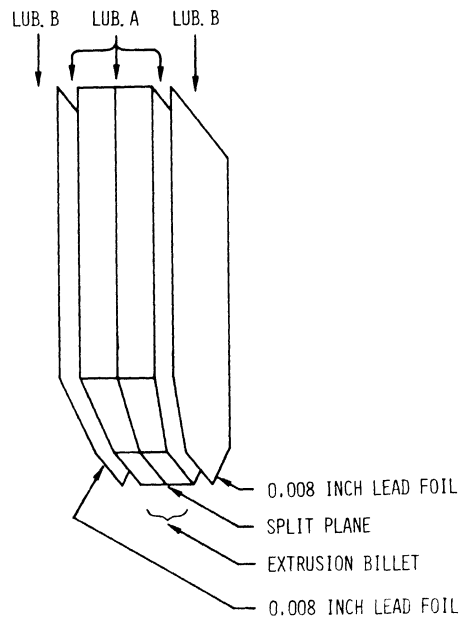


Figure 7 Lubrication for extrusion billet. The billet surfaces adjacent to the die walls were coated with lubricant A.

GRID SYSTEM

The regular lattice marked on the billet prior to extrusion will now be called the grid;⁽⁴⁰⁾ it is especially chosen to relate to the important kinematic variables of the steady two dimensional extrusion process.

Figure 8 shows the photographic record of the change in the grid during the extrusion process and this record is called the real metal deformation field.

The grid chosen is a lattice of numbered concentric circles, 0.1 inch and 0.2 inch diameters respectively, enclosed within 0.2 inch squares. The sides of these squares, being coincident with the velocity direction upstream from the tapered die section, are then stream lines. For steady flow, the path lines, streak line and stream lines are coincident. Since the flow of aluminum through the extrusion machine is steady, the paths do not change with time, and all particles passing a particular point continue on the same path. A steady flow is assured when the sides of the deformed squares again are coincident with the direction of the steady velocity downstream from the tapered die section as shown in Figure 8. For this steady flow the sides of the squares are the path lines, streak lines, and the streamlines.

Upstream from the tapered die section the lines normal to the streamlines are moving with the steady velocity of the ram. The distance between the normal lines is a constant 0.2 inches in this uniform velocity region. The inlet velocity is V_i . If the material is incompressible, the time interval for these normal lines to pass a point fixed in space is also constant,

$$\Delta t = 0.2 \text{ inches}/V_i \quad . \quad (4)$$

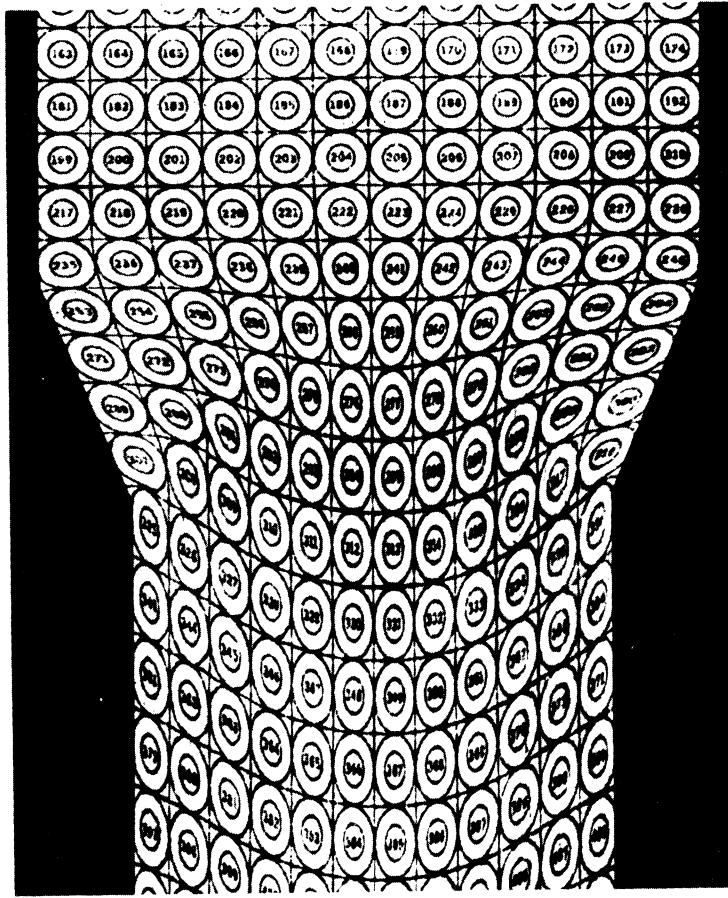


Figure 8 Real metal deformation field. Material: 6061-0 aluminum

For the large deformations being studied here, the aluminum is considered incompressible. If the line between rows of circles numbered 163, 164, . . . , 174 and circles numbered 181, 182, . . . , 192 in Figure 8 is considered coincident with a fixed line in space at which the particles are identified every Δt (Equation 4), the sides of the squares normal to the flow directions at the line, are identified at equal time intervals. This defines a time function, for the steady flow field, in

the x plane, (See Figure 9.),

$$t = t(x_1, x_2). \quad (5)$$

The level curves of this function are the sides of the squares and are defined by

$$t(x_1, x_2) = \pm N\Delta t \quad (6)$$

where $N = 0, 1, \dots, K$ and where Δt is defined by Equation (4). Down stream where the flow is faster, the distance between time lines is greater so that the time interval between time lines passing a fixed point remains constant. Therefore, the sides of the squares originally normal to the flow direction upstream from the tapered die section are time lines for the entire flow field.

Stream lines proceeding through the periphery of an infinitesimal area at some time t , will form a tube; this is called a stream tube. Figure 8 shows 6 stream tubes on each side of the center line and the changing of the circles to ellipses describes the deformations. Within a stream tube the next ellipse downstream shows the change in deformation of the ellipse during an increment of time, Δt . The procession of circles changing to ellipses down each stream tube describes the deformation history within the stream tube and this history is for discrete increments of time. The twelve stream tubes complete the incremental representation of the entire deformation field from the Lagrangian point of view.

EXPERIMENTAL RESULTS

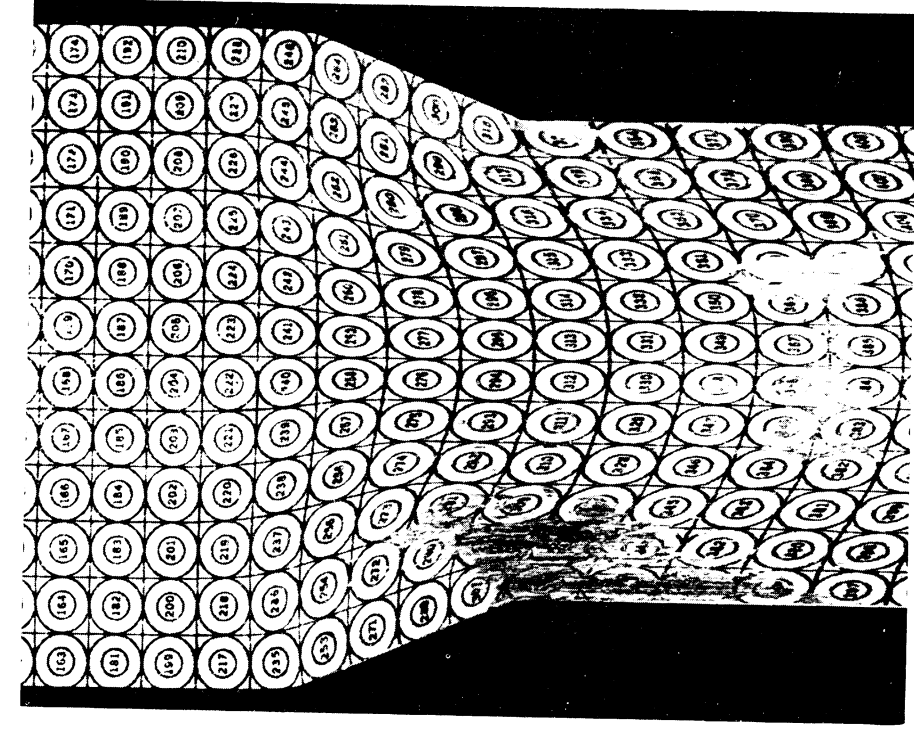
The experimental results are summarized in Figures 9, 10, and 11. In these figures are the photographic records of the steady flow pattern

for 6061-0 aluminum during the direct cold plane strain extrusion through tapered dies. These flow patterns which are called "real metal deformation fields" are for the geometries listed both in Table I and on the figures. The photographic records are for both the split plane and the plane adjacent to the die wall as indicated on the figures.

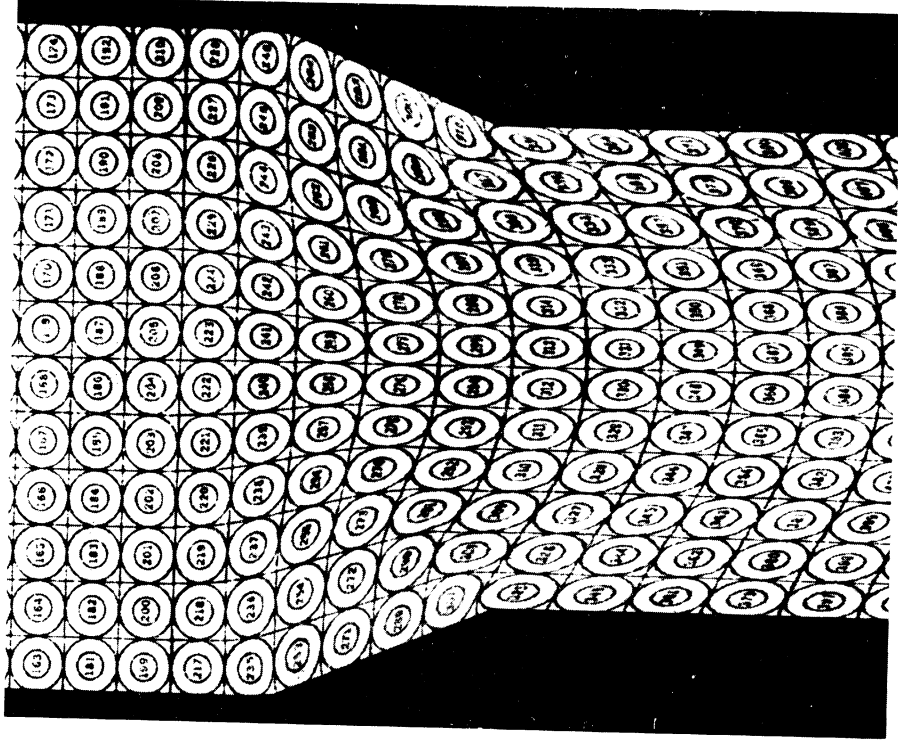
During the extrusion process, the aluminum displaces some of the lead in the foil (See Figure 7) and the clamps deflect due to the extrusion pressure. The combined effects of displacing lead and deflecting clamps results in an increase in thickness of the extruded billets. This is a change in dimension normal to the x_1, x_2 plane shown in Figures 9, 10, and 11. Due to the very nearly conserved volume during these plastic deformations the squares in the grid are foreshortened in the direction of flow. In Table V, the effective foreshortening ratio,

$$L = \frac{\text{Shorter length due to increased thickness}}{\text{Length without increased thickness}} \quad (7)$$

for geometries shown in Figures 9, 10, and 11 are listed. This results in the interpretation that a somewhat thicker foreshortened billet underwent extrusion.



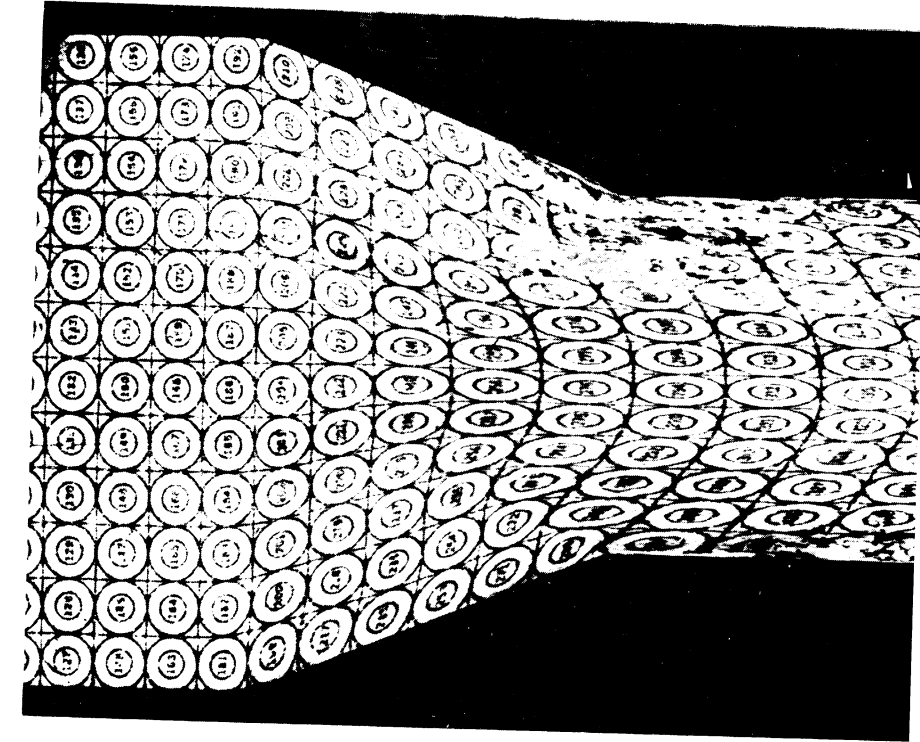
Plane adjacent to die wall
Reduction in area: $R = 0.276$
Material: 6061-0 aluminum



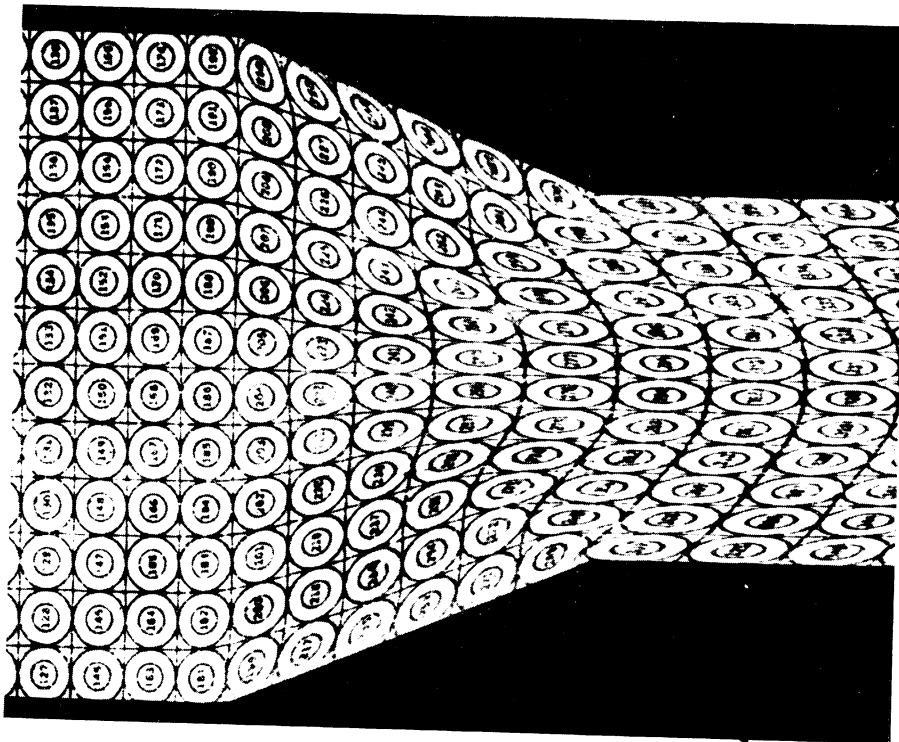
Split plane
Semi-die angle: $\gamma = 22.5^\circ$
Outlet to inlet
dimension ratio: $H = 0.724$
Material: 6061-0 aluminum



Figure 9 Real metal deformation field



Plane adjacent to die wall
Reduction in area: $R = 0.451$
Material: 6061-0 aluminum



Split plane
Semi-die angle: $\gamma = 22.5^\circ$
Outlet to inlet
dimension ratio: $H = 0.549$

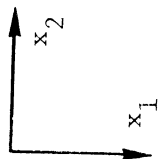
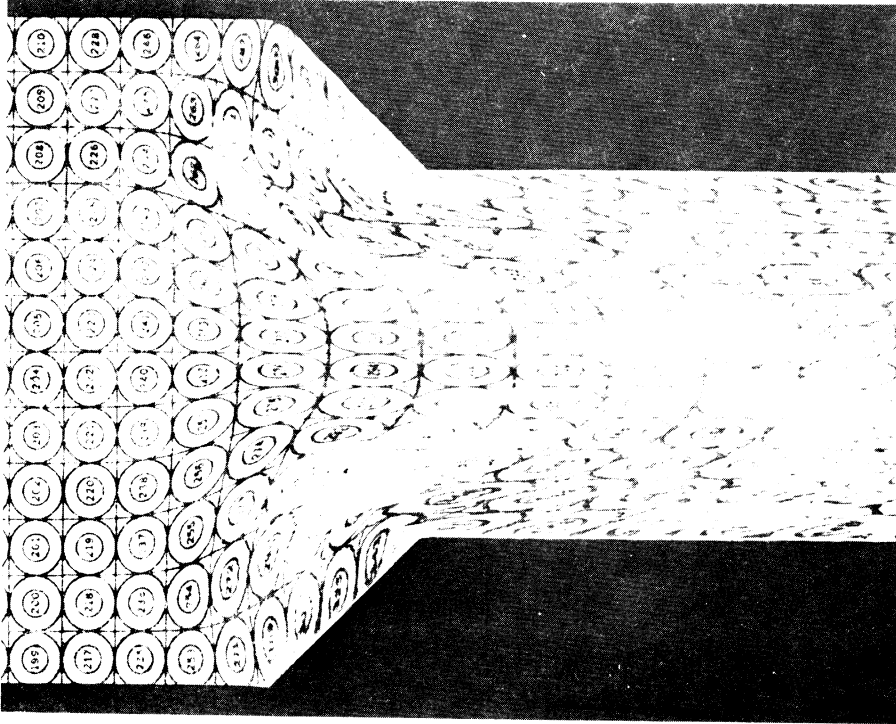
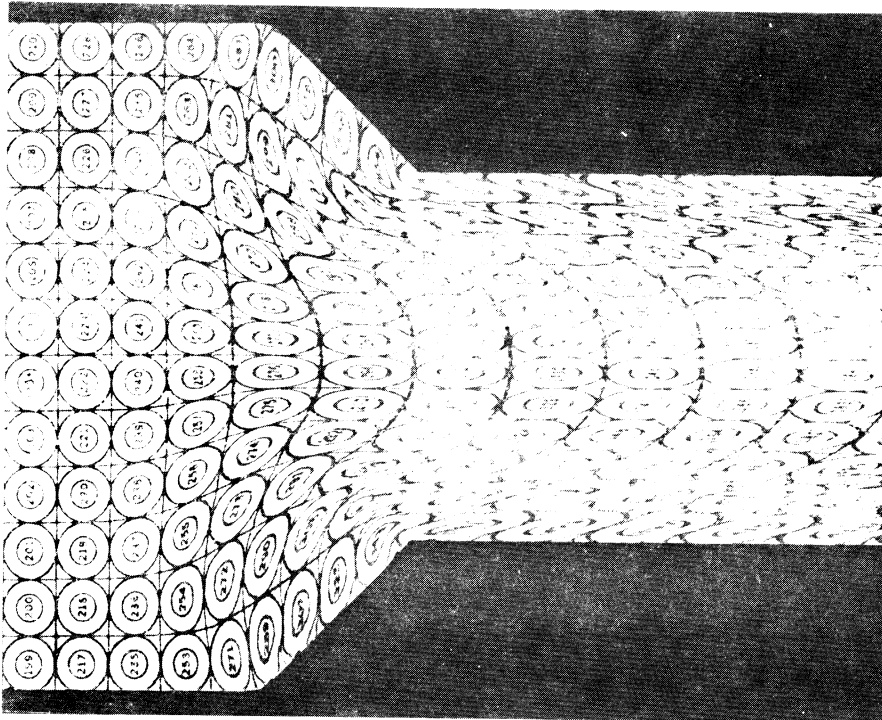


Figure 10 Real metal deformation field



Plane adjacent to die wall
Reduction in area: $R = 0.449$
Material: 6061-0 aluminum



Split plane
Semi-die angle: $\gamma = 45^\circ$
Outlet to inlet
dimension ratio: $H = 0.551$

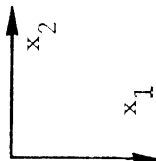


Figure 11 Real metal deformation field

TABLE V
FORESHORTENING RATIOS

Figure	Geometry	Foreshortening Ratio
9	$\gamma = 22.5^\circ$	
	H = 0.724	L = 0.975
	R = 0.276	
10	$\gamma = 22.5^\circ$	
	H = 0.594	L = 0.942
	R = 0.451	
11	$\gamma = 45^\circ$	
	H = 0.551	L = 0.960
	R = 0.449	

EXPERIMENTAL CAPABILITIES

The aim of the experimental portion of this investigation is to provide a capability for the direct visualization of kinematic variables which are the objects modeled. The steady extrusion results in the path,

1. Path lines
2. Streak lines
3. Stream lines
4. Time lines
5. Deformations.

These are the objects modeled. The steady extrusion results in the path,

streak and stream lines being coincident. The split billet technique, the selected grid and the specially developed extrusion machine are the experimental techniques used to implement the flow visualization.

If any plane in the third dimension is to be representative of the flow, different planes must be compared to determine the magnitude of any deformation gradients introduced by friction. Assuming a deformation gradient exists, the greatest difference in deformation exists between a split plane at the center of the billet where the frictional effects are the least and the plane adjacent to the die wall where the frictional effects are the greatest. A split plane at the center of the billet and the plane adjacent to the die wall are shown for the geometries listed in Table I in Figures 9, 10, and 11. In each case, the planes adjacent to the wall show evidence of local scraping where lubrication was inadequate. Both planes in each figure have the same scale.

The existence of deformation gradients is evidenced by changes in location and shape of the path lines, time lines, and deformation ellipses between the central split plane and the plane adjacent to the die wall. By comparing the differences in location and shape of the path lines, time lines, and deformation ellipses between the split plane and the plane adjacent to the die wall in Figures 9, 10, and 11, the deformation gradients are assayed to be negligible.

The central split plane is taken as most representative of this extrusion process. In conclusion it is felt that the experimental aim of providing a capability for the direct visualization of path lines, time lines and deformation ellipses is met. The real metal deformation fields that result from the application of the experimental capability described in this chapter are the objects of a Lagrangian kinematic

modeling method that mathematically describes the deformation of a work hardenable material as a function of time, relative to the path line.

Chapter III

ANALYTICAL PROCEDURE FOR MODELING REAL METAL DEFORMATION FIELDS IN DIRECT TWO DIMENSIONAL COLD EXTRUSION OF ALUMINUM

INTRODUCTION AND ASSUMPTIONS

Real metal deformation fields shown in Figures 9, 10, and 11 are to be modeled. The content of this chapter will show, by example for the deformation field in Figure 9, how to use this kinematic information as the basis for a mathematical model.

The presentation of the example follows these steps:

1. selection of a reference frame
2. selection of a reference continuum
3. determination of the path lines, time lines, and deformation ellipses for the reference continuum in terms of the reference frame for the geometry of Figure 9
4. determination of the kinematic variables in step 3 on the computer and implementation of computer aided plots of these variables in the format of the information shown in Figure 9
5. comparison of the plotted deformation field of the reference continuum with the real metal deformation field
6. modeling of the real metal path lines
7. modeling of the real metal velocity field
8. modeling of the real metal deformation field using the models from steps 6 and 7
9. implementation of the computer aided plots of the modeled real metal deformation field.

Four assumptions are made:

1. The metal can be modeled by a continuum.
2. The continuum representing the metal can be modeled as

incompressible for the large deformations encountered during this two dimensional extrusion process.

3. The metal is bounded and follows the die geometry.
4. The flow is symmetric with respect to the center line.

The first assumption neglects the microscopic crystalline nature of metals, while the second neglects changes in density. The third and fourth assumptions limit the investigation to symmetric extrusion processes where dead metal regions are not formed.

REFERENCE FRAME AND NORMALIZATION

The selected reference frame is the orthogonal curvilinear coordinate system shown in Figure 12. The selected reference frame and the reference continuum are directly related. The reference frame is the result of the Schwarz Christoffel transformation for the general quadrilateral with two vertices extended. One of the extended vertices contains a source and the other contains an equal sink and from the source to the sink flows a perfect fluid. The perfect fluid is the selected reference continuum. The complex analysis for this Schwarz Christoffel transformation is presented in Appendix C.

The generation of the Schwarz Christoffel transformation for the geometry of Figure 9 starts with the extrusion geometry being transformed to the upper Schwarz Christoffel half plane by conformal transformations through the rationalizing plane. The solution for a perfect fluid flowing in the transformed geometry is described by the conformal transformation from the complex potential plane to the Schwarz Christoffel half plane. Since conformal transformations of solutions remain solutions to flow problems in the transformed geometry, the conformal transformation

of the flow solution in the Schwarz Christoffel half plane to the physical plane is a solution to the flow problem in the physical plane. In the complex potential plane, streamlines and potential lines are defined. The images of a family of these lines in the physical plane results in the orthogonal curvilinear lattice shown in Figure 12.

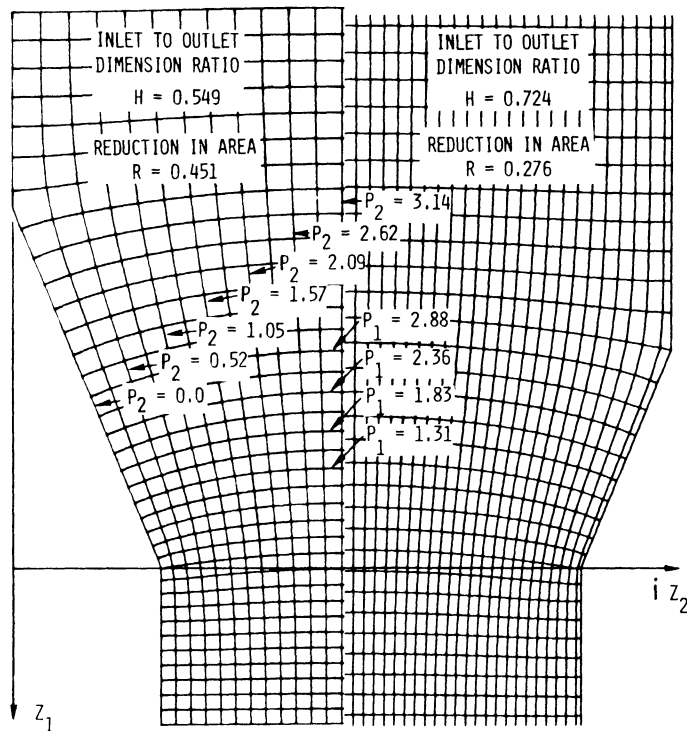


Figure 12 Orthogonal curvilinear coordinate systems showing two different spacings

The physical plane is shown in Figure 13. Due to the symmetry of the extrusion process selected, only half of the flow field is needed for completeness. The complex variable z is defined in terms of the normalized physical dimensions of the extrusion billet (Figure 6),

$$z = z_1 + iz_2 \quad (8)$$

where

$$z_1 = x_1/x_{\text{ref.}} \quad ; \quad z_2 = x_2/x_{\text{ref.}} \quad (9)$$

and

$$x_{\text{ref.}} = 1.2 \text{ inches}/\pi \quad (10)$$

With this definition the geometry becomes dimensionless. The inlet dimension becomes 2π and the distance to the center line becomes π , as shown in Figures 12 and 13. In the limit upstream and downstream from the tapered die section are the extended points A and D, while the tapered die section is defined by points B and C in Figure 13.

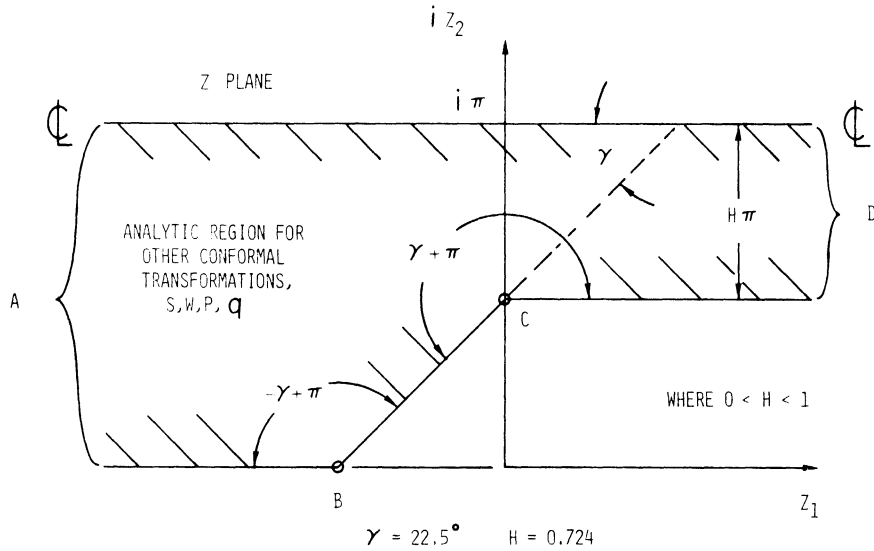


Figure 13 Physical plane

The derivative defining the Schwarz Christoffel transformation is in terms of w , the complex variable defining the Schwarz Christoffel upper half plane as shown in Figure 14. The derivative form of the transformation used for the extrusion geometry shown in Figure 9 is

$$\frac{dz}{dw} = \frac{H(w-1)^{1/8}}{w(w-H)} \quad (11)$$

The transformation defined by Equation (11) applies to all possible outlet to inlet dimension ratios H , when the semi-die angle is 22.5° or $\pi/8$ radians. The images of the points defining the die geometry in the physical plane are shown in Figure 14.

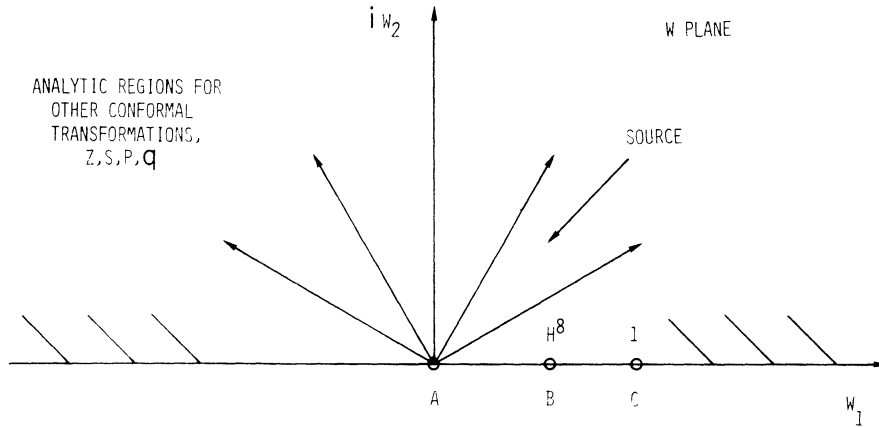


Figure 14 The Schwarz Christoffel upper half plane where point D is extended and contains sink

Equation (11) cannot be integrated directly, but by defining a new variable

$$s = \left(\frac{w-H}{w-1} \right)^{1/8}, \quad (12)$$

so that now

$$w = \left(\frac{H^8 - s^8}{1 - s^8} \right), \quad (13)$$

the Schwarz Christoffel transformation in terms of the rationalizing plane becomes,

$$\frac{dz}{ds} = 8Hs^6 \left(\frac{1}{1-s^8} - \frac{1}{H^8 - s^8} \right) \quad (14)$$

which can be integrated. The images of the points defining the die geometry in the rationalizing plane are shown in Figure 15. Equations (11), (12), (13), and (14) are conformal or define conformal transformations.

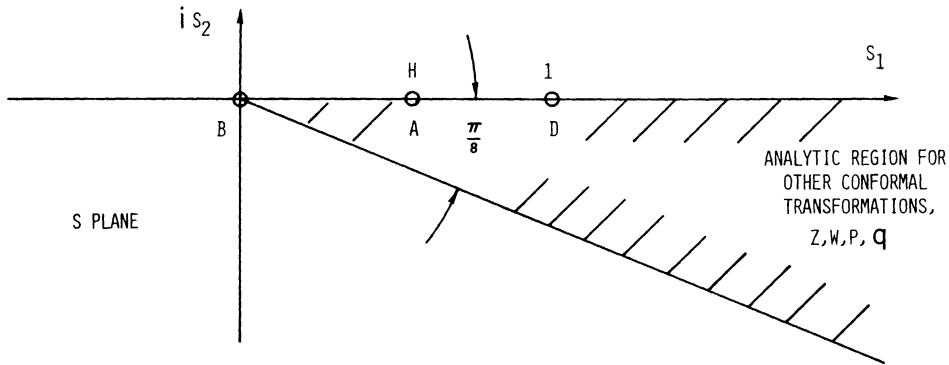


Figure 15 The rationalizing plane. Point C is extended.

The conformal transformation describing a perfect fluid flowing from a source to an extended sink as shown in Schwarz Christoffel upper half plane (Figure 14) is

$$p = V_A \text{Log } w , \quad (15)$$

or conversely

$$w = \exp (p/V_A) , \quad (16)$$

where the term V_A is the normalized uniform velocity in the limit upstream from the tapered die section,

$$V_A = \text{Actual Velocity/Reference Velocity} \quad (17)$$

where

$$\text{Reference Velocity} = 0.5 \text{ inches/minute} \quad (18)$$

The term $\text{Log } w$ (a complex function) is defined, $\text{Log } w = \log \sqrt{w_1^2 + w_2^2} + i\theta_w$

where $\theta_w = \tan^{-1}(w_2/w_1)$, θ_w is limited $0 < \theta_w < \pi$ for this problem, and \log is a logarithm to the base e (2.7183...). The complex potential plane is shown in Figure 16.

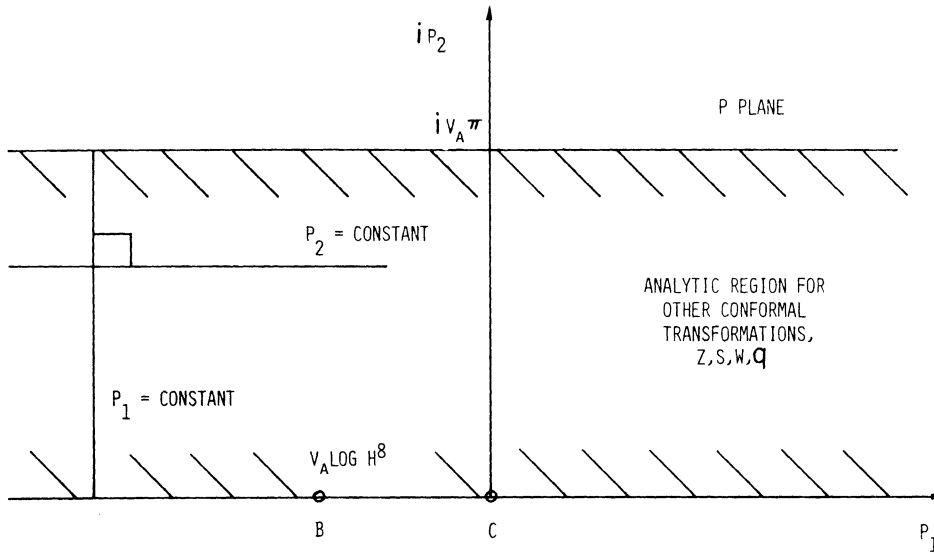


Figure 16 The complex potential plane where p_2 equal to a constant is a streamline and p_1 equal to a constant is a potential line. Points A and D are extended.

The complex potential plane,

$$p = p_1 + ip_2$$

can be interpreted as representing two important kinematic concepts for the flow of a perfect fluid. The image of p_1 equaling a constant in the z plane,

$$p_1(z_1, z_2) = \text{constant}, \quad (19)$$

is a potential line for the perfect fluid. The image of p_2 equaling a constant in the z plane,

$$p_2(z_1, z_2) = \text{constant}, \quad (20)$$

is a streamline for the perfect fluid. The potential function is defined as that scalar function whose gradient defines the velocity field. Since a conformal transformation conserves angular relations between lines, the conformal transformation of a family of streamlines that are orthogonal to the potential lines in the p plane remain orthogonal for the extrusion geometry in the physical plane, z .

Upon integration of Equation (14), the generation of the Schwarz Christoffel transformation is finished. The integrated form is

$$z = i^{1/2} \text{Log} \frac{(-i)^{1/2} H+s}{(-i)^{1/2} H-s} + (-i)^{1/2} \text{Log} \frac{i^{1/2} H+s}{i^{1/2} H-s} + i \text{Log} \frac{iH+s}{iH-s} - \text{Log} \frac{H+s}{H-s}$$

$$-H \left[i^{1/2} \text{Log} \frac{(-i)^{1/2} +s}{(-i)^{1/2} -s} + (-i)^{1/2} \text{Log} \frac{i^{1/2} +s}{i^{1/2} -s} + i \text{Log} \frac{i+s}{i-s} - \text{Log} \frac{1+s}{1-s} \right] \quad (21)$$

$$- \frac{(1-H)\pi}{\tan 22.5^\circ}, \text{ where for the two possible values of } i^{1/2} \text{ and } (-i)^{1/2}$$

the specific values required are

$$i^{1/2} = \sqrt{2}/2 + i\sqrt{2}/2$$

and

$$(-i)^{1/2} = -\sqrt{2}/2 + i\sqrt{2}/2.$$

Both values of $i^{1/2}$ and $(-i)^{1/2}$ are in the upper half plane.

The Equations (12), (16), and (21) are combined to provide an explicit closed form of the analytical expression for the conformal transformation from the complex potential plane to the physical plane. Each point

in the analytic region of the complex potential plane has a unique point in the analytic region of the physical plane. Therefore, the conformal transformation from the complex potential plane to the physical plane is a coordinate transformation and the family of streamlines and potential lines from the potential plane forms the basis of an orthogonal curvilinear coordinate system in the physical plane.

Three properties of this orthogonal curvilinear coordinate system are explicitly used in this investigation. The first property used is that boundaries and boundary conditions can be more economically described in this somewhat more natural curvilinear coordinate system. For example, the die shape is described by the expression,

$$p_1 = 0.$$

The second property used concerns differentiation. Christoffel symbols of the first and second kind are used when differentiating in general curvilinear coordinate systems. The concepts and distinctions embodied in Christoffel symbols for general curvilinear coordinate systems are not required for differentiations in the two dimensional orthogonal coordinate system shown in Figure 12. The third property used is the direct relationship between the coordinate system and the kinematics of the reference continuum.

REFERENCE CONTINUUM

The reference continuum selected is the perfect fluid; it is considered inviscid, incompressible and has only density, i.e., inertia. The perfect fluid is an analytical concept and is conceived to flow steadily in a symmetrically bounded channel as shown in Figure 12. This channel is of similar geometry to the die configuration for the steady direct two

dimensional cold extrusion of 6061-0 aluminum shown in Figure 9. The extrusion of the aluminum is referenced to this flowing perfect fluid; in essence, the flowing perfect fluid is the standard to which the actual flow is compared. Any differences between the actual flow and the standard are the result of differences between:

1. the environmental or external influences
2. the process variables
3. the flowing materials.

Since the flow of the perfect fluid is steady, the path lines, stream lines and streak lines are coincident. The stream lines for the steady flow of a perfect fluid in the geometry of Figure 12 are described by letting

$$p_1 = \text{constant},$$

in Equations (12), (16), and (21). These equations also describe the path lines. The time lines are determined from the path lines when the velocity with respect to the path line is known. For the perfect fluid, the velocity is defined by the conformal transformation

$$q = \text{conjugate } \frac{dp}{dz} \quad . \quad (22)$$

For the geometry of Figure 12 the expression for the velocity is,

$$q = (V_A/H) \text{ conjugate } (s). \quad (23)$$

The velocity plane is shown in Figure 17 together with the images of the points defining the die geometry. Equations (12), (16), and (23) directly relate the position on a path line to the velocity. The images of an array of perfect fluid path lines in the perfect fluid velocity plane is shown in Figure 18. The velocity at a particular position along a path

line is determined by the coordinate values of that path line point in the velocity plane. An example for a particular path line point is shown in Figure 18.

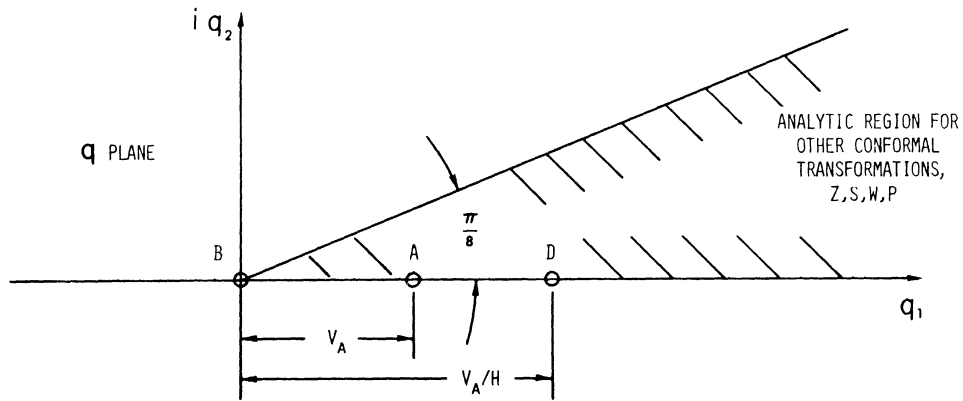


Figure 17 The velocity plane. Point C is extended.

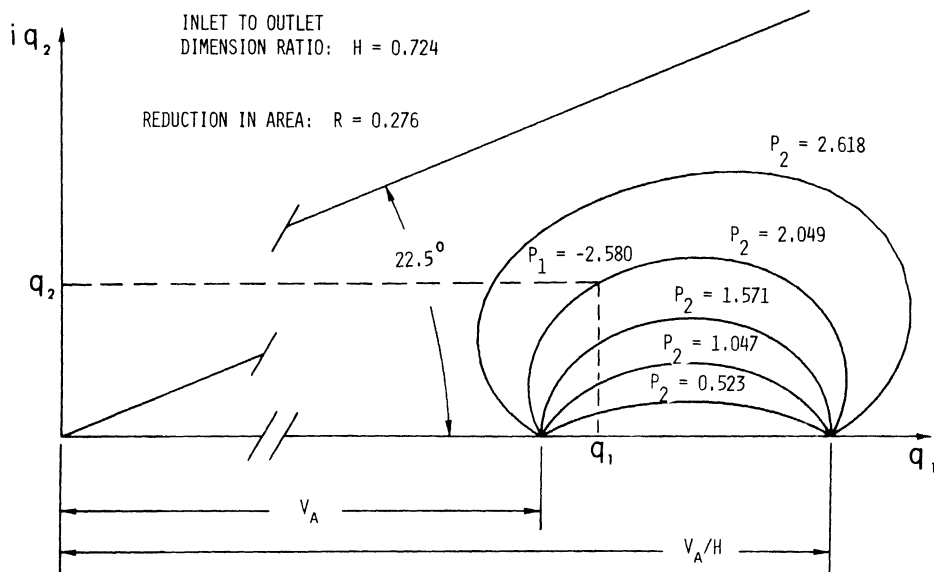


Figure 18 Images of an array of perfect fluid path lines in the perfect fluid velocity plane

PATH LINES, TIME LINES, AND STRAIN ELLIPSES

The path lines and time lines are related. For the discussion of these relationships, the path and the velocities on the path lines are assumed to be known. Experimentally the time lines can be identified when the grid system is selected as discussed in Chapter II. The mathematical expression for the time lines (two dimensional case) follows.

Let there be a velocity field. The curve

$$x = x(x_1, x_2) = \text{constant} \quad (24)$$

identifies all particles flowing through or on that curve. The particle's identity is assured if the position vector of that particle

$$\vec{R} = \vec{R}(t) \quad (25)$$

is a solution to Equation (24) when time t , is zero. That is, if

$$\vec{R} = \vec{D}(t) + \vec{R}_0 \quad (26)$$

where $\vec{D}(t)$ is the displacement vector, then $\vec{D}(t) = 0$ when $t = 0$ (27)

and \vec{R}_0 is a solution to Equation (24).

The differential equation,

$$dt = \frac{\dot{\vec{R}} \cdot \vec{dR}}{|\dot{\vec{R}}|^2} = \frac{dS}{v} \quad (28)$$

where

$$\begin{aligned} \dot{\vec{R}} &= d\vec{R}/dt, \\ dS &= \dot{\vec{R}} \cdot \vec{dR} / |\dot{\vec{R}}|, \end{aligned}$$

and

$$v = |\dot{\vec{R}}|,$$

together with the boundary conditions

$$S|_{t=0} = 0 \quad (29)$$

$$\vec{R}|_{t=0} = \vec{R}_0 \quad (30)$$

defines the time function for this process. The specific \vec{R}_0 associated with a particle, identifies that particle's path. Time is a path function as defined for this process and upon integration, time becomes,

$$t = \int_0^t dt = \int_0^S dS/V \quad . \quad (31)$$

Let the expression $t = t(\vec{R}_0, S)$ (32)

emphasize the path dependent nature of this time function. The expression

$$t(\vec{R}_0, S) = \text{constant} \quad (33)$$

identifies the position of any particle on its path at some time equaling a constant. The locus of these positions for all particles \vec{R}_0 , is a time line in continuum mechanics. Equation (33) is the mathematical expression for a time line. For a steady incompressible flow, the level curves of this time function are identical with the concept defined by Equation (6) in Chapter II. Equation (33) expresses the relationship between the path lines, the velocities on the path lines, and the time lines.

The deformation ellipses are related to the path lines, time lines, and the velocities on the path lines which are assumed to be known. As shown in Figure 19 the identifying surface,

$$x(x_1, x_2) = \text{constant}$$

is chosen normal to the flow direction. The differential length δ , identifying the neighborhood of points about \vec{R}_0 is small compared to the radius of curvature characterizing the change in the path line and the radius of curvature characterizing the change in the time line at \vec{R}_0 .

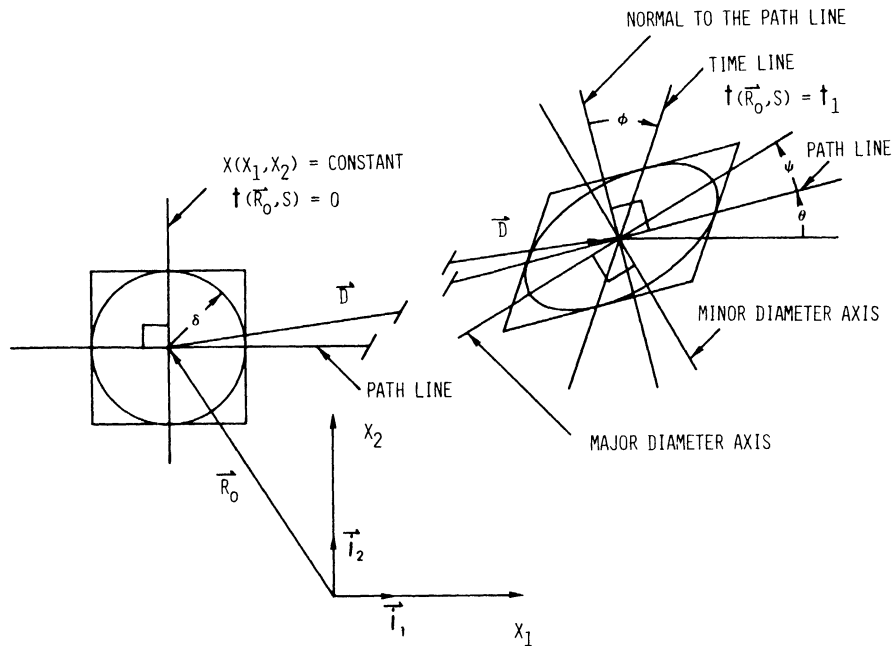


Figure 19 Schematic distortion of ellipse showing important parameters

These characteristic radii of curvature of the time line and path line represent the magnitude of the second order differential geometrical relations for the neighborhood of points. The differential length δ , is chosen to be small compared to these characteristic radii for an displacement, \vec{D} , of interest. That is to say that the changes in the relative displacements within this neighborhood are sensibly homogenous, are of first differential order, and that these changes are described locally by linear transformations. Within this neighborhood, by virtue of these linear transformations, any straight line is transformed into a straight line and any ellipse is transformed into an ellipse. These relative displacements describe the strained neighborhood and the ellipses characterizing the deformations are called strain ellipses.

The descriptions of the strained neighborhoods proceed from the

$$x(x_1, x_2) = \text{constant},$$

time equal zero surface. By definition, this is the zero strain state surface. For two dimensional flow, the zero strain state ellipse is the circle. If the zero strain surface is to represent all previous strain history, the path lines and the velocities along the path lines must be consistent with the motion of a rigid body previous to the intersection of the path lines and the zero strain surface.

The condition of incompressibility assures that volume is conserved, that is

$$L_0 A_0 = L_1 A_1 \quad (34)$$

in terms of a differential length L , along the path line and a differential area A , normal to the path line. The subscripts 0 and 1 refer to time $t=0$, and some later time $t = t_1$, respectively. In terms of continuity along the path line,

$$\rho V_0 A_0 = \rho V_1 A_1 \quad (35)$$

Since density is constant, from Equations (34) and (35),

$$L_1/L_0 = V_1/V_0 \quad (36)$$

The strain ellipse at time $t=0$, is a circle and is transformed into an ellipse at some later time $t=t_1$. Relative to the path line, this ellipse can be thought to have been formed by two transformations, an elongation and a shear.

If the shear transformation is performed last, the shear angle and the angle between the time line and the normal to the path line are the same. The local coordinate systems, Figure 20, have the same scale as

the x_1, x_2 coordinates in Figures 9, 10, 11 and 19. The $\zeta_1, \eta_1,$ and μ_1 axis together with their respective unit vectors $\vec{l}_1, \vec{m}_1,$ and \vec{n}_1 are tangent to the path line. The $\zeta_2, \eta_2,$ and μ_2 axis together with their respective unit vectors are normal to the path line.

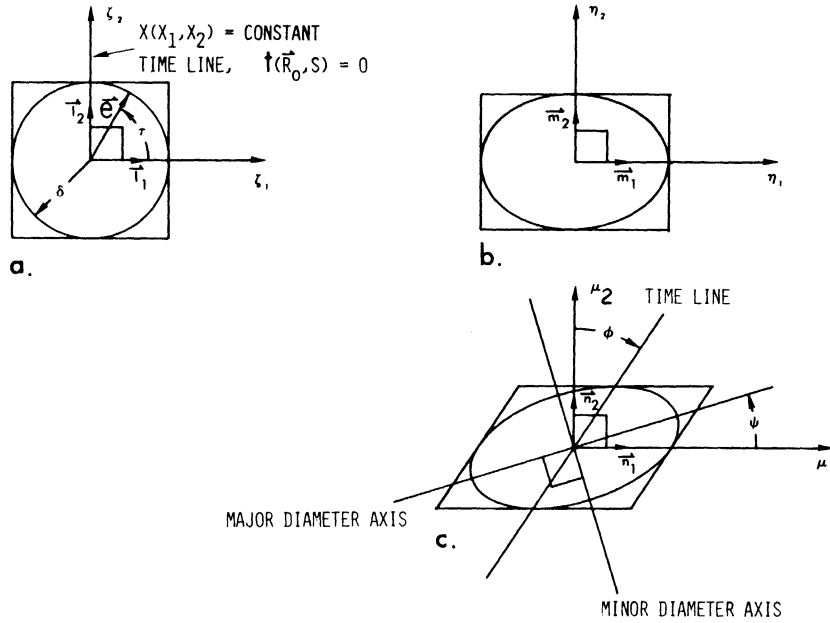


Figure 20 Local coordinate systems ζ and μ ; Intermediate transformation coordinate system η

The ellipse at time, $t = 0$, is a circle,

$$\vec{e} = \zeta_1 \vec{l}_1 + \zeta_2 \vec{l}_2 \tag{37}$$

where

$$\zeta_1 = \delta \cos \uparrow$$

$$\zeta_2 = \delta \sin \uparrow,$$

or

$$\vec{e} = \delta (\cos \uparrow \vec{l}_1 + \sin \uparrow \vec{l}_2) . \tag{38}$$

The first transformation is a simple elongation with respect to the pathline,

$$\eta_1 = a_T \zeta_1 \quad , \quad (39)$$

$$\eta_2 = (1/a_T) \zeta_2 \quad .$$

The transformation constant is defined from Equation (36)

$$a_T = L_1/L_0 \quad . \quad (40)$$

The second transformation is a simple shear with respect to the pathline

$$\mu_1 = \eta_1 + b_T \eta_2 \quad , \quad (41)$$

$$\mu_2 = \eta_2 \quad .$$

The second transformation constant is defined

$$b_T = \tan \phi \quad , \quad (42)$$

where ϕ is the shear angle shown in Figures 19 and 20. The ellipse in terms of the first transformation is,

$$\vec{e} = \delta (a_T \cos \uparrow \vec{m}_1 + (1/a_T) \sin \uparrow \vec{m}_2) \quad . \quad (43)$$

The final expression for the ellipse after both transformations is

$$\vec{e} = \delta [(a_T \cos \uparrow + (b_T/a_T) \sin \uparrow) \vec{n}_1 + (1/a_T) \sin \uparrow \vec{n}_2] \quad . \quad (44)$$

Since the Jacobians for transformations represented by Equations (39) and (41) are equal to one, the area of neighborhood δ is conserved.

The semi-major diameter d_1 , and the semi-minor diameter d_2 , of the final ellipse as described by Equation (44) are

$$d_{1,2} = \sqrt{2\delta} / (c \mp \sqrt{c^2 - 4})^{1/2}, \quad (45)$$

where d_1 and d_2 are defined by the minus sign and the plus sign respectively and where

$$c = a_T^2 + [(b_T^2 + 1)/a_T^2]. \quad (46)$$

The angle ψ from the path line to the major diameter axis is

$$\psi = (\pi/8)\Gamma(1-\Theta)(1-\Xi) + 1/2 \arctan[2b_T/(a_T^4 + b_T^2 - 1)] \quad (47)$$

where

$$\Gamma = b_T/|b_T|,$$

and $\Gamma = 1$ when $b_T = 0$,

where $\Theta = (a_T - 1)/|a_T - 1|$

and $\Theta = 1$ when $a_T = 1$,

where $\Xi = (a_T^4 + b_T^2 - 1)/|a_T^4 + b_T^2 - 1|$

and $\Xi = 1$ when $a_T^4 + b_T^2 = 1$.

The strain ellipse as described by Equations (44), (45), (46), and (47) together with the angle of rotation θ , of the path line relative to the x_1 axis, is completely determined. This strain ellipse describing the deformed neighborhood of points is completely determined for any shear angle

$$-90^\circ < \phi < 90^\circ,$$

and any extension

$$0 < a_T < \infty,$$

where $0 > a_T > 1$ describes contractions with respect to the path line.

The maximum and minimum principal natural strains ϵ_1 and ϵ_2 respectively, are defined

$$\epsilon_1 = \log_e (d_1/\delta), \quad (48)$$

and

$$\epsilon_2 = \log_e (d_2/\delta). \quad (49)$$

The ϵ_1 and ϵ_2 principal strain axes relative to the path line are defined by ψ and $\psi+\pi/2$ respectively. The ϵ_1 and ϵ_2 principal strain axes relative to the fixed X_1 axis are $\psi + \theta$ and $\psi + \theta + \pi/2$ respectively, as indicated in Figure 19. The natural elongation in the strained state for any line at angle \uparrow in the unstrained state is

$$\epsilon = \log_e (|\vec{e}|/\delta) \quad (50)$$

where \vec{e} is defined as in Equation (44).

The path lines, the velocities along the path lines, and the time lines defined or discussed in this section are for general two dimensional continuous flows. The strain ellipse is defined relative to the path line for general two dimensional incompressible flows and these kinematic concepts describe the flow from a Lagrangian point of view.

COMPUTER IMPLEMENTED MODEL OF PERFECT FLUID DEFORMATION IN THE SELECTED SELECTED REFERENCE FRAME

Since the path lines and the velocities along the path lines are known for the steadily flowing perfect fluid in the geometry of Figures 12 and 13, the kinematic variables from a Lagrangian point of view for this flow are defined. The purpose of this section is to present the method of evaluation and the method of graphically representing these kinematic variables. The digital computing facilities at the University

of Michigan⁽⁴¹⁾ are used to implement the evaluation and graphical procedures. This presentation is limited to the algorithms used and the results of these algorithms; however, the program listings and example non-graphical output are presented in Appendix D. This manner of presentation is used for all computer aided procedures presented in the text of this dissertation.

The incremental array of perfect fluid path lines used to define the time function is shown in Figure 21 where the time function for the flow field is incrementally defined by numerically integrating Equation (31) along each perfect fluid path line in the array shown. The index I identifies the particular path line, while the index J identifies the particular position along each path line. Each point on a path line has an image in

1. the physical plane, $z(I,J)$
2. the complex potential plane, $p(I,J)$
3. the Schwarz Christoffel half plane, $w(I,J)$
4. the rationalizing plane, $s(I,J)$
5. the velocity plane, $q(I,J)$.

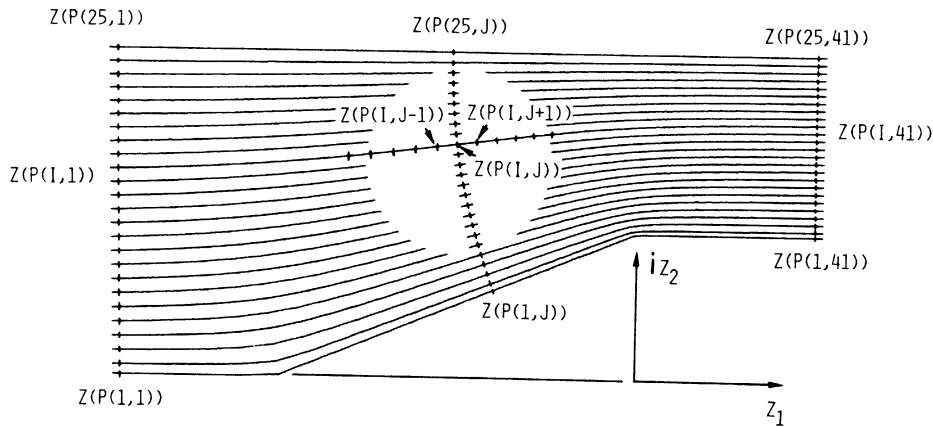
The path lines (stream lines) are defined in the complex potential plane,

$$\begin{aligned}
 p_2(1) &= 0 \\
 p_2(2) &= K_1 \\
 p_2(I) &= N(K_2) + K_1
 \end{aligned}
 \tag{51}$$

where $N = I-2$, and $I = 3, \dots, 25$

resulting when $I = 25,$

in $p_2(25) = V_A \pi$.



Semi-die angle: $\gamma = 22.5^\circ$

Outlet to inlet
dimension ratio: $H = 0.549$

Reduction in area: $R = 0.451$

Figure 21 Incremental array of perfect fluid path lines used to define the time function in the physical plane

The resulting path lines from this definition correspond to dividing the experimental streamtubes in Figure 9 into fourths in the limit up and down stream from the tapered die section. Every fourth path line defined by Equation (51) corresponds with an experimental path line in the limit up and down stream. The positions along the path lines are also defined in the complex potential plane,

$$p_1(J) = p_1'(I) + M(K_3)$$

where

$$M = J - 1 \quad \text{and} \quad J = 1, 2, \dots, 41. \quad (52)$$

When $J = 1$,

$$p_1(1) = p_1'(I)$$

The index, I , in $p_1(I)$ identifies the starting point along each path

line as being uniquely determined for that path line. The $p_1(I)$'s are determined by the intersection of the time equaling zero line in the physical plane with the perfect fluid path lines. The time equaling zero line for the perfect fluid is chosen to correspond to the experimentally selected time line between circles numbered 199, 200, . . ., 209, 210 and circles numbered 217, 218, . . ., 227, 228 in Figure 9. This selected time line facilitates the comparison of the perfect fluid deformation field with the real metal deformation field. The points plotted in Figure 21 are defined

$$z(I,J) = z(p(I,J)) \quad (53)$$

indicating the functional character of this definition. Path lines are represented by the straight line segments between the images of path line points in the physical plane as shown in Figure 21.

The velocity of the perfect fluid particle at each point in Figure 21 is defined

$$q(I,J) = q(p(I,J)). \quad (54)$$

Equation (54) defines the images of the perfect fluid path lines in the velocity plane, (See Figure 18.) As in Equations (51), (52), and (53), the index I identifies a path line and the index J indicates a position along the path line. Functional subprograms are defined for the functions as represented by Equations (53) and (54), (See ZF and QF, Subprograms, Appendix D.) An increment of time is defined using the trapezoidal rule between points on a path line $z(I,J)$ and $z(I,J+1)$, (See DT, Subprograms, Appendix D.),

$$\Delta t = 1/2 \left[\left(\frac{1}{|q(I,J)|} \right) + \left(\frac{1}{|q(I,J+1)|} \right) \right] \left[|z(I,J+1) - z(I,J)| \right] \quad (55)$$

Starting with $t(I,1) = 0$ and summing the time increments along the incremental perfect fluid path line, each point on the path line $z(I,J)$ is assigned a time $t(I,J)$. Upon integration along the entire array of incremental perfect fluid path lines, the time function for the steady flow field is determined for the array shown in Figure 21.

A new variable is employed to determine the level curves of this time function. The new variable defined for the flow field is

$$it(I,J) = \text{integer} (t(I,J)/\Delta t), \quad (56)$$

where

$$\Delta t = V_A \pi / 12$$

if twice as many level curves are desired as those shown in Figure 9.

This conversion from a real number to an integer drops all digits after the decimal. While traveling downstream on path line I, if

$$it(I,J) + 1 = it(I,J+1),$$

the time function has acquired the value

$$t = N\Delta t$$

where

$$N = it(I,J+1)$$

in the interval between $z(I,J)$ and $z(I,J+1)$. The position

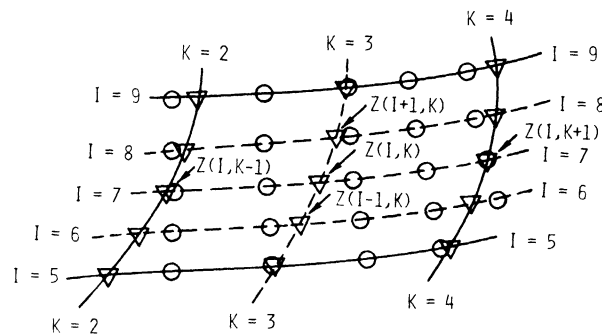
$$z(I,K) = \left[\frac{t - t(I,J)}{t(I,J+1) - t(I,J)} \right] \left[z(I,J+1) - z(I,J) \right] + z(I,J) \quad (57)$$

where

$$K = it(I,J+1),$$

is defined at the location where the time function $t = N\Delta t$, (See RINT, Subprograms, Appendix D.) That is to say that the position $z(I,K)$ is

determined by the linear interpolation with respect to time along the straight line segment between $z(I,J)$ and $z(I,J+1)$, and the index K identifies the position where level curve K intersects path line I . All values of $t(I,J)$ are examined in this manner, which determines the array of positions $z(I,K)$. The index K is thus associated with particular time lines. The time lines are represented by straight line segments between the images of time line points in the physical plane as shown in Figure 22.



$z(I,K)$ are time line segments, when K is constant

$z(I,J$ or $K)$ are path line segments, when I is constant

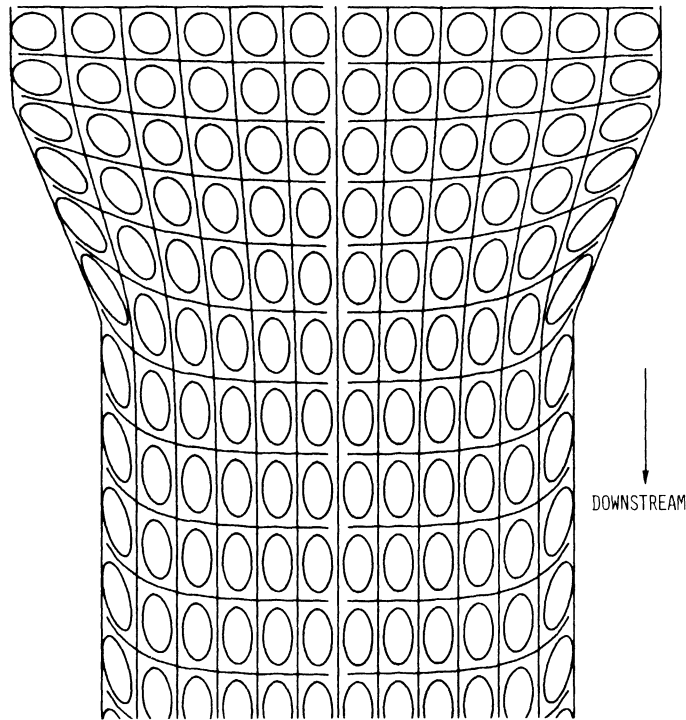
Figure 22 Example array of $z(I,J)$ and $z(I,K)$ positions

An example array of $z(I,K)$ and $z(I,J)$ positions is shown in Figure 22, where time lines are defined for $z(I,K)$ when K is a constant integer, and path lines are defined for $z(I,J)$ or $z(I,K)$ when I is a constant integer. In the limit up or down stream from the tapered section the $I = 5$ and the $I = 9$ perfect fluid path lines are straight and correspond to the first and second experimentally selected path lines in from the wall as shown in Figure 9. The perfect fluid time lines $K=2$ and $K=4$ correspond to the same time line increment as shown in Figure 9. There are twice as many perfect fluid time lines as experimentally selected time lines. The additional time lines are used to determine

strain ellipses. In Figure 22 the solid lines correspond to those selected experimental lines shown in Figure 9.

To implement the computer aided plots of the time lines and the path lines in the format of those kinematic variables shown in Figure 9, every fourth perfect fluid path line and every other perfect fluid time line is plotted, (See Perfect Fluid Deformation Field Computation and Plot, Appendix D.) The plotting is done on a CALCOMP 780/763 digital plotter from plot descriptions generated on the IBM 360 model 67 computer at the University of Michigan. (42)

The perfect fluid deformation field resulting from the computer aided plot is shown in Figure 23; this field includes strain ellipses.



Semi- die angle: $\gamma = 22.5^\circ$
 Reduction in area: $R = 0.276$

Outlet to inlet
 dimension ratio: $H = 0.724$

Figure 23 Perfect fluid deformation field

Each strain ellipse is plotted using similar information as that represented in Figure 22, together with the velocity vector at the center of the deformed squares. In Figure 22 the center of the deformed square is

$$z(I,K) = z(7,3)$$

and the velocity vector in the complex form is

$$q(I,K) = q_1(7,3) + iq_2(7,3)$$

The inclination of the path line to the z_1 axis at point $z(I,K)$, (Angle θ , see Figure 19.) is determined from the velocity vector, since this vector is tangent to the path line at point $z(I,K)$. The elongation ratio (the transformation constant " a_T ", Equation (40)) is determined from the velocity $q(I,K)$,

$$a_T = |q(I,K)|/V_A . \quad (58)$$

The tangent to the segmented time line at $z(I,K)$ is represented by the directed time line segment in complex form,

$$z(I+1,K) - z(I-1,K) = z(8,3) - z(6,3) \quad (59)$$

The angle between this directed time line segment and the normal to the path line at $z(I,K)$ is shear angle ϕ . From the shear angle ϕ , the transformation constant is determined,

$$b_T = \tan \phi . \quad (42)$$

The untransformed radius δ , is selected to represent strain ellipses intermediate in size between those strain ellipses that would result from the concentric circles in the selected grid system discussed in Chapter II. The collection of strain ellipses plotted at the centers of the array of deformed squares is shown in Figure 23. The major and minor

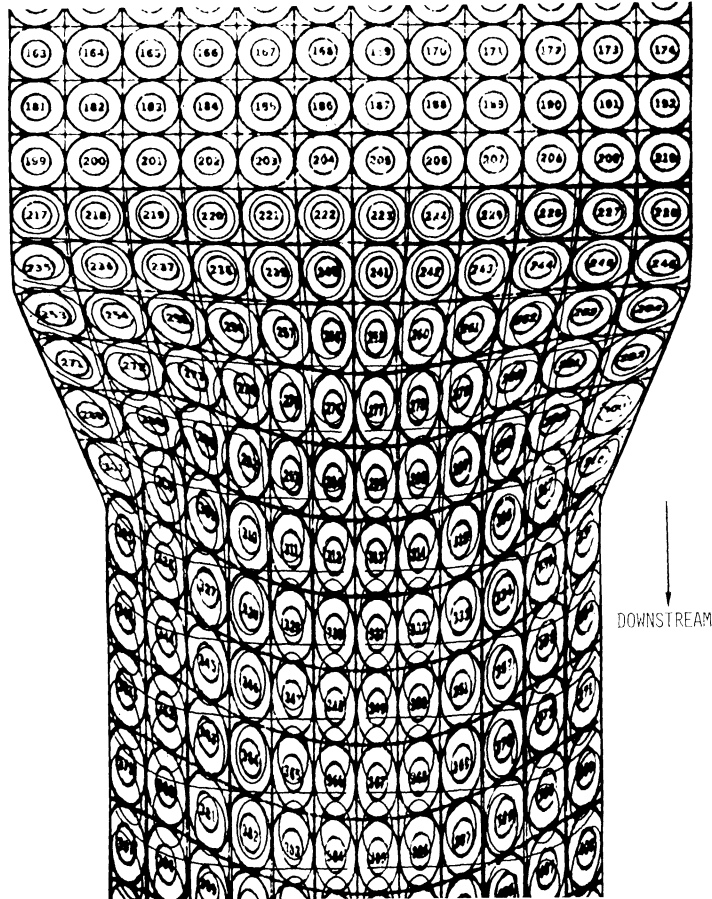
diameters together with the major diameter axes are determined from the representative array of points associated with each deformed square in a manner analogous to the example for the array of points shown in Figure 22. This collection of strain ellipses is an incremental representation of the strain field for the flowing perfect fluid. The kinematic variables for the steadily flowing perfect fluid, i.e., (1) the path lines, (2) the time lines, (3) the strain ellipses are presented in Figure 23 in the same format as the experimentally determined kinematic variables of the real metal deformation field shown in Figure 9. Both this analytical and the experimental deformation fields are defined and interpreted from the Lagrangian point of view.

COMPARISON OF THE DEFORMATION FIELD OF A PERFECT FLUID WITH THE DEFORMATION FIELD OF A REAL METAL

The deformation field of Figure 23 is superimposed on the deformation field of Figure 9 in Figure 24. The composite in Figure 24 allows the perfect fluid deformation field to be compared to the real metal deformation field of 6061-0 Aluminum. The selected time equaling zero line for the perfect fluid corresponds to the line between circles numbered 199, 200, . . . , 209, 210 and circles numbered 217, 218, . . . , 227, 228 of the real metal deformation field. This selected time line does not define a zero strain state for the perfect fluid, since the motion of the perfect fluid is not entirely consistent with that of a rigid body previous to the selection time line. However, the selected time line can be said to identify both perfect fluid particles and real metal particles at equal time intervals and at the same location in the flow field. Subsequent deviations in location between the real metal time lines and the perfect fluid time lines as shown in Figure 24

represent the kinematical differences in the flow fields. The time increments in the perfect fluid deformation field have been corrected to account for the effect of foreshortening in the real metal deformation field, (See Table V.),

$$\Delta t \text{ corrected} = L\Delta t. \quad (60)$$



Semi-die angle: $\gamma = 22.5^\circ$

Reduction in area: $R = 0.276$

Outlet to inlet

dimension ratio: $H = 0.724$

Material: 6061-0 aluminum

Figure 24 Perfect fluid deformation field superimposed on the real metal deformation field. (Note that the real metal deformation field has numbered ellipses.)

The perfect fluid flows steadily with a velocity field that is described as irrotational, whereas the real metal flows steadily in this extrusion process with a velocity field that is described as rotational. Whether a velocity field is rotational or irrotational depends on the vorticity of the velocity field. The vorticity is defined by the vector operator,

$$\vec{\omega} = 1/2 \text{ curl}(\vec{V}) \quad (61)$$

where \vec{V} is a general velocity field. For an irrotational velocity field the vorticity is everywhere equal to zero. Since vorticity is defined at a point fixed in space, vorticity is defined from an Eulerian point of view.

From a Lagrangian point of view the effects of the rotationality of the real metal velocity field manifest themselves in the deviations between the families of time lines and path lines of the real metal deformation field and those same families of lines in the irrotational perfect fluid deformation field. The measure of rotationality for the real metal flow field is selected to be the deviations of the real metal path line from the perfect fluid path line, when both path lines would be coincident in the limit upstream and downstream from the tapered die section. The effects of the rotationality are now defined as a function of time along the real metal path line and therefore, the selected measure of rotationality fulfills the requirements of a Lagrangian measure.

The environment of the extruding aluminum is that of a cold extrusion, i.e., the 0.5 inch per minute ram speed results in a negligible increase in billet temperature above room temperature. The environment of the perfect fluid is conceptual and is assumed to be compatible with

that of the extruding aluminum, i.e., the perfect fluid flows steadily in a similar geometry. The flowing aluminum is subject to frictional effects at the die and container walls, but the flowing perfect fluid is inviscid. Aluminum has all the properties of a metal, e.g., density, hardness, yield strength, shear strength, tensile strength, elasticity, ductility, etc. With respect to the large deformations encountered in this extrusion process, the aluminum is assumed to be incompressible and though the flowing perfect fluid is inviscid, it is also incompressible with density. Therefore, within the given extrusion environment, relations between the frictional effects and those metallic properties other than density and incompressibility which can account for the deviations between the families of path lines, remain to be determined.

MODELED REAL METAL PATH LINES

The Lagrangian model of the real metal flow field requires that the real metal path lines are modeled. To accomplish this, these lines are described in terms of the normalized complex variable r , where

$$r = r_1 + ir_2 \quad (62)$$

Real metal path lines are defined when,

$$r_2 = \text{constant} \quad (63)$$

and the position along a real metal path line is determined by a value of r_1 . Figure 25 shows the schematic relationship between the perfect fluid path lines, the real metal path lines, and the perfect fluid potential lines.

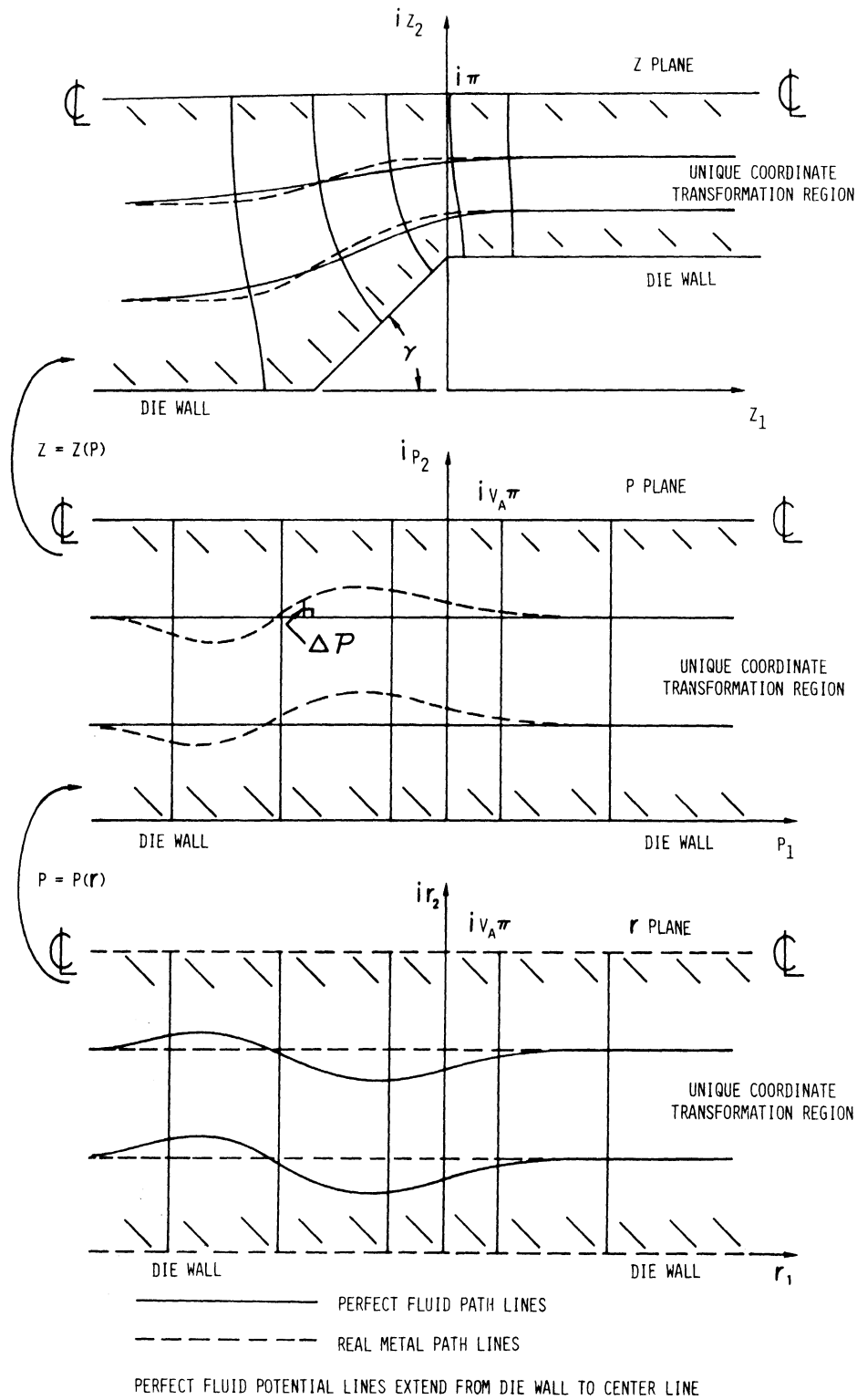


Figure 25 Schematic representation of perfect fluid potential lines, real metal path lines, and perfect fluid path lines in the z, p, and r planes

The explicit relation,

$$z = z(p)$$

is defined by Equations (12), (16), and (21), while the explicit relation between the r plane and the complex potential plane p , is

$$p = p(r) \quad (64)$$

where

$$p_1 = r_1,$$

and

$$p_2 = p_2(r_1, r_2)$$

or

$$p_2 = r_2 + \Delta P. \quad (65)$$

The flow of a real metal is rotational during the extrusion process and no conformal representation can exist for the path lines (stream lines) of a steady rotational flow. Thus, Equations (64) and (65) are not conformal representations of the transformation from the r plane to the p plane.

The real metal path line and the perfect fluid path line are coincident at the center line, at the die wall, and in the limit upstream and downstream from the tapered die section (See Figure 24.) That is,

$p_2(r_1, r_2)$ has the following constraints:

$$\lim_{r_1 \rightarrow \pm\infty} p_2(r_1, r_2) = r_2, \quad (66)$$

$$\lim_{r_2 \rightarrow V_A \pi} p_2(r_1, r_2) = V_A \pi,$$

and

$$\lim_{r_2 \rightarrow 0} p_2(r_1, r_2) = 0.$$

If $p_2(r_1, r_2)$ is expressed by Equation (65), ΔP must be equal to zero at the center line, at the die wall, and in the limit up and downstream from the tapered die section. That is, ΔP has the following constraints:

$$\lim_{r_1 \rightarrow \pm\infty} \Delta P = 0 , \quad (67)$$

$$\lim_{r_2 \rightarrow V_A \pi} \Delta P = 0 ,$$

and

$$\lim_{r_2 \rightarrow 0} \Delta P = 0 .$$

The functional notation

$$p = p(r)$$

implies a coordinate transformation which, if it is to be unique, i.e., one-to-one, the following constraint must be met. As r_2 increases monotonically from 0 to $V_A \pi$, $p_2(r_1, r_2)$ must increase monotonically from 0 to $V_A \pi$ for any value r_1 . That is, from Equation (65),

$$\partial p_2(r_1, r_2) / \partial r_2 > 0 \quad (68)$$

or

$$\partial \Delta P / \partial r_2 > -1 .$$

Equations (66), (67), and (68) express constraints on the functional relation,

$$p = p(r) .$$

$$\text{Let } \Delta P = [p_2(r_1, r_2) - p_2(1)] \Big|_{r_1} = \text{constant} \quad (69)$$

where

$$p_2(1) = \lim_{r_1 \rightarrow \pm\infty} p_2(r_1, r_2) = r_2 .$$

This definition of ΔP satisfies constraint Equation (67). The perfect

fluid path line $p_2(1)$, is coincident with the real metal path line r_2 , in the limit up and down stream from the tapered die section. ΔP is measured along the perfect fluid potential line, since

$$p_1 = r_1 .$$

The perfect fluid potential line p_1 , is orthogonal to the perfect fluid path line $p_2(1)$. ΔP represents the difference in position in the complex potential plane between the real metal path line r_2 , and the perfect fluid path line $p_2(1)$. Therefore, ΔP is the selected Lagrangian measure of rotationality for the real metal velocity field of this extrusion process.

ΔP is defined in the complex physical plane and the coordinate system shown in the right-hand side of Figure 12 facilitates the determination of positions in the physical plane in terms of complex potential plane coordinates. Since every fourth perfect fluid path line in Figure 12 is coincident with the real metal path lines of Figure 9 in the limit up and down stream, when the incremental array of real metal path lines in Figure 9 is superimposed on the right-hand coordinate system of Figure 12, the values of ΔP can be experimentally determined.

Deviations of the real metal path lines from the perfect fluid path lines as shown in Figure 24 have a regular pattern on traveling downstream. The real metal path line first deviates toward the die wall and then deviates toward the center line. In Figure 26 is shown a schematic plot of these regular deviations in terms of the experimentally determined ΔP 's. The model selected for the experimental ΔP 's has the form,

$$\Delta P_m = A - B , \quad (70)$$

where
$$A = A/(a(r_1 - \alpha)^2 + e^{-c_1(r_1 - \alpha)}) \quad (71)$$

and
$$B = B/(b(r_1 - \beta)^2 + e^{c_2(r_1 - \beta)}). \quad (72)$$

Modeling ΔP is equivalent to modeling the real metal path lines.

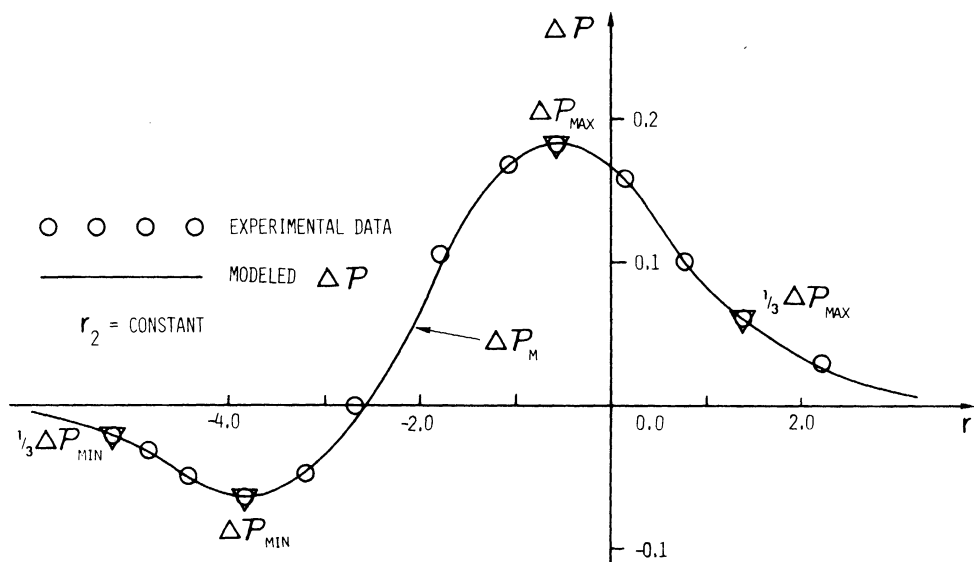


Figure 26 Schematic representation of the difference between the perfect fluid path lines and the real metal path lines ΔP .

The synthesis of function A is diagrammed in Figure 27. The four coefficients A , a , α , and c_1 are closely related to different geometric properties of the nonlinear function A . The coefficient A , is closely related to the maximum value of A and the coefficient a , is closely related to the decay for increasing values r_1 from the maximum in the function A . The coefficient α , is closely related to the location r_1 , of the maximum in the function A , while the coefficient c_1 is related to the skewed symmetry of the function A . The function B is similar to the function A except for the opposite sign in skewed symmetry term. When the coefficient β , is less than the coefficient α , the synthesis of the model for ΔP is shown in Figure 28.

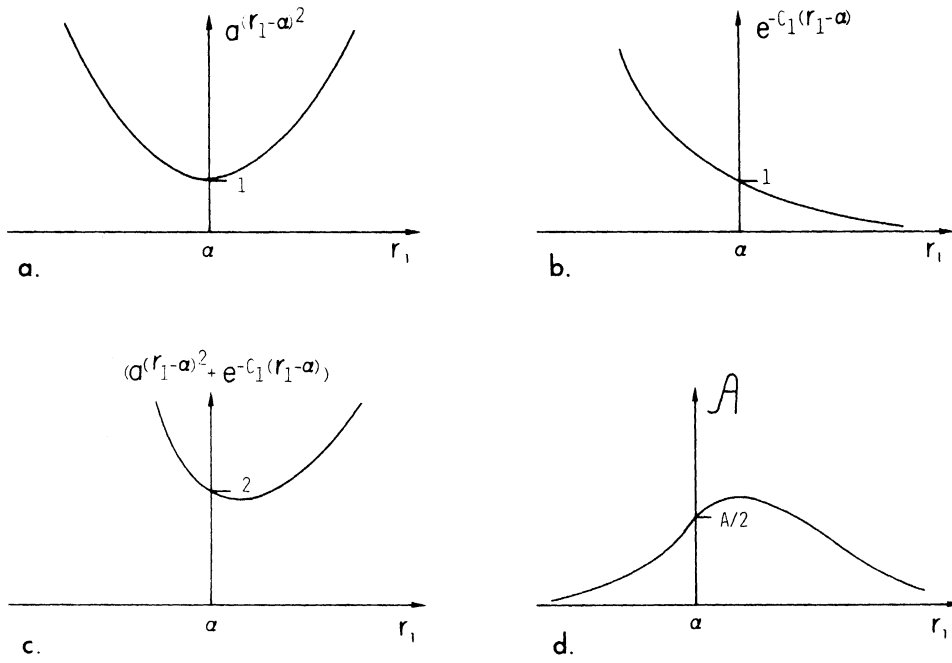


Figure 27 Schematic synthesis of function A

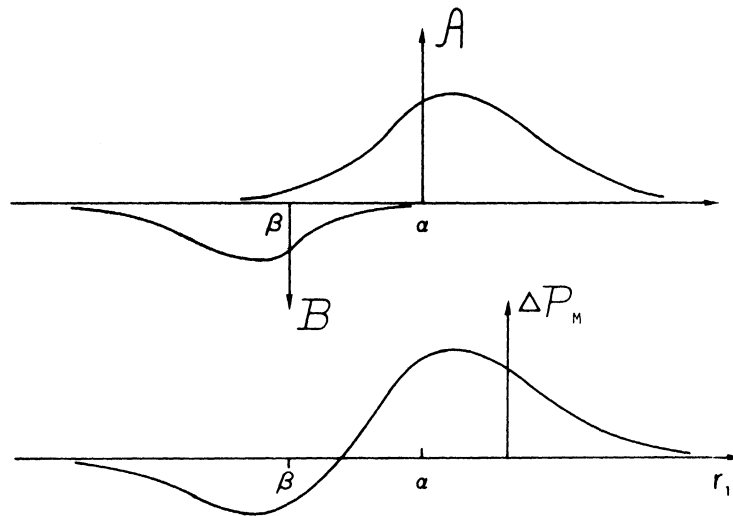


Figure 28 Schematic synthesis of function ΔP_m .

Since

$$\Delta P \doteq \Delta P_m,$$

the modeled real metal path lines have the form, $p_1 = r_1$, (64)

and

$$p_2 = r_2 + \Delta P_m. \tag{73}$$

Alternate models exist for the experimental ΔP 's, but the relative accuracy of these models is not within the scope of this investigation. The accuracy of the selected model is assayed by comparing the real metal deformation field with the resulting modeled real metal deformation field.

The coefficients for ΔP_m are determined from the location of the four experimentally determined points ΔP_{\max} , ΔP_{\min} , $1/3\Delta P_{\max}$, and $1/3\Delta P_{\min}$ as shown in Figure 26, together with the constraints that

$$\left. \frac{d\Delta P_m}{dr_1} \right|_{\Delta P_{\max}} = 0 \quad (74)$$

and

$$\left. \frac{d\Delta P_m}{dr_1} \right|_{\Delta P_{\min}} = 0. \quad (75)$$

When Equation (73) is evaluated at the four experimental points, and when Equation (74) and (75) are evaluated at ΔP_{\max} and ΔP_{\min} respectively, the resulting six nonlinear equations can be solved for six of the eight coefficients in ΔP_m , if two of the coefficients are known. The skew symmetric coefficients c_1 , and c_2 are selected to meet two criteria. The first criterion is that the nonlinear equation solving algorithm used in the computer program converges, (See Experimental Modeling Coefficients Computations, Appendix D.) whereas the second is that the resulting ΔP_m is representative of the flow field. The decision with respect to the satisfaction of the second criterion is made by comparing the resulting modeled real metal deformation field with the real metal deformation field; a schematic representation of the modeled ΔP 's, ΔP_m , is shown in Figure 26. The selected skewed symmetry coefficients c_1 and c_2 are geometrically most closely related to the fit of the model ΔP_m , between ΔP_{\min} and ΔP_{\max} .

The nonlinear equation solving computer program is typical in that an initial estimate of the resulting model coefficients must be made. If the initial estimate is not sufficiently close to the final result, the computational algorithm may not converge. The geometric relationship between the experimental values of ΔP and the model coefficients is useful in making the initial estimates of the model coefficients. After some experience is gained with the successful solution of the set of nonlinear equations, plots of the resulting coefficients versus their most closely related geometrical properties are additionally useful in making initial estimates.

The experimental points for determining the model coefficients for the five interior path lines of the real metal deformation field in Figure 9 are tabulated in Table VI. The resulting coefficients A , a , α , B , b , and β from the nonlinear equation solving computer programs are tabulated in Table VII, when the selected skewed symmetry terms have values

$$c_1 = (4/\pi)r_2+1 \quad \text{and} \quad c_2 = (4/\pi)r_2+3.$$

The modeled coefficients are a function of the real metal path line, r_2 . In Figure 29 the model coefficients are plotted as a function of the path line, r_2 . These five interior values for the model coefficients are calculated from experimentally determined information. The values of the model coefficients at the die wall, $r_2 = 0$ and at the center line, $r_2 = \pi$ are not determined directly from the experimentally evaluated ΔP 's, but since ΔP is equal to zero at the die wall and center line, to insure that the modeling deviations ΔP_m , are also equal to zero, the values of the model coefficients A and B are extrapolated to zero at the die wall and center line, (See Figure 29 and Equations (70), (71), and (72).) With

these extrapolations on model coefficients A and B, the model deviation function ΔP_m , meets constraint Equation (67). The die wall value of α and β are determined by a linear extrapolation of the first two experimentally determined coefficients adjacent to the die wall. The other extrapolated values of the model coefficients at the die wall or the center line are set equal to the value of the coefficient adjacent to the die wall or center line, respectively. The resulting modeled deviations ΔP_m now meets the constraint equations and the extrapolated coefficients form a completed set.

TABLE VI
EXPERIMENTAL POINTS FOR DETERMINING MODEL COEFFICIENTS

Die Geometry:	R = 0.276 H = 0.724 $\gamma = 22.5^\circ$					
Material:	6061 aluminum					
Normalized Upstream Velocity:	$V_A = 1.0$					
Lubrication:	(See Lubrication, Chapter II)					
r_2	ΔP_{\max}	$r_1(\Delta P_{\max})$	ΔP_{\min}	$r_1(\Delta P_{\min})$	$r_1(1/3\Delta P_{\max})$	$r_1(1/3\Delta P_{\min})$
0.468	0.100	-0.320	-0.0240	-2.733	0.980	-4.033
1.003	0.160	-0.670	-0.0263	-2.983	0.698	-4.283
1.538	0.173	-0.980	-0.0243	-3.109	0.455	-4.409
2.072	0.140	-1.220	-0.0221	-3.203	0.283	-4.503
2.607	0.077	-1.450	-0.0166	-3.210	0.120	-4.510

TABLE VII
MODEL COEFFICIENTS

Die Geometry:	R = 0.276 H = 0.724 $\gamma = 22.5^\circ$					
Material:	6061-0 aluminum					
Normalized Upstream Velocity:	$V_A = 1.0$					
Lubrication:	(See Lubrication, Chapter II)					
Experimental Points:	(See Table VI)					
Skewed Symmetry Coefficients:	$c_1 = (4/\pi)r_2+1, c_2 = (4/\pi)r_2+3$					
r_2	A	a	α	B	b	β
0.468	0.155	1.513	-0.939	0.0407	1.421	-1.945
1.003	0.222	1.421	-1.315	0.0387	1.430	-2.264
1.538	0.223	1.371	-1.614	0.0324	1.442	-2.467
2.072	0.172	1.338	-1.830	0.0271	1.465	-2.656
2.607	0.090	1.313	-2.033	0.0196	1.480	-2.712

An interpolative definition of the modeled real metal path line for any path line desired is defined using the complete set of model coefficients. Interpolation by piece-wise cubic splines is the method of approximation used to define the model coefficients between experimentally calculated values for any value of real metal path line, (See Cubic Spline Fit, Appendix D.) The resulting cubic splines are plotted in Figure 29. The interpolated model coefficients equal the experimentally

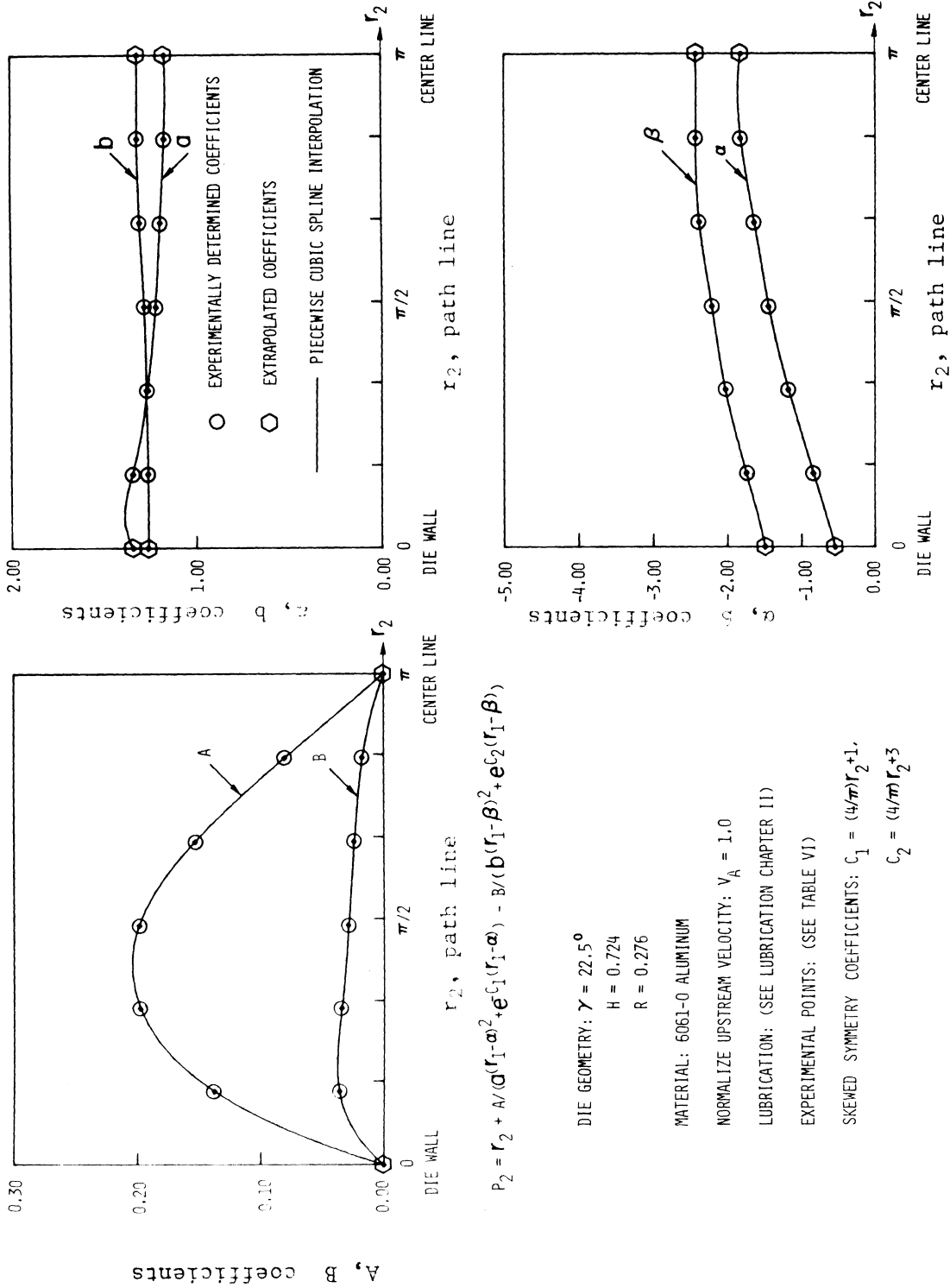


Figure 29 Model coefficients versus real metal path line

determined and extrapolated values of the model coefficients when the selected real metal path line coincides with one of the experimental path lines in Figure 9. The interpolated model coefficients are continuous and possess continuous first and second derivatives with respect to r_2 ; the functions representing a perfect fluid are continuous and their derivatives of all order are continuous. The modeled deviation function ΔP_m , is continuous and its derivatives with respect to r_1 of all order are continuous, therefore, the modeled real metal path lines are continuous and the partial derivatives of this model are continuous at least through the second order. The modeled path lines meet the requirements for a continuum.

The model coefficients and the first derivative of the model coefficients with respect to any value r_2 are defined by a subroutine subprogram DCONS (See DCONS, Subprograms, Appendix D.) This subprogram returns values of the model coefficients and their derivatives when given a value of the real metal path line r_2 . With the model coefficients for a real metal path line, the functional subprogram RM, (See RM, subprograms, Appendix D.) returns the $p_2(r_1, r_2)$ value for the modeled real metal path line when r_1 is given. The functional subprogram RM is the computer implementation of Equation (73). The subroutine subprogram DCONS and the functional subprogram RM are the digital computer methods employed to model the real metal path lines.

MODELED REAL METAL VELOCITY FIELDS

The Lagrangian model of the real metal flow field requires the velocity of the metal particles along their path lines but the velocity of a real metal particle is not directly observable with the split billet technique. For steady flows, the path lines and stream lines are

coincident and when the path function equals a constant, a path line is defined. For a steady flow, the path function and stream function are identically equal and for incompressible, two dimensional and possibly rotational flows, the stream function defines the velocity field. In terms of the path function for the steadily flowing aluminum, the real metal velocity field has the form in the physical plane,

$$v = \frac{\partial r_2}{\partial z_2} \vec{k}_1 - \frac{\partial r_2}{\partial z_1} \vec{k}_2 \quad . \quad (76)$$

The coordinate transformations defined for the z , w , s , p , q , and r planes are unique in each plane for the representative image of the die cavity. Therefore, Equation (65) implicitly defines the unique function,

$$r_2 = r_2(p_1, p_2),$$

and Equations (12), (16), and (21) implicitly define the unique functional relations,

$$p_1 = p_1(z_1, z_2)$$

and

$$p_2 = p_2(z_1, z_2).$$

Now the partials in Equation (76) can have the forms

$$\frac{\partial r_2}{\partial z_2} = \frac{\partial r_2}{\partial p_1} \frac{\partial p_1}{\partial z_2} + \frac{\partial r_2}{\partial p_2} \frac{\partial p_2}{\partial z_2} \quad (77)$$

and

$$\frac{\partial r_2}{\partial z_1} = \frac{\partial r_2}{\partial p_1} \frac{\partial p_1}{\partial z_1} + \frac{\partial r_2}{\partial p_2} \frac{\partial p_2}{\partial z_1} \quad . \quad (78)$$

Let
$$\vec{e}_q = \vec{q} / |\vec{q}| \quad (79)$$

and
$$\vec{e}_{nq} = \vec{k}_3 \times \vec{e}_q, \text{ (vector cross product)} \quad (80)$$

where \vec{k}_3 is the unit normal to the z plane. Then using the Cauchy Riemann conditions on the conformal relationship between z and p planes, together with Equations (77) through (80), Equation (76) becomes,

$$\vec{v} = |\vec{q}| \left(\frac{\partial r_2}{\partial p_2} \vec{e}_q - \frac{\partial r_2}{\partial p_1} \vec{e}_{nq} \right) . \quad (81)$$

Equation (81) is expressed in terms most closely related to the selected reference frame. When r_2 is the modeled real metal path function, Equation (81) represents the modeled real metal velocity field.

If the modeled real metal velocity field is to be evaluated as a function of position along the path line, the expression for $|\vec{q}|$, $\partial r_2 / \partial p_2$, and $\partial r_2 / \partial p_1$ must be expressed as functions of position along the modeled real metal path line. Upon selection of a modeled real metal path line r_2 , and position along this path line r_1 , DCONS together with RM returns the image of this real metal particle in the p plane. From this image in the p plane, the subroutine QF returns the velocity q , of a perfect fluid particle at this position. Since Equations (64) and (73),

$$p_1 = r_1 \quad (64)$$

$$p_2 = r_2 + \Delta P_m(r_1, r_2) \quad (73)$$

implicitly define,

$$r_2 = r_2(p_1, p_2),$$

the partials $\partial r_2 / \partial p_1$ and $\partial r_2 / \partial p_2$, must be evaluated by the techniques

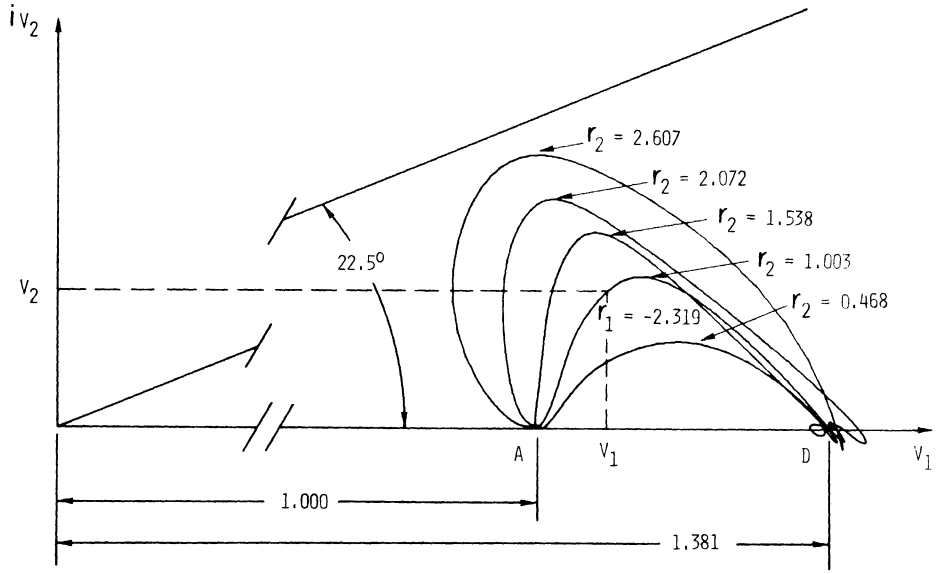
for partial differentiation of implicitly defined functions. The subroutine subprogram PDPRM (See PDPRM, Subprograms, Appendix D.) returns the values for these two partials, when r_1 , r_2 , the model coefficients, and the derivatives of the model coefficients are given. The subroutine subprogram DCONS that has been called to evaluate q , established the values of the model coefficients and their derivatives. From the results of DCONS, RM, QF, and PDPRM the functional subprogram VF (See VF, Subprograms, Appendix D.) returns the value for Equation (81).

Equation (81) expresses the velocity of a real metal particle in terms of the deviation in the velocity of the real metal particle from the velocity of a perfect fluid particle at the same point. These deviations are the direct consequence of the deviations between the modeled real metal and the perfect fluid path lines and the possibly rotational character of the real metal velocity field at the specific point. Since the real metal path line has the implicit form,

$$p_2 = r_2 + \Delta P(r_1, r_2) \quad (65)$$

the deviations in velocity between a real metal particle and a perfect fluid particle at the same point are directly related to the Lagrangian measure of rotationality ΔP , selected for these steady flows.

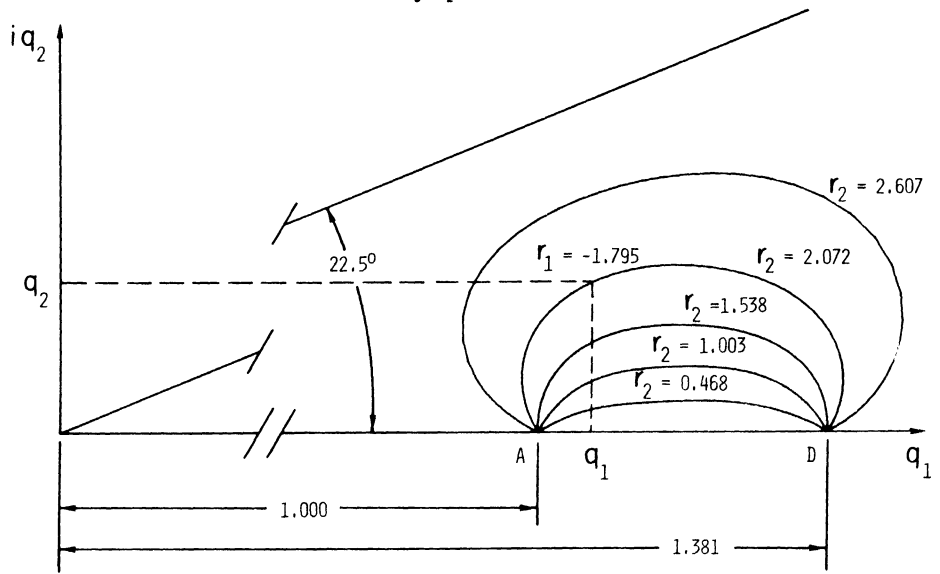
The images of an array of modeled real metal path lines in the modeled real metal velocity plane are shown in Figure 30. The velocity at a particular position along a path line is determined by the coordinate values of that modeled path line point in the modeled real metal velocity plane. An example for a particular path line point is shown in Figure 30, while the images of an array of modeled real metal path lines in the perfect fluid velocity plane are shown in Figure 31.



Semi-die angle: $\gamma = 22.5^\circ$
 Outlet to inlet
 dimension ratio: $H = 0.724$

Reduction in area: $R = 0.276$
 Material: 6061-0 aluminum
 $c_1 = (4/\pi)r_2 + 1$, $c_2 = (4/\pi)r_2 + 3$

Figure 30 Images of an array of modeled real metal path lines in the modeled velocity plane



Semi-die angle: $\gamma = 22.5^\circ$
 Outlet to inlet
 dimension ratio: $H = 0.724$

Reduction in area: $R = 0.276$
 Material: 6061-0 aluminum
 $c_1 = (4/\pi)r_2 + 1$, $c_2 = (4/\pi)r_2 + 3$

Figure 31 Images of an array of modeled real metal path lines in the perfect fluid velocity plane

The differences in Figures 30 and 31 are the results of the modifying partials in Equation (81); the curves shown in Figure 30 are computer generated, (See Modeled Real Metal and Perfect Fluid Velocity Hodograph Plots, Appendix D.) The functions defining the modeled real metal velocity field are continuous; however, differentiation of functions such as ΔP_m which have experimental input tends to magnify experimental errors.

Finite deformations for the modeled real metal flow field can be defined in terms of integrals of strain rates. Strain rate equations require differentiations of the velocity field. This information has included an additional magnification of experimental error with respect to ΔP_m . The time line method for determining finite deformations uses a single integration of the velocity information and integration is a smoothing process. Finite deformations defined by the strain rate method are the result of smoothing operations on information that has a double magnification of experimental error with respect to ΔP_m when compared to finite deformations defined by the time line method.

Constraint Equation (68) insures the uniqueness of the coordinate transformation between the p and r planes.

Since

$$p_1 = r_1 \quad (64)$$

then

$$\partial p_2 / \partial r_2 = 1 / \frac{\partial r_2}{\partial p_2} ,$$

now constrain Equation (68) can be reformulated,

$$\frac{\partial r_2}{\partial p_2} > 0. \quad (82)$$

Upon inspection of Equation (81), Equation (82) can be interpreted as constraining the velocity of a real metal particle to having a component of velocity in the same direction as a perfect fluid particle at the same point. The subroutine subprogram PDPRM that returns the partial derivatives of the modeled real metal path line is used to check to see that constraint Equation (82) is satisfied for the array of points used to define the modeled real metal deformation field in the next section.

COMPUTER IMPLEMENTED MODEL OF REAL METAL DEFORMATION FIELDS

Now the deformation field for the real metal can be modeled. The computer implementation for the deformation field of the modeled real metal is analogous to the computer generated deformation field of the perfect fluid. An incremental array of modeled real metal path lines is used to defined the time function. The time function is defined by integrating scalar Equation (31) along each modeled real metal path line of the array. The modeled real metal path lines are defined,

$$\begin{aligned} r_2(1) &= 0 \\ r_2(2) &= K_1 \\ r_2(I) &= N(K_2)+K_1 \end{aligned} \tag{83}$$

where $N = I-2$, and $I = 3, \dots, 25$

resulting when $I = 25$,

$$r_2(25) = \pi$$

since $V_A = 1.0$ for the real metal flow. The constants K_1 and K_2 are the same as in Equation (51). Therefore, in the limit up and down stream the modeled real metal path line array is coincident with the perfect fluid path line array defined by Equation (51). The index I identifies a particular modeled real metal path line.

The positions along the modeled real metal path lines are defined,

$$r_1(J) = r_1'(I) + M(K_3) \quad (84)$$

where $M = J-1$ and $J = 1, 2, \dots, 41$ and the constant K_3 , is the same as in Equation (52). Index J identifies a position along a path line. When $J = 1$,

$$r_1(1) = r_1'(I).$$

The index I in $r_1'(I)$ identifies the starting point along each path line as being uniquely determined for the modeled real metal path line. The $r_1'(I)$'s are determined by the intersection of the time equaling zero line in the physical plane with the real metal path lines. The time equaling zero line for the model real metal is chosen to correspond to the experimentally selected line between circles numbered 199, 200, . . . , 209, 210 and circles numbered 217, 218, . . . , 227, 228 in Figure 9.

This selected time line facilitates the comparison of the modeled real metal deformation field with both the real metal and the perfect fluid deformation fields in Figures 9 and 23 respectively. The perfect fluid points plotted in Figure 21 have an analog with respect to modeled real metal points when the points in the physical plane are defined,

$$z(I,J) = z(r(I,J)). \quad (85)$$

Equation (85) indicates that the plotted points are defined for a modeled real metal. The path lines are represented by straight line segments between images of modeled real metal path line points in the physical plane. Equation (83) and (84) together with computer subprograms DCONS, RM, AND ZF define the modeled real metal path line points, (See Real Metal Deformation Field Modeling Computation and Plot, Appendix D.)

The velocity of the modeled real metal particle at each point defined by Equation (85) is defined

$$v(I,J) = v(r(I,J)). \quad (86)$$

As in Equations (83), (84), and (85), the index I identifies a path line and the index J indicates a position on a path line. $v(I,J)$ is defined using the information needed to evaluate Equation (85) together with subprograms PDPRM and VF.

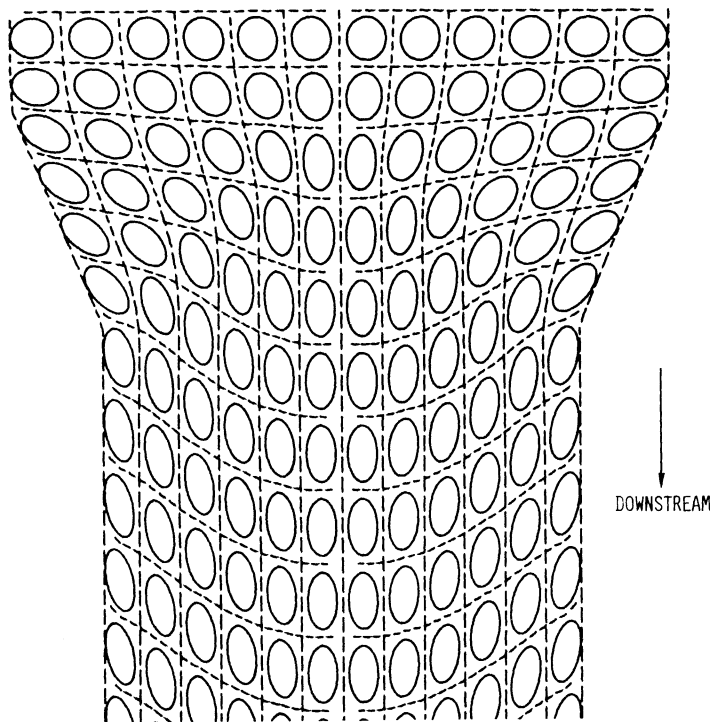
An increment of time is defined,

$$\Delta t = 1/2 \left[\left(\frac{1}{|v(I,J)|} \right) + \left(\frac{1}{|v(I,J+1)|} \right) \right] \times \left[|z(I,J+1) - z(I,J)| \right]. \quad (87)$$

Starting with time equaling zero and summing the time increments along each incrementally modeled real metal path line, every point in the array $z(I,J)$ is assigned a time $t(I,J)$. The times $t(I,J)$ are converted to integers, and the time lines $z(I,K)$ are determined in a completely analogous manner to those for the perfect fluid. To implement the computer aided plots of the time lines and path lines of the modeled real metal in the format of those kinematic variables shown in Figure 9, every fourth modeled real metal path line and every other modeled real metal time line is plotted, (See Real Metal Deformation Field Modeling Computation and Plot, Appendix D.)

The modeled real metal deformation field resulting from the computer aided plot is shown in Figure 32. This deformation field includes strain ellipses. From the time lines, velocity fields, and the path lines are determined the transformation coefficients for a given strain ellipse. That is to say that the strain ellipses are determined and plotted in a

completely analogous manner to those for the perfect fluid. This collection of strain ellipses shown in Figure 32 is an incremental representation of the strain field for the modeled real metal. The kinematic variables for the steadily flowing modeled real metal, i.e., (1) the path lines, (2) the time lines, (3) the strain ellipses, are presented in Figure 32 in the same format as the experimentally determined kinematic variables of the flowing real metal shown in Figure 9. Both the mathematically modeled and the experimentally determined deformation fields are interpreted from a Lagrangian point of view. The entire kinematic effect of a real metal steadily flowing with friction is represented by analytical manifestations of the modeled deviations, ΔP_m .



Semi-die angle: $\gamma = 22.5^\circ$
 Outlet to inlet
 dimension ratio: $H = 0.724$

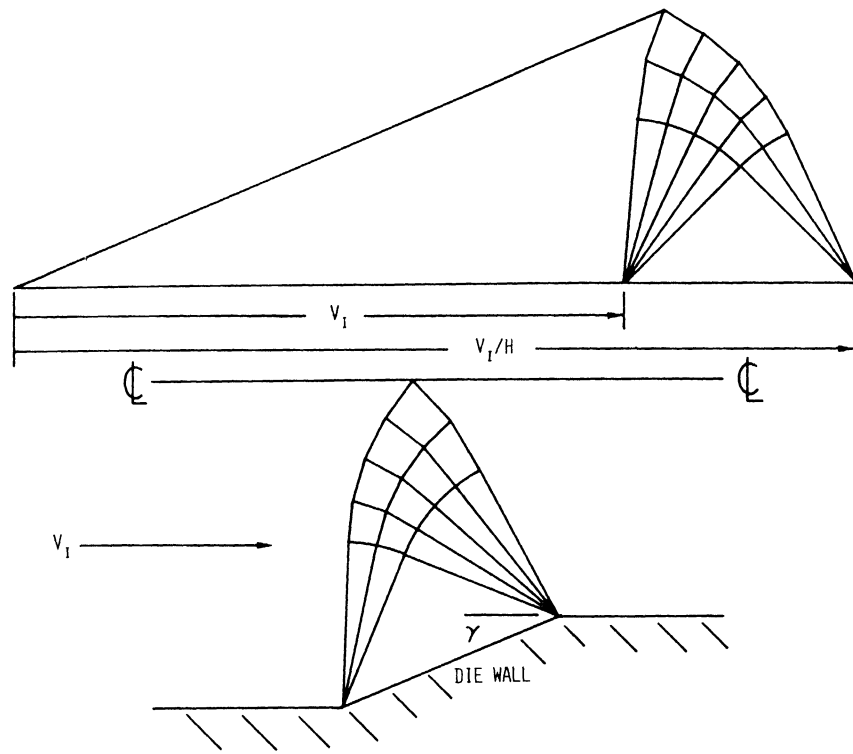
Reduction in area: $R = 0.276$
 Material: 6061-0 aluminum
 $c_1 = (4/\pi)r_2 + 1$, $c_2 = (4/\pi)r_2 + 3$

Figure 32 Modeled real metal deformation field

SLIP LINE GENERATED DEFORMATION FIELD

Slip line field theory applies to non-homogeneous plane strain deformations of a rigid-perfectly plastic isotropic solid. A perfectly plastic solid has a constant yield strength so clearly this theory does not apply to the extrusion of the work hardening 6061-0 aluminum described in this dissertation. However, the deformation field of a perfectly plastic solid extruded through the die geometry defined in Figure 12 can be compared to the real metal deformation field shown in Figure 9. This comparison is analogous to the way the real metal is compared to a perfect fluid, and the deviations of the real metal path lines with respect to the solid path lines could be modeled. The kinematical analysis of the extrusion of a perfectly plastic solid is accomplished using slip line theory. Slip line analysis for the extrusion of the perfectly plastic solid is completed using the graphical cord method.⁽⁴³⁾ The slip line field and velocity hodograph are shown in Figure 33. From the slip line field and the velocity hodograph, the path lines and time lines are constructed. The starting time line is selected to correspond to the starting time line of the perfect fluid and modeled real metal deformation fields shown in Figures 23 and 32. Path lines and time lines for the perfectly plastic solid are shown in Figure 34 where the selected path line and time line increments correspond to the experimentally selected path line and time line increments in Figure 9. The path lines for the perfectly plastic solid shown in Figure 34 are continuous but do not have continuous first derivatives due to discontinuous changes in the velocity field.

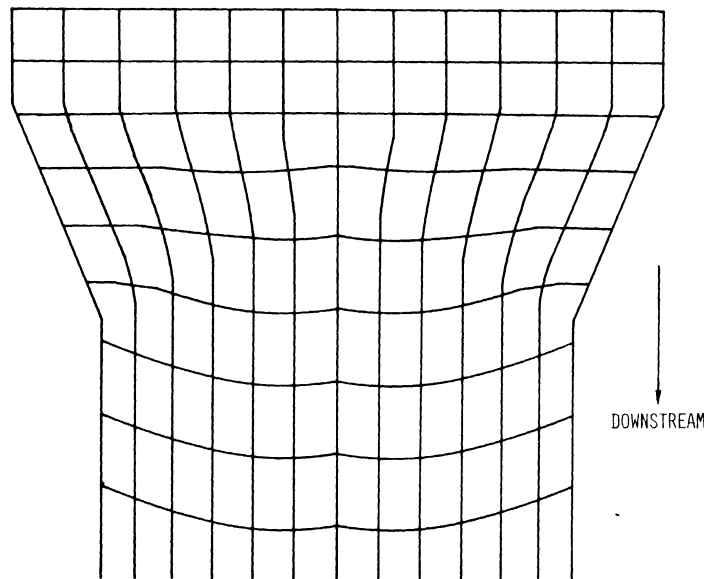
It can be proposed that the real metal path lines would be modeled by starting with the slip line field path lines and modeling the real



Semi-die angle: $\gamma = 22.5^\circ$
 Reduction in area: $R = 0.276$

Outlet to inlet
 dimension ratio: $H = 0.724$

Figure 33 Slipline field and velocity hodograph



Semi-die angle: $\gamma = 22.5^\circ$
 Reduction in area: $R = 0.276$

Outlet to inlet
 dimension ratio: $H = 0.724$

Figure 34 Deformation field of a perfectly plastic solid

metal path line deviations relative to these lines. If this technique were used to model smoothly changing real metal deformation fields as exemplified by those shown in Figures 9, 10, and 11, at each location of discontinuous change in velocity there would have to be an offsetting change in the modeled deviations so that when slip line field path lines were taken together with the modeled deviations, the results would be smoothly changing. Modeling real metal path lines relative to perfectly plastic solid path lines can be seen to introduce additional constraints when compared to the modeling technique which employs a perfect fluid.

The generalized slip line problem statement developed from kinetical considerations by Richmond⁽²⁾ can include a realistic material model. The solution to this problem would result in smoothly changing path lines, however, the detailed deformation history of the material still would be required for a work hardening material model.

Chapter IV

COMPARISON AND DISCUSSION OF MODELED DEFORMATION FIELDS AND EXPERIMENTAL RESULTS

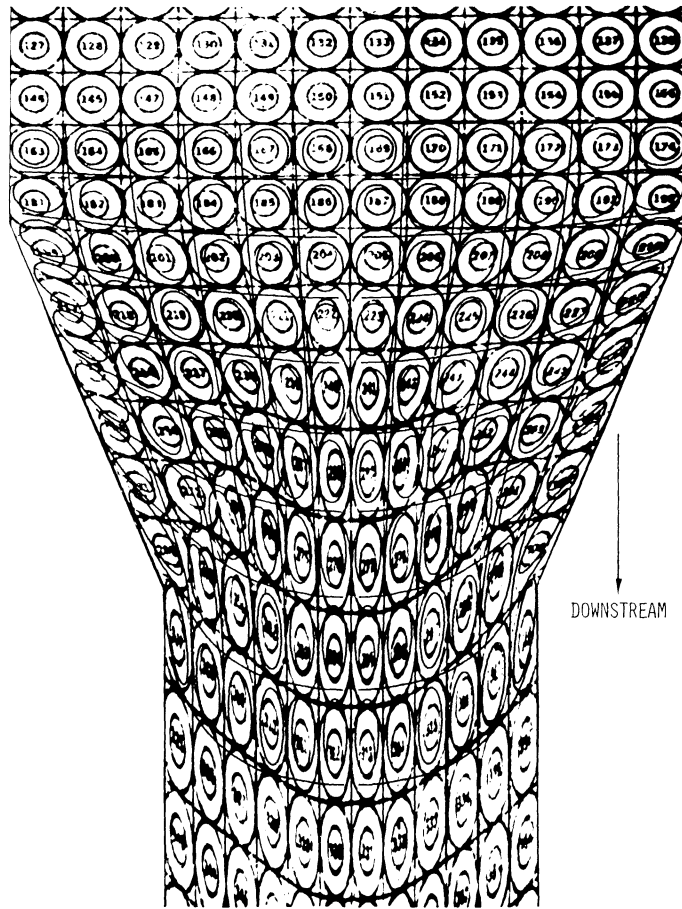
In Chapter III the real metal deformation field shown in Figure 9 is used as the basis for a mathematical model. In this chapter, this modeling method is applied to the real metal deformation fields shown in Figures 10 and 11. This method requires the comparison of the real metal path lines with the perfect fluid path lines and then the deviations between these path lines are modeled. These deviations are interpreted to be a Lagrangian measure of rotationality and from the modeled deviations, the modeled real metal path lines are defined. For this steady state extrusion process, the modeled real metal velocity field is defined in terms of the modeled real metal path lines. With the modeled velocities as a function of the modeled real metal path lines, the modeled real metal deformation field can now be determined from a Lagrangian point of view.

The results are presented by making the following superimpositions for comparative purposes. The perfect fluid deformation field, the modeled real metal deformation field, and the slip line deformation field are superimposed on the real metal deformation field.

COMPARISON OF THE PERFECT FLUID DEFORMATION FIELDS WITH THE REAL METAL DEFORMATION FIELDS

The real metal deformation fields shown in Figures 10 and 11 are compared to corresponding perfect fluid deformation fields in Figures 35 and 36 respectively. As in Figure 24, the deviations between the real metal path lines and the perfect fluid path lines are regular. On traveling downstream the real metal path line first deviates toward the

die wall and then deviates toward the center line before coming coincident with the perfect fluid path line once again.



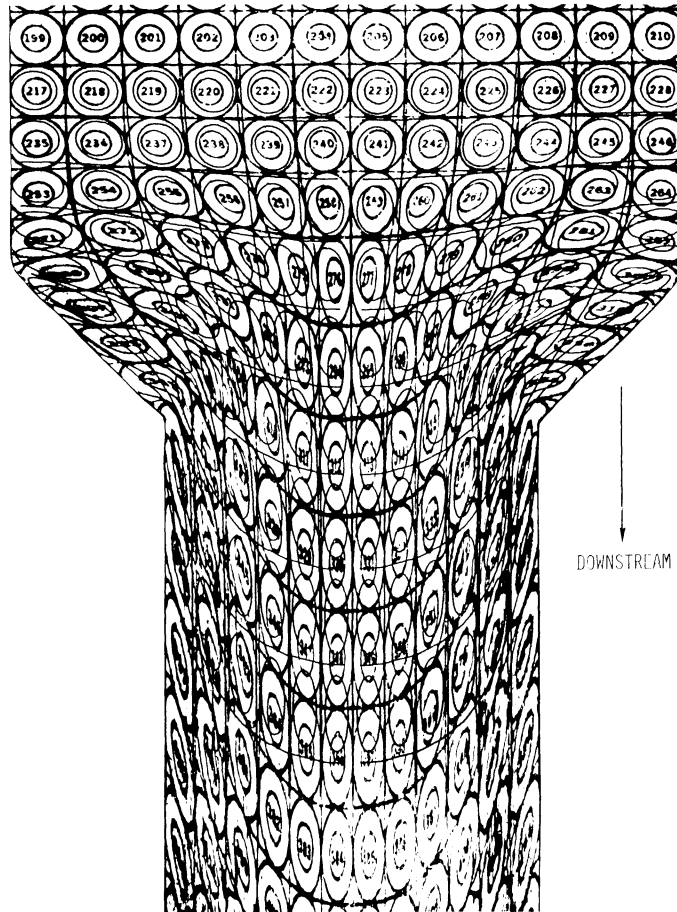
Semi-die angle: $\gamma = 22.5^\circ$
 Outlet to inlet
 dimension ratio: $H = 0.549$

Reduction in area: $R = 0.451$
 Material: 6061-0 aluminum

Figure 35 Perfect fluid deformation field superimposed on the real metal deformation field. (Note that the real metal has numbered ellipses.)

The real metal deformation fields are photographed using a copy camera with Kodak metallographic plates. The copy camera assures the orthogonality between the object photographed and the glass photographic plate; the latter assures a minimum of distortion during development. This photographic procedure is selected to minimize the distortions of

geometric relations on the photographic negative and subsequent projections.



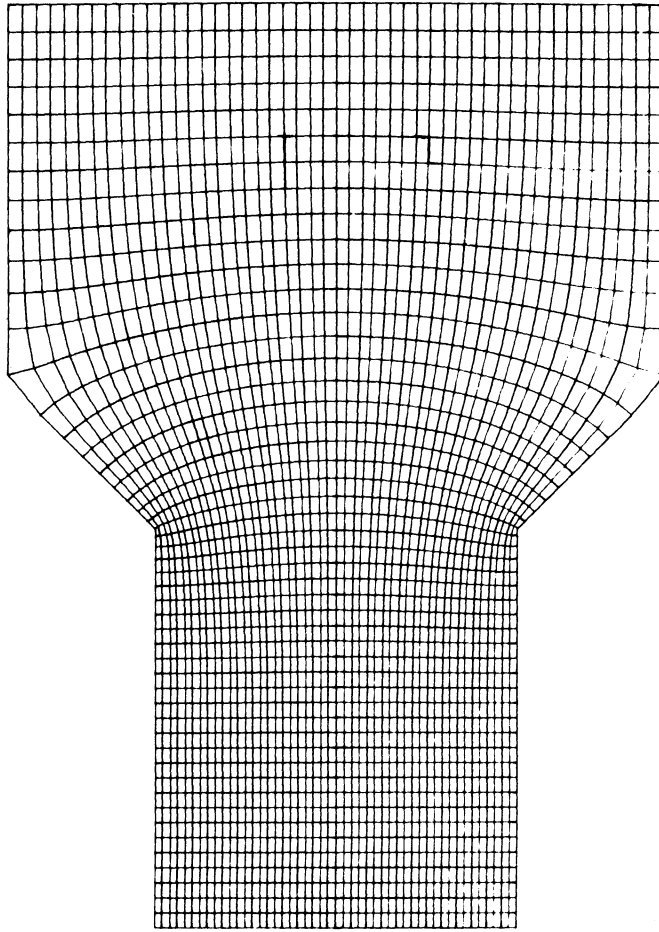
Semi-die angle: $\gamma = 45^\circ$
 Outlet to inlet
 dimension ratio: $H = 0.551$

Reduction in area: $R = 0.449$
 Material: 6061-0 aluminum

Figure 36 Perfect fluid deformation field superimposed on the real metal deformation field. (Note that the real metal has numbered ellipses.)

To determine experimentally the value of the deviations indicated in Figures 35 and 36, the image of the real metal deformation field is projected on to an orthogonal curvilinear coordinate system, (See Orthogonal Curvilinear Coordinate System Computation and Plot, Appendix D.)

The orthogonal curvilinear coordinate system shown in Figure 37 is used for analyzing the real metal deformation field shown in Figure 11. The deviations between the real metal path lines and the perfect fluid path lines are determined experimentally. By using this curvilinear coordinate system, the Lagrangian measure of rotationality ΔP , is modeled in terms of the coordinates defined in the complex potential plane p .



Semi-die angle: $\gamma = 45^\circ$
 Reduction in area: $R = 0.449$

Outlet to inlet
 dimension ratio: $H = 0.551$

Figure 37 Orthogonal curvilinear coordinate system

The experimental points for determining the model coefficients for the five representative interior path lines of the real metal deformation

field in Figure 10 are tabulated in Table VIII. The resulting coefficients A , a , α , B , b , and β from the nonlinear equation solving computer program are tabulated in Table IX, when the selected skewed symmetry terms have values,

$$c_1 = (2/\pi)r_2+1 \text{ and } c_2 = (2/\pi)r_2+2.$$

The modeled coefficients are only a function of the real metal path line r_2 . In Figure 38, cubic splines define the model coefficients for any path line.

TABLE VIII
EXPERIMENTAL POINTS FOR DETERMINING MODEL COEFFICIENTS

Die Geometry:	R = 0.451 H = 0.549 $\gamma = 22.5^\circ$					
Material:	6061-0 aluminum					
Normalized Upstream Velocity:	$V_A = 1.0$					
Lubrication:	(See Lubrication, Chapter II)					
r_2	ΔP_{\max}	$r_1(\Delta P_{\max})$	ΔP_{\min}	$r_1(\Delta P_{\min})$	$r_1(1/3\Delta P_{\max})$	$r_1(1/3\Delta P_{\min})$
0.487	0.115	-0.946	-0.0783	-4.869	0.363	-6.032
1.018	0.175	-1.340	-0.1035	-4.731	0.056	-6.112
1.549	0.200	-1.594	-0.1035	-4.582	-0.154	-6.159
2.080	0.180	-1.785	-0.0810	-4.413	-0.388	-6.201
2.611	0.109	-1.931	-0.0450	-4.263	-0.622	-6.225

TABLE IX
MODEL COEFFICIENTS

Die Geometry:	$R = 0.451$ $H = 0.549$ $\gamma = 22.5^\circ$					
Material:	6061-0 aluminum					
Normalized Upstream Velocity:	$V_A = 1.0$					
Lubrication:	(See Lubrication, Chapter II)					
Experimental Points:	(See Table VIII)					
Skewed Symmetry Coefficients:	$c_1 = (2/\pi)r_2+1, c_2 = (2/\pi)r_2+2$					
r_2	A	a	α	B	b	β
0.487	0.187	1.538	-1.543	0.114	1.629	-4.296
1.018	0.264	1.422	-2.008	0.141	1.400	-4.070
1.549	0.283	1.376	-2.281	0.134	1.294	-3.868
2.080	0.248	1.398	-2.442	0.100	1.224	-3.652
2.611	0.147	1.462	-2.541	0.054	1.184	-3.471

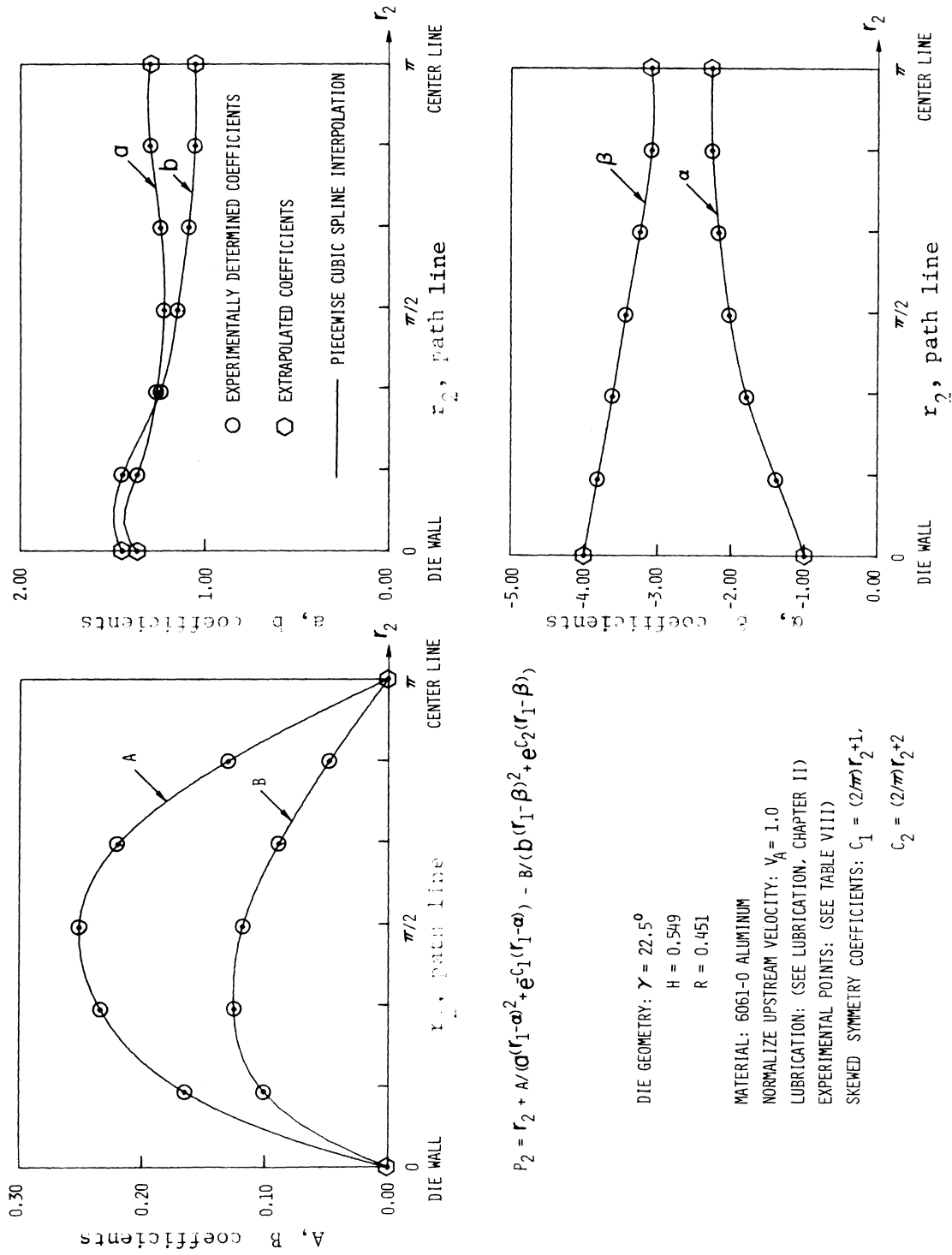


Figure 38 Model coefficients versus real metal path line, r_2

MODELED REAL METAL VELOCITY FIELD

Using Equation (76), the images of an array of modeled real metal path lines in the modeled real metal velocity plane are calculated and shown in Figure 39. The velocity at a particular position along a path

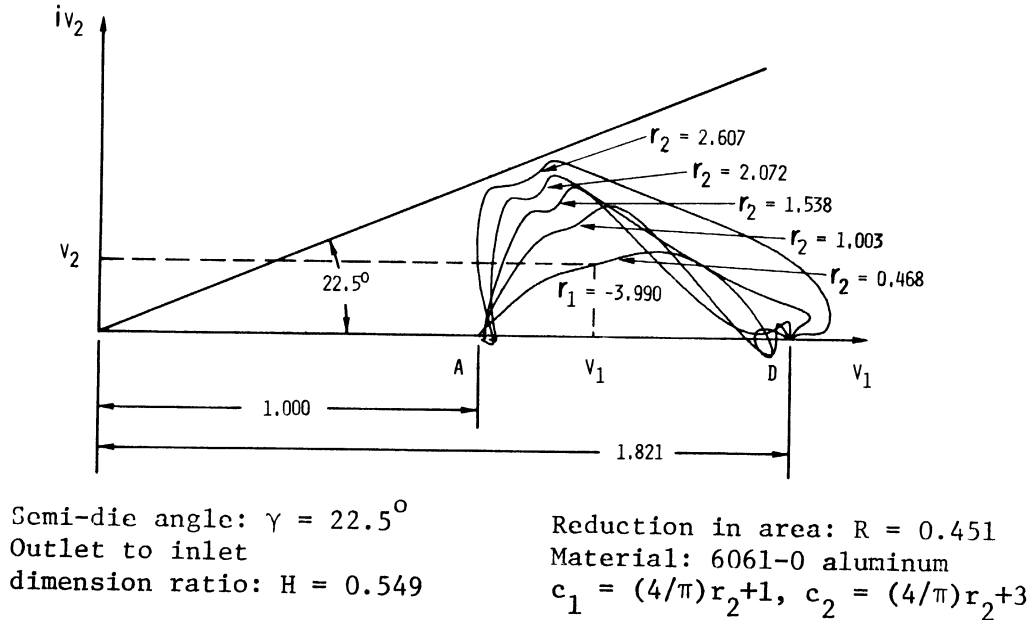
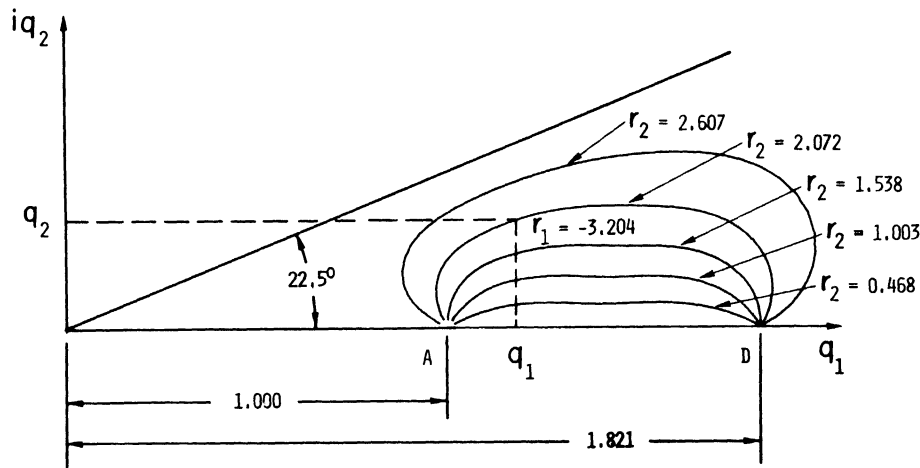


Figure 39 Images of an array of modeled real metal path lines in the modeled real metal velocity plane v

line is determined by the coordinate values of that point in this velocity plane as shown in Figure 39. The images of an array of modeled real metal path lines in the perfect fluid velocity plane are shown in Figure 40. The differences between Figures 39 and 40, and the differences between the path lines in Figure 35 are the result of the rotational character of the real metal flow field. The frictional effects and those metallic properties that contribute to this rotational character are kinematically modeled through the Lagrangian measure of rotationality, ΔP_m .



Semi-die angle: $\gamma = 22.5^\circ$
 Outlet to inlet
 dimension ratio: $H = 0.549$

Reduction in area: $R = 0.451$
 Material: 6061-0 aluminum
 $c_1 = (4/\pi)r_2 + 1$, $c_2 = (4/\pi)r_2 + 3$

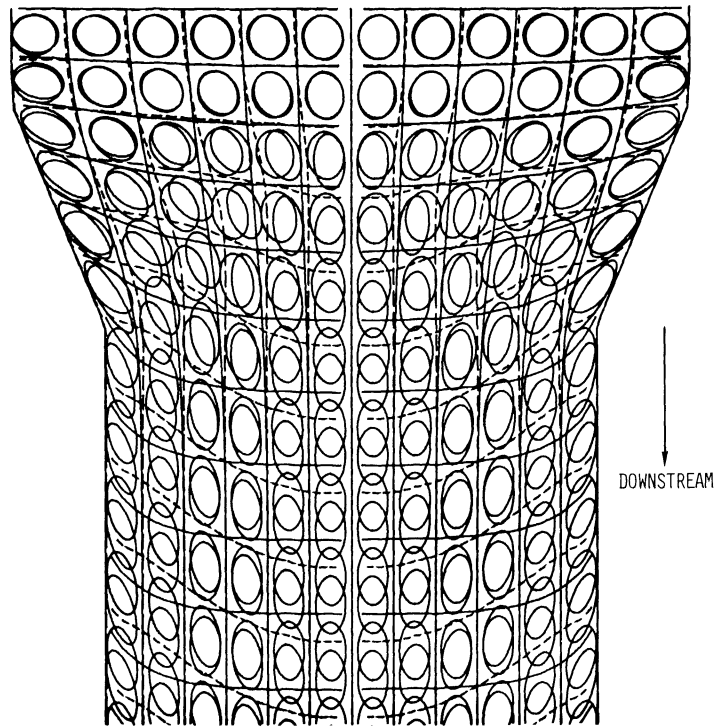
Figure 40 Image of an array of modeled real metal path lines in the perfect fluid velocity plane q .

COMPARISON OF PERFECT FLUID DEFORMATION FIELDS WITH MODELED REAL METAL DEFORMATION FIELDS

From the modeled path lines and velocities, the modeled real metal deformation field is determined for the steadily flowing 6061-0 aluminum shown in Figures 9 and 10. These modeled real metal deformation fields are compared to corresponding perfect fluid deformation fields in Figures 41 and 42.

As in Figures 24 and 35, when the perfect fluid and real metal deformation fields are compared, the deviations between the modeled real metal path lines and the perfect fluid path lines shown in Figures 41 and 42 are regular. On traveling downstream the modeled real metal path line first deviates toward the die wall and then deviates toward the center line before becoming coincident with the perfect fluid path line once again. This modeled path line behavior is similar to the real metal path line behavior. Additionally, deviations between the modeled

time lines and the perfect fluid time lines in Figures 41 and 42 are similar to the deviations between the real metal time lines and the perfect fluid time lines in Figures 24 and 35.



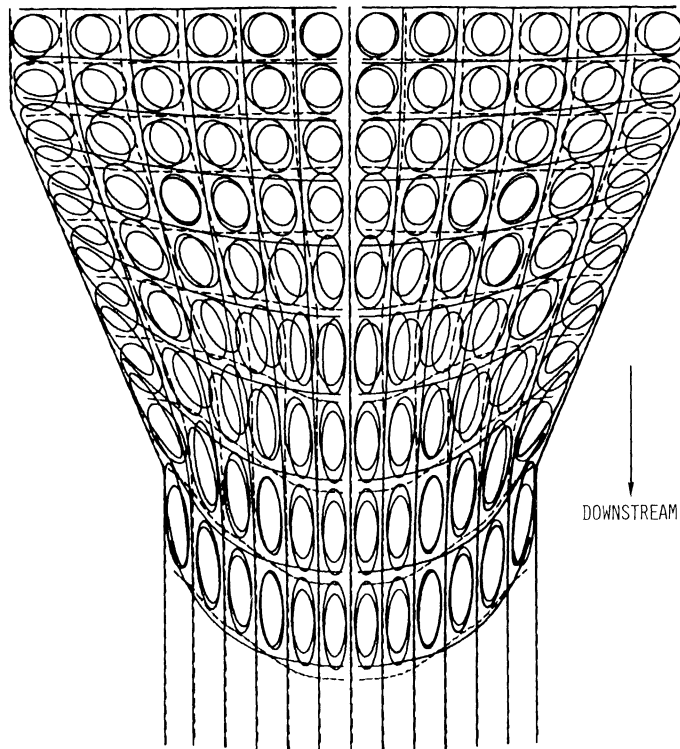
----- Modeled real metal

————— Perfect fluid

Semi-die angle: $\gamma = 22.5^\circ$
 Outlet to inlet
 dimension ratio: $H = 0.724$

Reduction in area: $R = 0.276$
 Material: 6061-0 aluminum

Figure 41 Perfect fluid deformation field superimposed on the modeled real metal deformation field



- - - - - Modeled real metal ————— Perfect fluid
 Semi-die angle: $\gamma = 22.5^\circ$ Reduction in area: $F = 0.451$
 Outlet to inlet Material: 6061-0 aluminum
 dimension ratio: $H = 0.549$

Figure 42 Perfect fluid deformation field superimposed on the modeled real metal deformation field

COMPARISON OF MODELED REAL METAL DEFORMATION FIELDS WITH REAL METAL DEFORMATION FIELDS

The modeled real metal deformation fields are determined for the steadily flowing 6061-0 aluminum shown in Figure 9 and 10. These modeled deformation fields are compared to the corresponding real metal deformation fields in Figures 43 and 44.

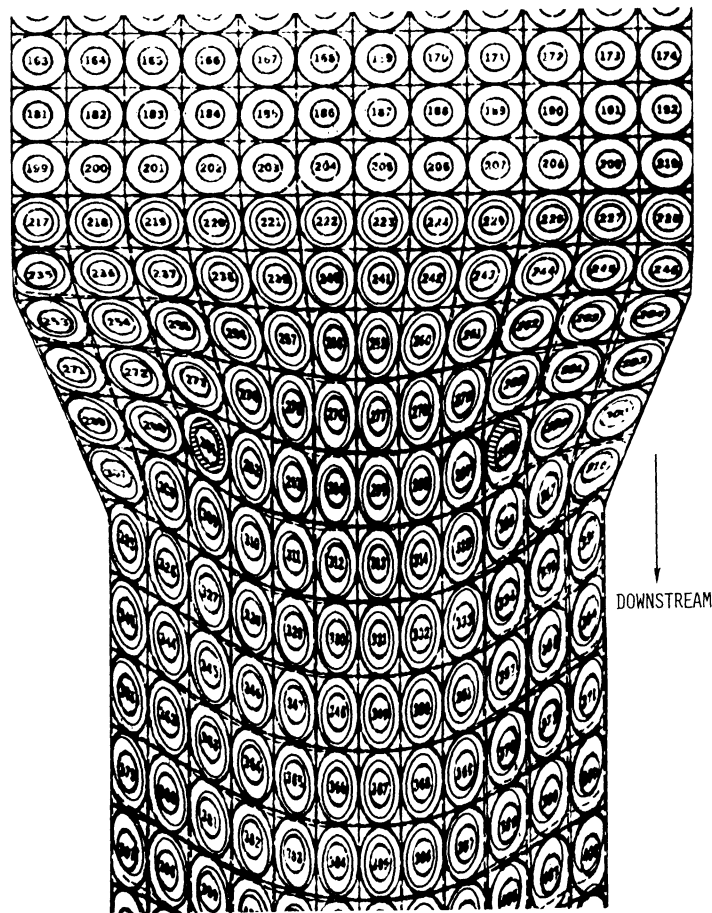
The experimental extrusion is conceived to be symmetric and two dimensional. Actually, the billets become somewhat thicker as indicated

by the foreshortening ratios in Table V. In Figure 43 the area between two sets of concentric ellipses is shaded. The smallest ellipse in each set is the experimentally deformed strain ellipses while the next larger is the modeled strain ellipse. The two modeled strain ellipses are constructed symmetrically about the center line. From the differences between the two shaded areas, the experimental extrusion is seen to be asymmetrical. Upon inspection, the extrusion dies were found to be slightly asymmetrical.

The modeled real metal deformation fields shown in Figures 43 and 44 are in error. Besides foreshortening, the errors are of two types:

1. errors in displacements from the original time line
2. errors in the relative displacements or strains.

Errors in displacements are differences in location between the modeled strain ellipses and the corresponding experimental strain ellipses. Errors in relative displacements are differences in shape and orientation between the modeled strain ellipse and the corresponding experimental strain ellipse irrespective of errors in location. The errors in displacements between symmetric modeled strain ellipses and the experimental strain in Figure 43 graphically point out the asymmetrical character of the real metal deformation field. To the author, this asymmetrical character is not obvious on first inspection of the flow field in Figure 9. Somewhat finer distinctions with respect to real metal flow fields appear to be possible when the real metal flow field is compared to a modeled flow.



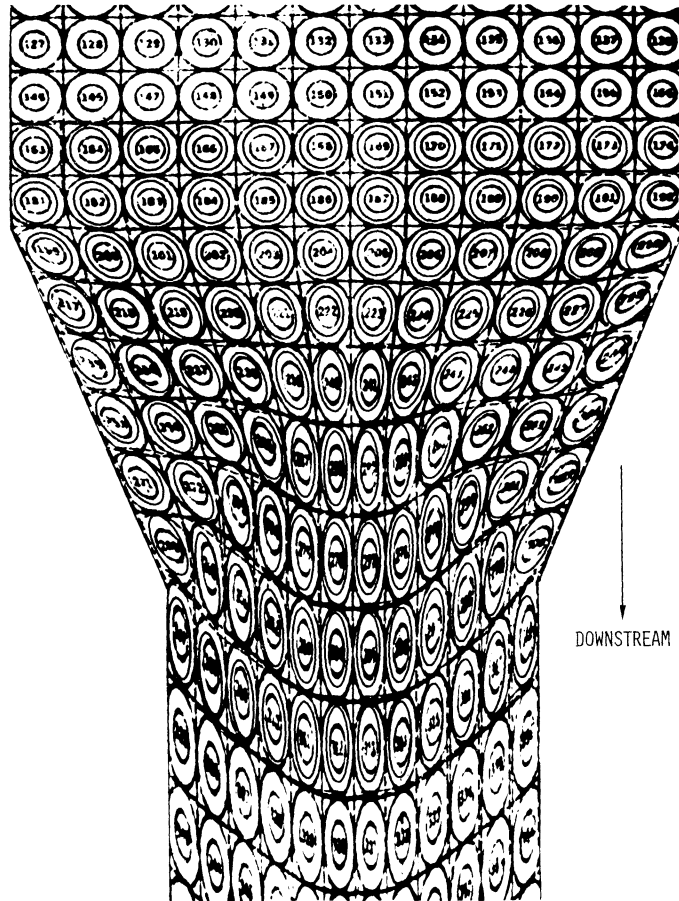
----- Modeled real metal

Semi-die angle: $\gamma = 22.5^\circ$
 Outlet to inlet
 dimension ratio: $H = 0.724$

Reduction in area: $R = 0.276$
 Material: 6061-0 aluminum

Figure 43 Modeled real metal deformation field superimposed on the real metal deformation field. (Note that real metal has numbered ellipses.)

The selected differential radius δ of the neighborhood of points for which the strain is to be defined must be small with respect to the characteristic radii of curvature of both the time lines and path lines, if an ellipse is to accurately indicate the strain state. Additionally,



----- Modeled real metal

Semi-die angle: $\gamma = 22.5^\circ$

Reduction in area: $R = 0.451$

Outlet to inlet
dimension ratio: $H = 0.549$

Material: 6061-0 aluminum

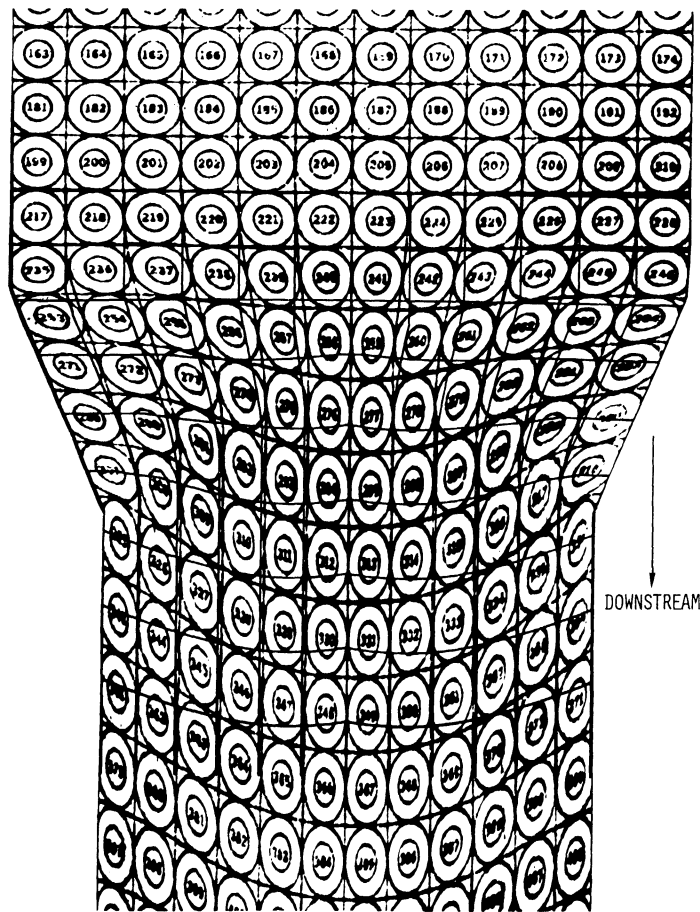
Figure 44 Modeled real metal deformation field superimposed on the real metal deformation field. (Note that real metal has numbered ellipses.)

the differential radius δ , must be small compared to these characteristic radii of curvature for any displacement of the neighborhood of points if an ellipse is to accurately represent the changing strain for these displacements. The corners in the extrusion die walls which correspond to points B and C in Figure 13 are singularities. The radius of curvature for the path line at these corner points is zero. For path lines that pass close to these corner points the strain ellipses that result from neighborhoods defined by increasingly smaller differential

radii more accurately represent the strains in these areas. This effect is seen in the areas adjacent to the die wall corners in Figures 9, 10, and 11.

COMPARISON OF SLIP LINE DEFORMATION FIELDS WITH REAL METAL DEFORMATION FIELDS

The slip line modeled deformation fields, as determined for a perfectly plastic solid, are compared to the corresponding real metal deformation fields in Figures 45, 46, and 47.

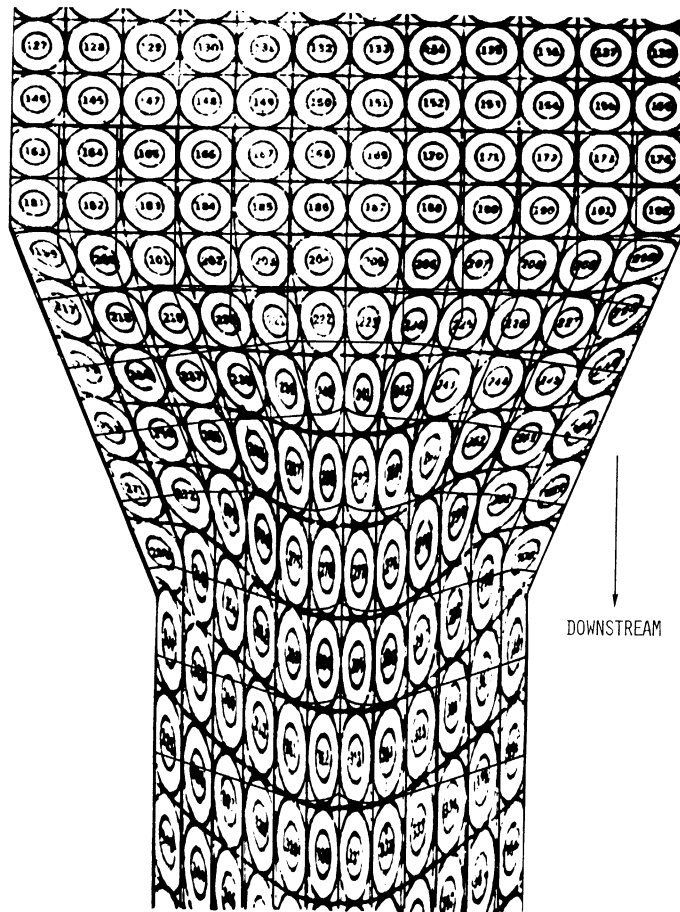


Semi-die angle: $\gamma = 22.5^\circ$
 Outlet to inlet
 dimension ratio: $H = 0.724$

Reduction in area: $R = 0.276$
 Material: 6061-0 aluminum

Figure 45 Slip line deformation field superimposed on the real metal deformation field

The flowing perfect fluid is described by Laplace's (an elliptic) partial differential equation, whereas the flowing perfectly plastic solid is described by a hyperbolic partial differential equation. The comparison of the real metal deformation field with that of both the perfect fluid and perfectly plastic solid indicates that the real metal flow field is described by neither an elliptic nor a hyperbolic partial differential equation. The hyperbolic equation of a flowing perfectly

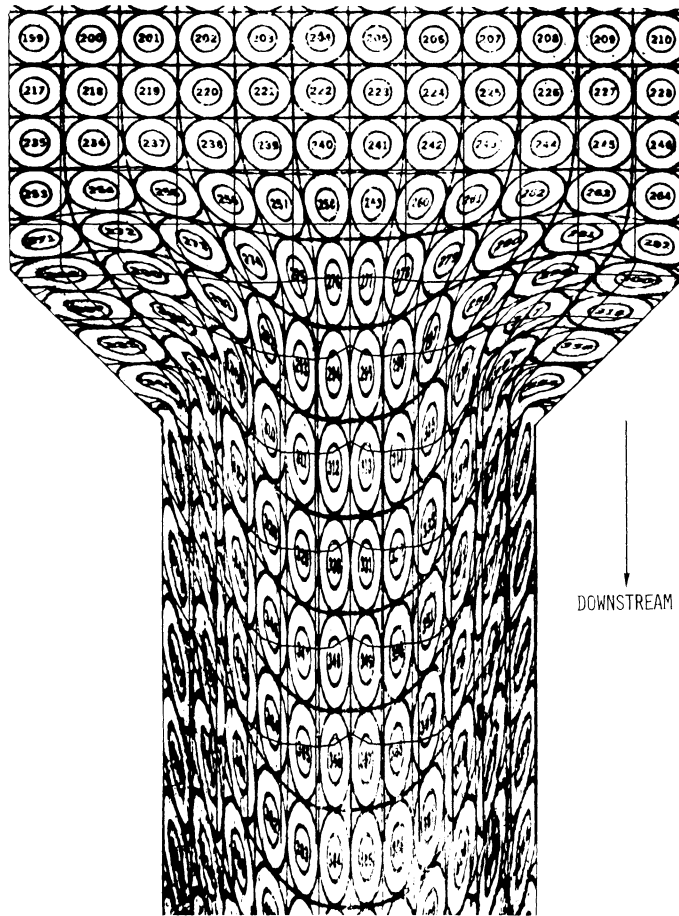


Semi-die angle: $\gamma = 22.5^\circ$
 Outlet to inlet
 dimension ratio: $H = 0.549$

Reduction in area: $R = 0.451$
 Material: 6061-0 aluminum

Figure 46 Slip line deformation field superimposed on the real metal deformation field

plastic solid confines the deformations to within the slip line field, whereas the flowing perfect fluid as described by an elliptic equation is disturbed in the limit both up and down stream from the tapered die section. The real metal deformation zone can be seen to be greater than that described for a perfect plastic solid but less than that of a perfect fluid.



Semi-die angle: $\gamma = 45^\circ$
 Outlet to inlet
 dimension ratio: $H = 0.551$

Reduction in area: $R = 0.449$
 Material: 6060-0 aluminum

Figure 47 Slip line deformation field superimposed on the real metal deformation field

PERTURBATIONS OF THE DEVELOPED MODEL FOR THE REAL METAL DEFORMATION FIELD

The model of the real metal deformation field developed in Chapter III is created in an explicit manner; however, there are equally valid alternatives to that modeling method. This section deals with two perturbations or small changes to the modeling method of Chapter III. The first perturbed modeling method is based on alternate ways of extrapolating the model coefficients, other than A and B, to the die wall. (See page 72, Chapter III.) The second perturbed model is based on alternate functional relations for the skewed symmetry coefficients c_1 and c_2 .

The five interior values of the model coefficients shown in Figure 48 are determined experimentally and have the same values as those coefficients shown in Figure 38. The values of the model coefficients in Figure 48 are extrapolated in the same manner as those model coefficients shown in Figure 38 except for the die wall values of α and β . In modification 1, the die wall values of α and β in Figure 48 are defined to be equal to the first experimentally determined value adjacent to the die wall. Interpolation by piece wise cubic splines completes the definition of the model coefficients shown in Figure 48 so that any real metal path line can be modeled.

In Figure 49, modification 1 of the modeled real metal deformation field is superimposed on the modeled real metal deformation field developed in Chapter III. The effect of the modified model coefficients is most readily seen in the deviations of the modeled time lines from the experimental time lines on traveling down stream through the die adjacent to the die walls.

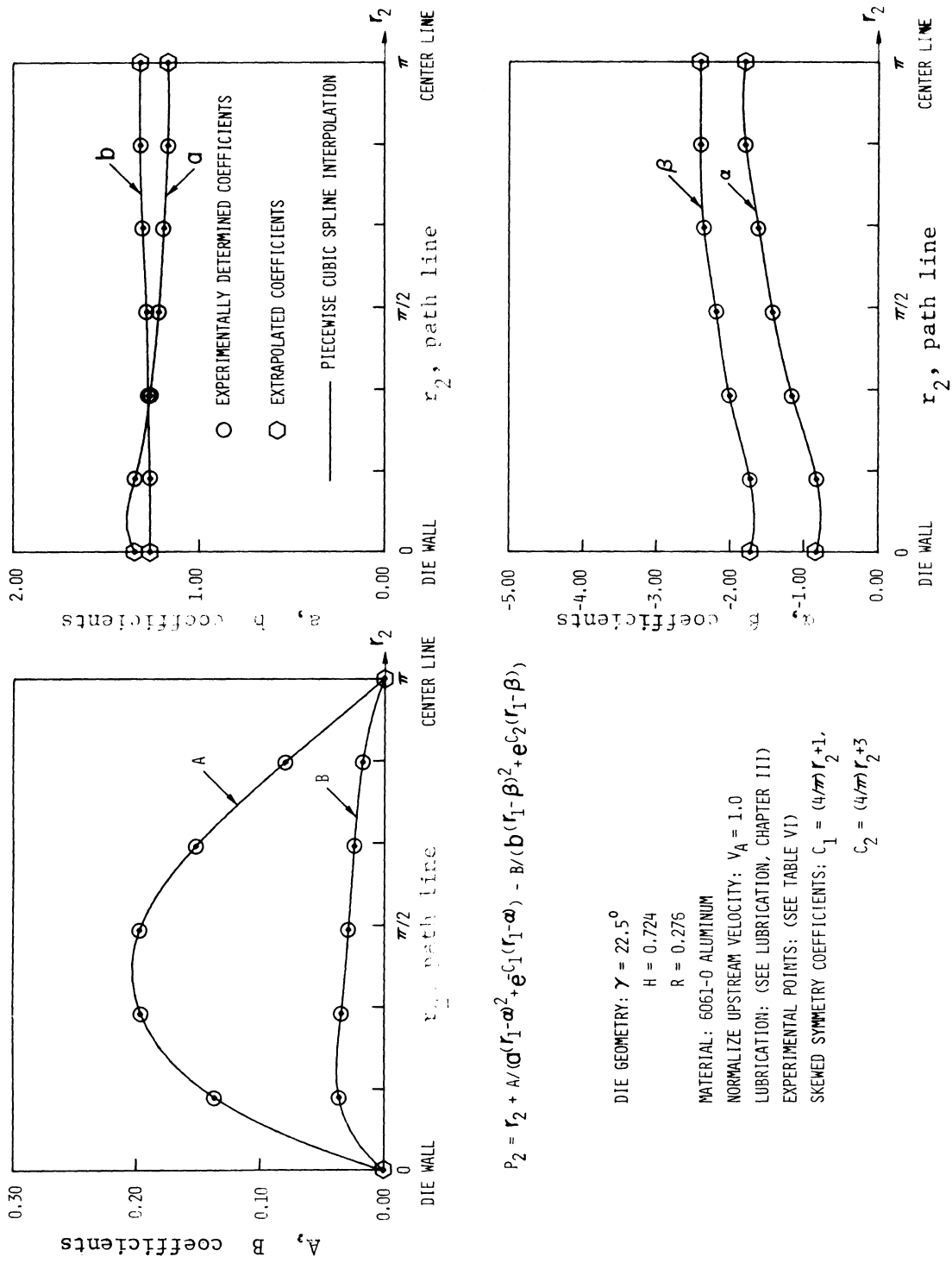
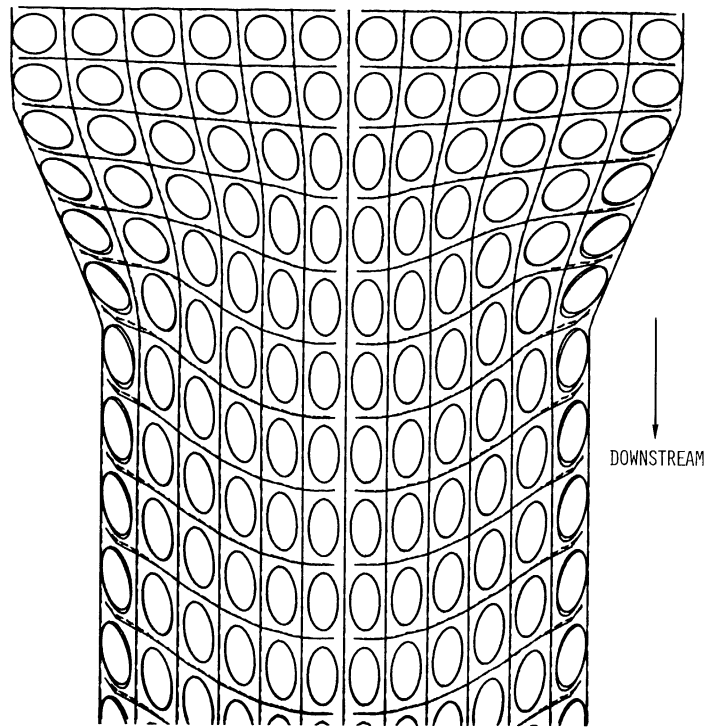


Figure 48 Modification 1, model coefficients versus real metal path line, r_2



——— Modification 1. ---- Model developed in Chapter III
 Semi-die angle: $\gamma = 22.5^\circ$ Reduction in area: $R = 0.276$
 Outlet to inlet Material: 6061-0 aluminum
 dimension ratio: $H = 0.724$

Figure 49 Modeled deformation field based on Modification 1 superimposed on the modeled deformation field developed in Chapter III

Modification 2 is created using new functions for the skewed symmetry coefficients. Table VIII, new model coefficients are calculated when

$$c_1 = (6/\pi)r_2+1 \text{ and } c_2 = (6/\pi)r_2+5.$$

The experimentally determined model coefficients are plotted in Figure 50. This model coefficient set is extrapolated in Figure 50 by the procedure of Chapter III. Interpolation by piecewise cubic splines completes the definition of the model coefficients.

The modeled real metal deformation field based on these new coefficients is superimposed in Figure 51 on the modeled real metal deformation field developed in Chapter III. The effect of the new coefficients

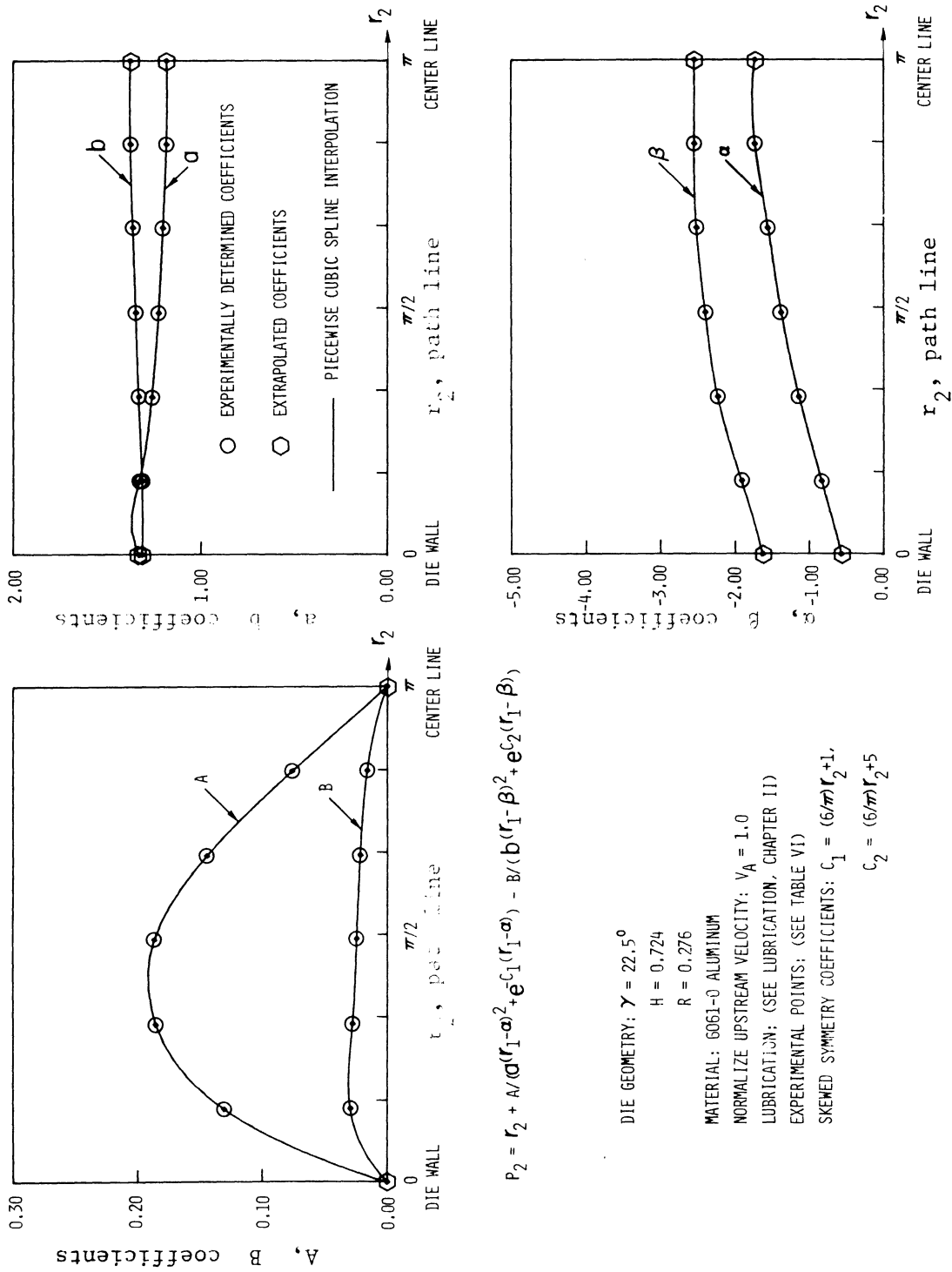


Figure 50 Modification 2, model coefficients versus real metal path line, r_2

is most readily seen in the deviation between the modeled time lines. These deviations manifest themselves at a greater distance from the die wall than those associated with modification 1.

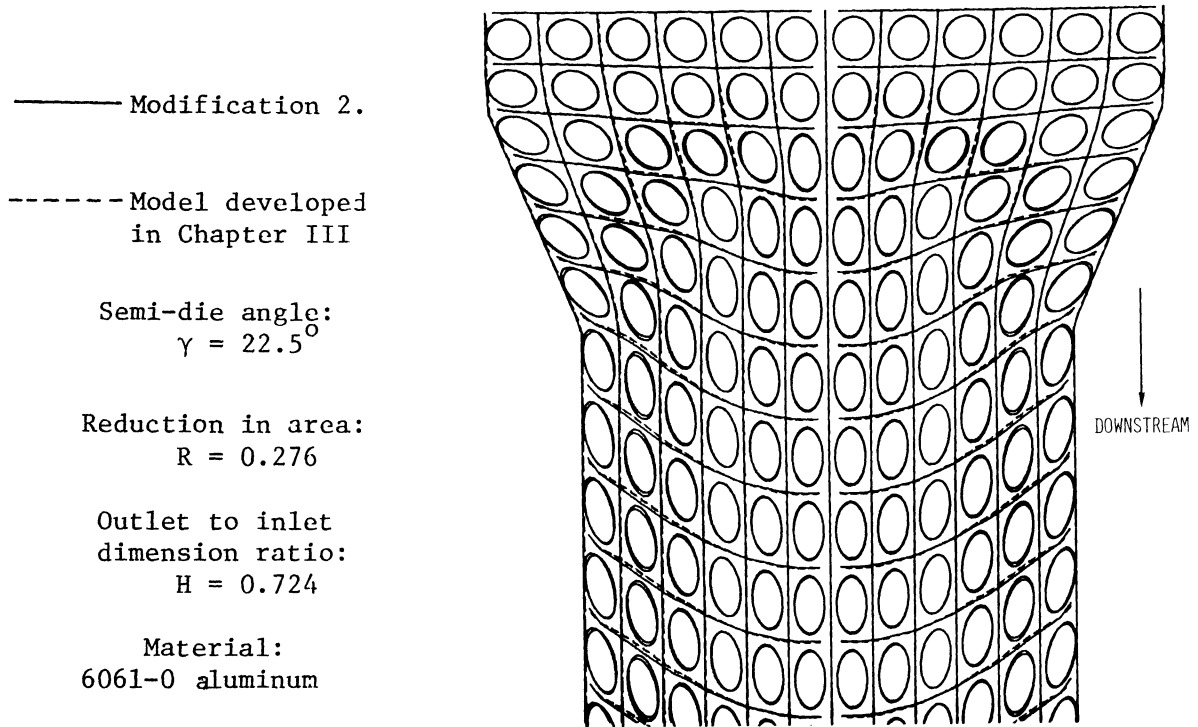


Figure 51 Modeled deformation field based on Modification 2 superimposed on the modeled deformation field developed in Chapter III.

The two perturbations discussed in this section together with combinations of these changes, are available to the kinematic modeler of real metal deformation fields. The model used in Chapter III, compared to the modifications in Figures 49 and 51, is judged to be more effective. The perturbed techniques are presented to indicate ways of creating the alternate choices a kinematic modeler requires to assay goodness of fit.

POTENTIAL FLOW AND PLANE-STRAIN EXTRUSION

Potential flow theory has been applied to plane-strain extrusion by Shabaik, Kobayashi, and Thomsen⁽⁴⁴⁾ and to axisymmetric extrusion by Shabaik and Thomsen⁽⁴⁵⁾. In each case the flow field developed from the potential solution is compared to an actual flow as visualized by using a split billet technique (grids are used but no circles). The similarities and differences were noted. That the potentially derived flow field is irrotation in character as compared to the rotational character of the actual flow field was emphasized by Richmond and Devenpeck in their discussion of the Shabaik, Kobayashi, and Thomsen paper. The technique presented in this dissertation starts with the differences between the flow fields and models these differences in terms of a curvilinear coordinate system defined by the potential solution. The resulting modeled flow is rotational in character.

CONCLUSIONS

1. The principal strains and directions are readily obtained experimental data and modeled computer output.
2. The modeled real metal deformation field provides a base for determination of experimentally related variations.
3. The perturbation techniques utilized in this study effectively enhance the goodness of fit.
4. The modeled measure of rotationality, ΔP_m , minimizes error magnification in determination of rotationality.
5. The Lagrangian measure of rotationality, ΔP_m , is influenced by frictional effects and metallic properties.
6. The real metal deformation zone is greater than that for a perfectly plastic solid, but less than that of a perfect fluid.

7. The Lagrangian kinematic model is applicable to continuously deformable materials without requiring a material model.

FUTURE APPLICATIONS

One of the strongest attributes of the techniques presented in this dissertation is the ability to amass large amounts of numerical information accompanying the kinematical relationships. Logically this leads to the employment of this method for obtaining a better understanding of the effects of strain history on product properties, perhaps resulting in improved material models.

In like manner property distributions within extrusions can be determined which reasonably could lead to directly applicable correlations between strain histories and deformation related properties.

Lubrication influence on extrusion and other processes is an area to be studied in hopes of putting numerical values on lubricants and frictional effects. The techniques presented are directly applicable.

Further, the work of this thesis should be extended to other die geometries as well as axisymmetrical three-dimensional cases for extrusions, indirect extrusions and drawing.

APPENDIX A

SELECTED PROPERTIES OF 6061-0 ALUMINUM

The 6061-0 aluminum is received in the T6511 temper (extruded and stress-relieved stretched). The original bar stock of dimensions 1.0 inch by 2.5 inches in 12 foot lengths is completely annealed to bring it to the "0" temper condition. The measured properties are compared to typical properties as tabulated in the ASM Metals Handbook, Properties and Selection, Volume 1 ⁽¹⁵⁾ in Table X.

TABLE X
SELECTED MECHANICAL PROPERTIES
6061-0 ALUMINUM

	MEASURED	TYPICAL
Yield Strength	6,650 psi [*]	8,000 psi
Tensile Strength	18,100 psi	18,000 psi
Elongation	31.2%	30%
Reduction in Area	74.4%	-----

* See TABLE XI

HARDNESS

Measured Hardness:

$63R_H^*$ average of 5 readings, range 1 R_H .

10 R_E average of 4 readings, range 2 R_E .

Typical Hardness:

60 - 75 R_H

* Rockwell Hardness

YIELD STRENGTH VERSUS PERCENT COLD WORK

The 6061-0 aluminum is work hardenable. From information determined during a tensile test, the yield strength and percent cold work are tabulated in Table XI. The yield strength of 6061-0 aluminum doubles within 5 percent cold work. The cold work is defined in terms of the changing cross sectional area.

TABLE XI

YIELD STRENGTH VERSUS PERCENT COLD WORK

Yield Strength	Percent Cold Work
6780 psi	0.94
9180 psi	1.72
12600 psi	3.26
13850 psi	4.42

TENSILE BEHAVIOR

The plastic strain data is determined on the run, i.e., the diameter data is taken while the test load is being applied. The modified stress state due to the hour glass shape of the tensile specimen after necking is not included as a correction. (See Figure 52.)

MODELED TENSILE BEHAVIOR

The tensile behavior of this metal is modeled,

$$\sigma = 29,500 (\epsilon)^{.255} \text{ psi}, \quad (88)$$

where σ is the true stress and ϵ is the true plastic strain.

ANISOTROPIC BEHAVIOR

The aluminum behaves in an anisotropic manner during the tensile test. The originally round tensile specimen cross section becomes elliptical by the time of fracture. The minimum and maximum diameters at fracture are

$$D_{\min} = 0.255 \text{ inches,}$$

and

$$D_{\max} = 0.310 \text{ inches.}$$

An isotropic material would have had a circular cross section. The information used to create the true stress versus true strain graph in Figure 52 results from measurement taken on the diameter.

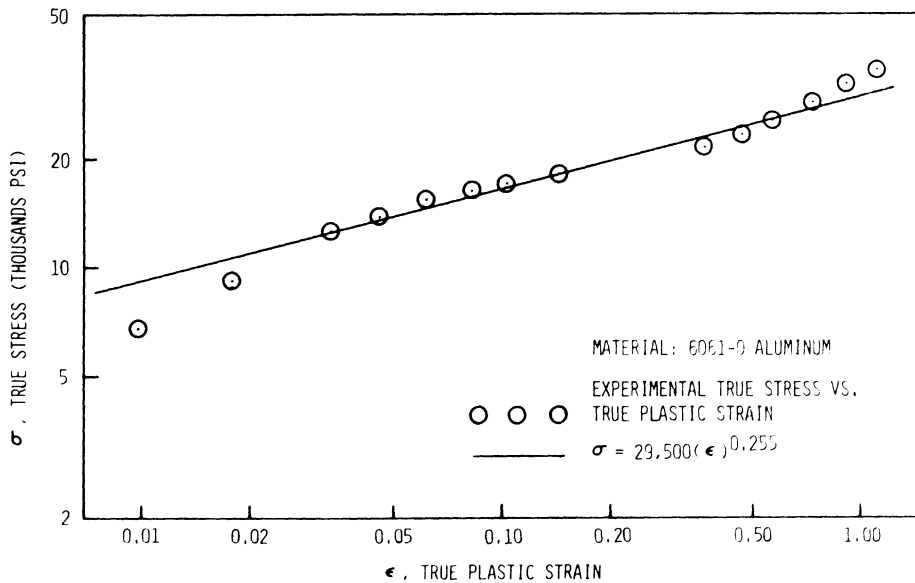


Figure 52 True stress versus true plastic strain

APPENDIX B

RAM LOADS AND VELOCITIES DURING THE
DIRECT COLD TWO DIMENSIONAL EXTRUSION PROCESS

The ram loads and velocities during the direct cold two dimensional extrusion of 6061-0 aluminum are summarized in Figure 53.

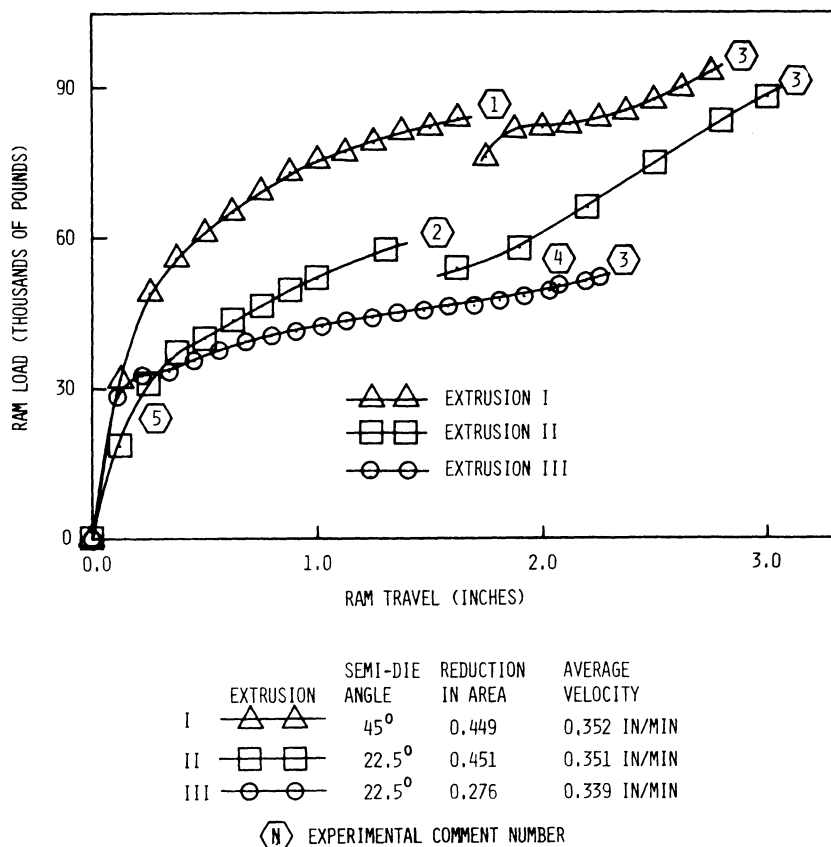


Figure 53 Ram loads and velocities during the direct cold two dimensional extrusion of 6061-0 aluminum

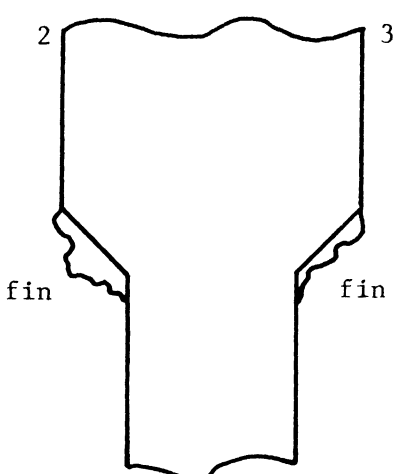
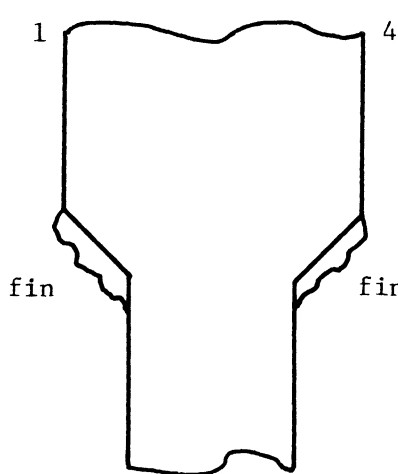
Experimental comments:

1. In extrusion I at this point, the extrusion machine was disassembled and the split billet relubricated as shown in Figure 7 before resumption of the extrusion process.

2. In extrusion II at this point, the extrusion process was halted overnight and resumed the next morning.
3. The increasing rate of loading with ram travel was discovered to be a manifestation of the formation of fins. The fins are formed when the billet is extruded between the parting surfaces needed for the disassembly of the extrusion machine, (See Table XII.).
4. In extrusion II at this point, the maximum piston stroke was exceeded. A spacer block was added and the extrusion completed.
5. The billet in extrusion II was 1.4% thinner than the billets used in the other two experimental extrusions. The more gradual initial increase in load with ram travel in this region is thought to be associated with the initial deformation of the billet within the container walls.
6. Extrusions I and II proceed in steps shown in Figure 53. In extrusion I, the standard deviation among the step velocities is 0.0204 inches per minute. In extrusion II, the standard deviation among the step velocities is 0.0733 inches per minute. Extrusion III was extruded continuously with load readings taken at equal time intervals. Within the accuracy established in extrusions I and II, the ram travel distance at each time interval is calculated from the average velocity in extrusion III.
7. The numbers next to the billet shown in Table XII were scribed onto the billets before extrusion. These numbers correspond to numbers on the extrusion machine. The parts of the extrusion machine were numbered to assure that the machine is assembled in the same way each time.

8. The fins were removed before the photographs in Figures 9, 10, and 11 were taken.

TABLE XII
FIN THICKNESSES

Position					
					
Fin Thickness		Semi-Die Angle	Reduction [*] in Area	Fin Thickness	
2	3			1	4
0.007 ^{**}	0.011	45°	0.449	0.005	0.013
n ^{***}	0.009	22.5°	0.451	n	0.009
n	n	22.5°	0.276	n	n

* experimental, assuming thickness remains constant

** inches

*** negligible

APPENDIX C

THE SCHWARZ CHRISTOFFEL TRANSFORMATION FOR THE GENERAL QUADRILATERAL WITH TWO VERTICES EXTENDED, OF THE EXTENDED VERTICES, ONE CONTAINS A SOURCE AND THE OTHER CONTAINS AN EQUAL SINK.

COMPLEX VARIABLE NOTATION THAT IS PECULAR TO THIS WORK

The complex variable will be denoted by lower case Roman letters,

$$p, q, \dots, x, y, z,$$

where the real part and the imaginary part will be denoted by subscripts 1 and 2 respectively, for example,

$$w = w(w_1, w_2),$$

$$w = w_1 + iw_2,$$

or

$$w = r_w e^{i\theta_w},$$

where

$$r_w = (w_1^2 + w_2^2)^{1/2}$$

and

$$\theta_w = \tan^{-1}(w_2/w_1).$$

A specific complex point will be denoted by a capital Roman letter,

$$A, B, \dots, L, M, N,$$

where the real part and the imaginary part will be denoted by subscripts 1 and 2 respectively, for example,

$$A = A_1 + iA_2$$

or

$$A = A(A_1, A_2).$$

If we have one or several conformal transformations, the image of a specific point with respect to a variable can have the form when required, for example,

$$A_z = A_{1z} + iA_{2z},$$

or

$$A_z = A(A_{1z}, A_{2z}).$$

which refers to the image of the point A in the z plane.

The reasons for the subscripted complex notation are to economize the symbolization and to facilitate the use of two dimensional tensor or vector calculus when these techniques would seem useful.

THE SCHWARZ CHRISTOFFEL TRANSFORMATION

The general quadrilateral with the vertices extended is shown in Figure 54. The Schwarz Christoffel transformation,

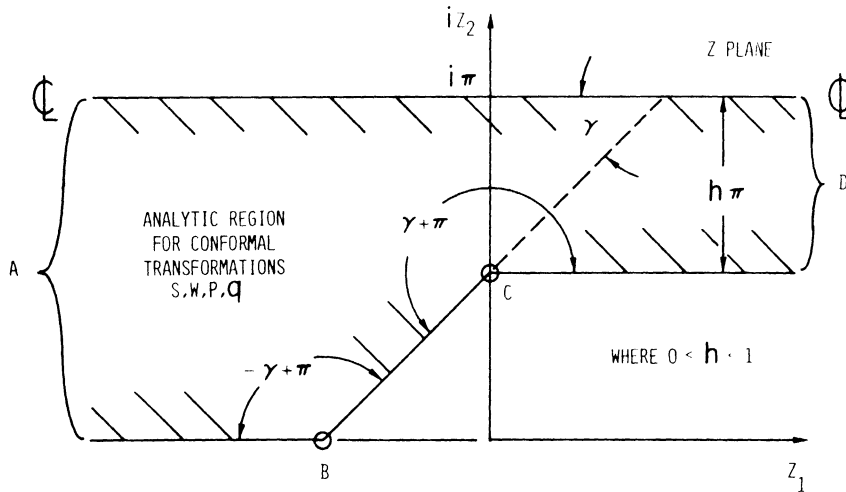


Figure 54 Physical plane z

$$\frac{dz}{dw} = R_t \prod_{k=1}^n (w-a_k)^{\left(\frac{\alpha_k}{\pi} - 1\right)}$$

in general maps the interior of a polygon onto the upper half plane, the w plane in this case. The α_k term represents the interior angle of the

of the K^{th} vertice, while the a_k term represents the image of the K^{th} vertice in the w plane.

The transformation is completed by integration,

$$z = R_t \int \prod_{k=1}^n (w-a_k)^{\left(\frac{\alpha_k}{\pi} - 1\right)} dw + T_t \quad (89)$$

where the constant R_t can be used to control the relative size and orientation of the polygon in the z plane, and the constant T_t can be used to translate the polygon in the z plane.

In general three vertices can be mapped arbitrarily whereas the images of the remaining vertices must be uniquely determined.

For the quadrilateral in Figure 54 let,

$$\begin{aligned} \alpha_1 = \alpha_A = 0, \quad \alpha_2 = \alpha_B = -\gamma + \pi, \\ \alpha_3 = \alpha_C = \gamma + \pi, \quad \alpha_4 = \alpha_D = 0, \end{aligned}$$

also let the images of the four vertices in the w plane have the following values,

$$\begin{aligned} a_1 = A_w = 0, \quad a_2 = B_w = b \text{ where } 0 < b < 1, \\ a_3 = C_w = 1, \quad a_4 = D_w = \text{the extended point.} \end{aligned}$$

The Schwarz Christoffel transformation for the quadrilateral in Figure 54,

$$\frac{dz}{dw} = \frac{R_t}{w} \left(\frac{w-1}{w-b} \right)^{\gamma/\pi} \quad (90)$$

will be rationalized by the following procedure. Let

$$m = \gamma/\pi, \text{ where } 0 < m \leq 1.$$

When m is an irrational number, the rational fraction f/g will be used to approximate m as closely as desired. Before completing the rationalization of this derivative the constants R_t and b will be determined.

Point A will be considered a source and point D will be considered an equal sink. The complex potential function P for the flow in the w half plane, Figure 55 is

$$P = \frac{Q}{\pi} \text{Log } w,$$

where Log w is the principal value of log w.

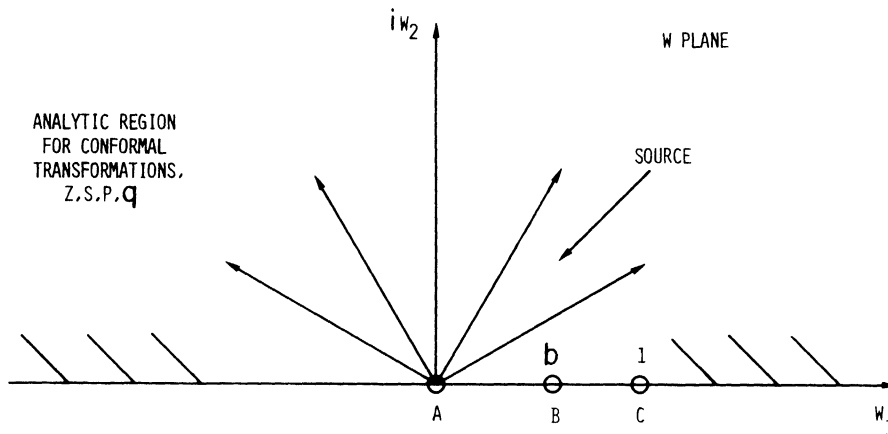


Figure 55 The Schwarz Christoffel upper half plane. Point D is extended.

Let the real constant V_A denote the velocity of the flow in the limit far from the offset to the left in the physical plane, Figure 54.

Let q be the velocity where,

$$q = \text{complex conjugate } \frac{dp}{dz} = \overline{\frac{dp}{dz}}$$

and

$$\lim_{\text{Re}(z) \rightarrow -\infty} q = V_A.$$

Therefore the strength of the source on the left and of the sink on the right in the physical plane, is then

$$Q = \pi V_A,$$

and then

$$p = V_A \text{Log } w.$$

Figure 56 and 57 show the p plane and the q plane respectively.

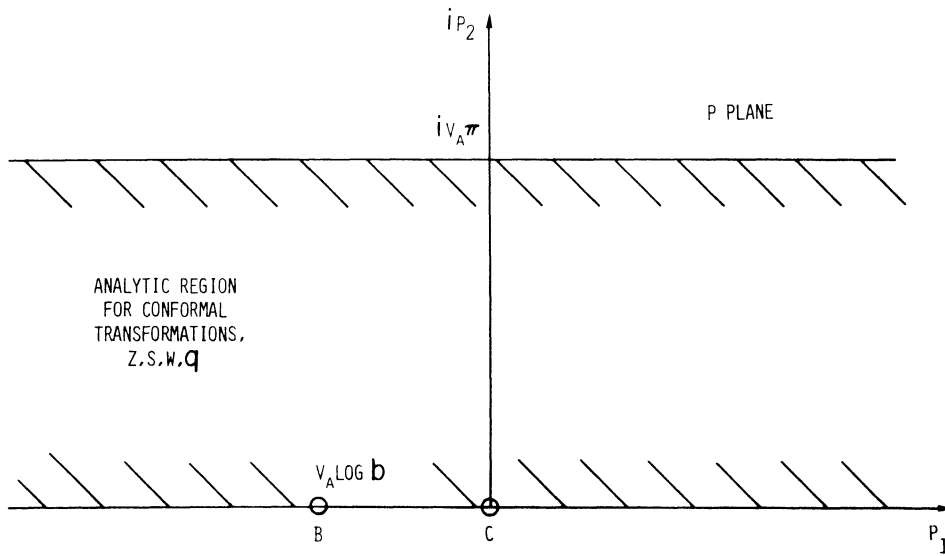


Figure 56 The complex potential plane, p_2 equal to a constant is a streamline. Points A and D are extended.

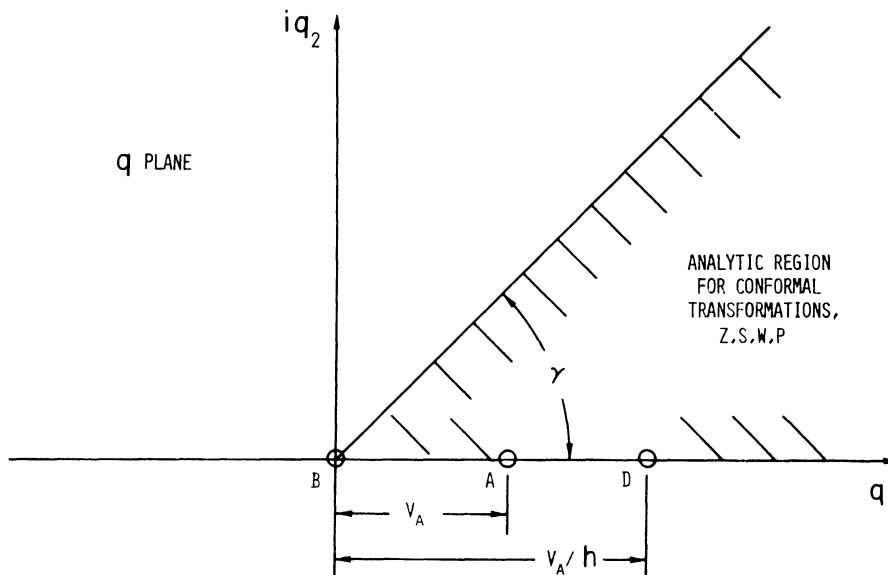


Figure 57 The velocity plane, q . Point C is extended.

The complex velocity,

$$\begin{aligned}\bar{q} &= \frac{dp}{dz} = \frac{dp}{dw} \frac{dw}{dz} , \\ &= \frac{V_A}{w} \frac{w}{R_t} \left(\frac{w-b}{w-1} \right)^{f/g} .\end{aligned}\quad (91)$$

When $w = 0$, $\bar{q} = V_A$. Therefore,

$$V_A = \frac{V_A}{R_t} (b)^{f/g} . \quad (92)$$

When w approaches point D, $\bar{q} = V_D = \frac{V_A}{h}$ since $Q = V_A = hV_D$.

Therefore, from Equation (91),

$$\frac{V_A}{h} = \frac{V_A}{R_t} ,$$

or

$$R_t = h, \quad (93)$$

and from Equation (92),

$$b = (h)^{g/f} . \quad (94)$$

Now that constants R_t and b have been evaluated, the rationalization of the Schwarz Christoffel transformation will be completed. This method of evaluating R_t and b is suggested by Churchill.⁽⁴⁶⁾

The transformation from Equations (90), (93), and (94)

$$\frac{dz}{dw} = \frac{h}{w} \left(\frac{w-1}{w-h^{g/f}} \right)^{f/g} ,$$

can be rationalized by defining a new complex variable

$$s^f = \left(\frac{w-h^{g/f}}{w-1} \right)^{f/g} .$$

Now

$$s = \left(\frac{w-h^{g/f}}{w-1} \right)^{1/g},$$

$$s^g = \frac{w-h^{g/f}}{w-1},$$

so that

$$w = \frac{h^{g/f} - s^g}{1 - s^g}, \quad (95)$$

and so that

$$\frac{dz}{dw} = \frac{h}{s^f} \left(\frac{1 - s^g}{h^{g/f} - s^g} \right). \quad (96)$$

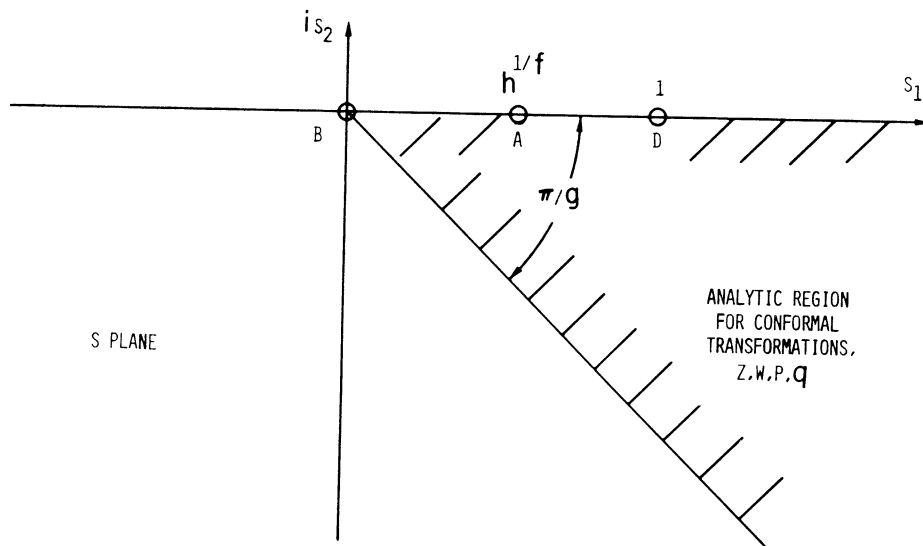


Figure 58 The rationalizing plane, s . Point C is extended.

Writing the Schwarz Christoffel transformation between the z plane and the s plane we get

$$\frac{dz}{ds} = \frac{dz}{dw} \frac{dw}{ds}, \quad (97)$$

where from Equation (95)

$$\frac{dw}{ds} = \frac{d}{ds} \left(\frac{h^{g/f} - s^g}{1 - s^g} \right),$$

$$\frac{dw}{ds} = g s^{g-1} \left[\frac{(h^{g/f} - s^g)}{(1 - s^g)^2} - \frac{1}{(1 - s^g)} \right]. \quad (98)$$

Combining Equations (96), (97), and (98)

$$\frac{dz}{ds} = g h s^{g-f-1} \left[\frac{1}{(1-s^g)} - \frac{1}{(h^{g/f} - s^g)} \right],$$

and integrating

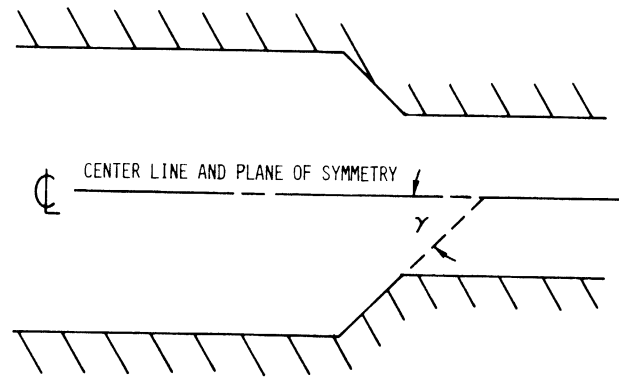
$$z = g h \int \frac{s^{g-f-1} ds}{(1 - s^g)} - g h \int \frac{s^{g-f-1} ds}{(h^{g/f} - s^g)} + T_t .$$

From the algebra these fractions are expanded into partial fractions and integrated.

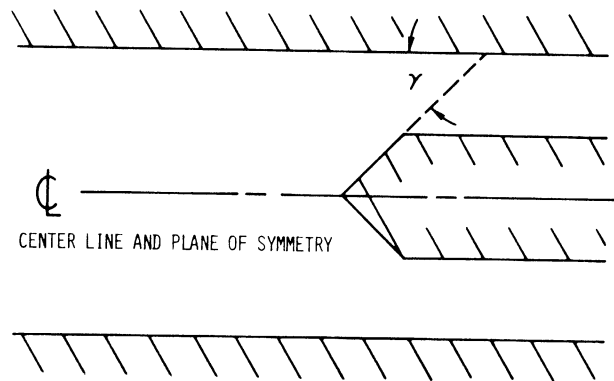
Now that the algorithm for the Schwarz Christoffel transformation is complete, the reflection or symmetry principle⁽⁴⁷⁾ will allow the results to be interpreted as also applying to either physical system shown in Figure 59.

If $\theta = \pi/4$ in Figure 54,

$$z = h \left[\text{Log} \left(\frac{1+s}{1-s} \right) - i \text{Log} \left(\frac{i+s}{i-s} \right) \right] - \left[\text{Log} \left(\frac{h+s}{h-s} \right) - i \text{Log} \left(\frac{ih+s}{ih-s} \right) \right] - (1-h) .$$



a. Converging channel flow



b. Split and separated channel flow

Figure 59 Two additional equivalent physical configurations for the Schwarz Christoffel transformation

APPENDIX D

COMPUTER AIDED ANALYSES AND PLOTTING PROGRAMS

The subroutine and function subprograms collected in the first section of this appendix are used by the remaining programs. The presentation of these remaining programs is in the order in which they appeared in the text of this dissertation. Comment cards are used to describe the various sections of the longer functions, subroutines and programs.

GENERAL PURPOSE SUBPROGRAMS

<u>Subprograms</u>	<u>Brief Description</u>
Real Function RM	Given r_1 , r_2 and the model coefficients from subroutine DCONS, RM returns the image of the real metal path line point in the potential plane.
Real Function DT	Given two path line points and the velocities at these points, DT returns the time increment based on the trapezoidal rule between these points.
Complex Function RINT	Given two vectors in complex form, the times associated with these two vectors, and an intermediate value of time, RINT returns a vector in complex form that is a linear interpolation with respect to time between the two given vectors.
Complex Function SF	Given a point in the potential plane, SF returns a point in the rationalizing plane.

GENERAL PURPOSE SUBPROGRAMS, continued

- Complex Function ZF Given a point in the rationalizing plane, ZF returns a point in the physical plane.
- Complex Function QF Given a point in the rationalizing plane, QF returns a point that is a complex conjugate of the point in the perfect fluid velocity plane as defined in the text.
- Complex Function VF Given the image of r_1, r_2 in the perfect fluid velocity plane, and the partial derivatives from PDPRM, VF returns the modeled real metal velocity vector in complex form.
- Subroutine DGCONS Given r_2 , DGCONS returns the model coefficients and their derivatives with respect to r_2 .
- Subroutine DGCP2 Subroutine called by DGCONS for computational purposes.
- Subroutine PDPRM Given a modeled real metal point, PDPRM returns the partial derivatives of r_2 with respect to p_1 and p_2 using the information from DCONS.
- Subroutine MINV Matrix inversion using Gauss-Jordan reduction with a maximum pivot strategy. This subroutine subprogram is only a slightly modified form of the program presented by Carnahan, Luther, and Wilkes, ⁽⁴⁸⁾ and is not listed.

GENERAL PURPOSE SUBPROGRAMS, continued

- Subroutine MATVEC Multiplies a matrix and a vector. This subroutine subprogram is only a slightly modified form of the subroutine presented by Carnahan, Luther, and Wilkes,⁽⁴⁸⁾ and is not listed.
- Subroutine NLSYS This subroutine solves a system of non-linear equations, given a sufficiently accurate initial estimate of the solution and equations to be solved in Subroutine AUXFCN. This subroutine is the same as that of Brown and Conti⁽⁴⁹⁾ and is not listed.
- Subroutine AUXFCN This subroutine contains the equations to be solved by NLSYS and is listed in the Experimental Modeling and Coefficients Computation section.

GENERAL PURPOSE SUBPROGRAMS, continued

```
REAL FUNCTION RM*(AA,BB,GXX)
```

```
C ... THIS FUNCTION RETURNS RM, THE IMAGE OF A MODELED REAL METAL PATH
C ... LINE POINT IN THE POTENTIAL PLANE, GIVEN THE MODELED PATH LINE
C ... POINT AND THE MODEL COEFFICIENTS.
```

```
IMPLICIT REAL*(A-H)
DOUBLE PRECISION AA,BB,PI,C1,C2
REAL*8 GXX(6)
PI=3.14159265
C1=2.5
C2=C1+7
A1=(BB-GXX(3))*2
A2=-C1*(BB-GXX(3))
A3=(BB-GXX(6))*2
A4=C2*(BB-GXX(6))
IF (A2.GT.70) A2=70
IF (A2.LT.-70) A2=-70
IF (A4.GT.70) A4=70
IF (A4.LT.-70) A4=-70
HI=1.0075
BB1=A1*DLOG(GXX(2))
B1=HI
IF (BB1.LT.174.0) B1=GXX(2)**A1
B2=DEXP(A2)
BB3=A3*DLOG(GXX(5))
B3=HI
IF (BB3.LT.174.0) B3=GXX(5)**A3
B4=DEXP(A4)
RM=GXX(1)/(B1+B2)-GXX(4)/(B3+B4)+AA
RETURN
END
```

```
*****
```

```
REAL FUNCTION DT*(A,B,C,D)
```

```
C ... THIS FUNCTION RETURNS THE TIME INCREMENT DT USING THE TRAPEZOIDAL
C ... RULE, GIVEN TWO PATH LINE POINTS A AND B, AND THEIR RESPECTIVE
C ... VELOCITIES C AND D.
```

```
COMPLEX*16 A,B,C,D
DT=0.5*(1/CDABS(C)+1/CDABS(D))*CDABS(B-A)
RETURN
END
```

```
*****
```

GENERAL PURPOSE SUBPROGRAMS, continued

COMPLEX FUNCTION RINT*16(Z2,Z1,T2,T1,DDT,IT)

C ... THIS FUNCTION RETURNS RINT, A VECTOR IN COMPLEX NOTATION THAT IS A
C ... LINEAR INTERPOLATION WITH RESPECT TO TIME BETWEEN TWO GIVEN
C ... VECTORS.

```

COMPLEX*16 Z1,Z2
DOUBLE PRECISION T,T1,T2,DDT
T=IT*DDT
RINT=((T-T1)/(T2-T1))*(Z2-Z1)+Z1
RETURN
END

```

COMPLEX FUNCTION SF*16(AA,BB,CC)

C ... THIS FUNCTION RETURNS SF, A POINT IN THE RATIONALIZING PLANE,
C ... GIVEN A POINT IN THE POTENTIAL PLANE.

```

COMPLEX*16 AB,AC,AA,CC,SSF
DOUBLE PRECISION BB,BBB
BBB=BB**3
AB=(AA-BBB)/(AA-CC)
AC=CDSORT(AB)
SSF=CDSORT(AC)
SF=CDSORT(SSF)
IF (AIMAG(SF).GT.0) SF=DCONJG(SF)
RETURN
END

```

COMPLEX FUNCTION ZF*16(AA,BB,CC,DD,FE,FA,EB)

C ... THIS FUNCTION RETURNS ZF, A POINT IN THE PHYSICAL PLANE GIVEN A
C ... POINT IN THE RATIONALIZING PLANE. THE SCHWARTZ CHRISTOFFEL
C ... TRANSFORMATION IS REQUIRED TO DEFINE ZF. (SEE APPENDIX C.)

```

COMPLEX*16 ABG,ACG,ADG,AFG,AFG,AGG,AHG,AIG,AR,AC,AD),
IAE,AE,AG,AH,AI,AA,DD),FE,FA,EB
DOUBLE PRECISION BB,CC
ABG=(FA+AA)/(FA-AA)
AH=CDSORT(ABG)
ACG=(-FB+AA)/(-FB-AA)
AC=CDSORT(ACG)
ADG=(FE+AA)/(FE-AA)
AD=CDSORT(ADG)

```

GENERAL PURPOSE SUBPROGRAMS, continued

```

AFG=(DD+AA)/(DD-AA)
AE=CDLOG(AFG)
IF (AIMAG(AFG).EQ.0.AND.REAL(AHG).LT.0) AE=DCONJG(AE)
AFG=(FA*BB+AA)/(FA*BB-AA)
AF=CDLOG(AFG)
AGG=(-FB*BB+AA)/(-FB*BB-AA)
AG=CDLOG(AGG)
AHG=(EE*BB+AA)/(EE*BB-AA)
AH=CDLOG(AHG)
AIG=(BB+AA)/(BB-AA)
AI=CDLOG(AIG)
IF (AIMAG(AIG).EQ.0.AND.REAL(AIG).LT.0) AI=DCONJG(AI)
ZF=BB*(FB*AB-EA*AC-EE*AD+AF)+(-EB*AF+FA*AG+FF*AH-AI)+CC
RETURN
END

```

COMPLEX FUNCTION QF*16(AA,BB,CC)

C ... THIS FUNCTION RETURNS QF, A POINT IN THE CONJUGATE PERFECT
C ... FLUID VELOCITY PLANE GIVEN A POINT IN THE POTENTIAL PLANE, (THIS
C ... IS THE COMPLEX CONJUGATE OF THE QF DEFINED IN THE TEXT.)

```

COMPLEX*16 AA
DOUBLE PRECISION BB,CC
QF=(BB/CC)*AA
RETURN
END

```

COMPLEX FUNCTION VF*16(Q,PDP1,PDP2)

C ... THIS FUNCTION RETURNS VF, THE MODELED REAL METAL VELOCITY VECTOR
C ... IN COMPLEX FORM, GIVEN THE PARTIAL DERIVATIVES FROM PDPRM AND THE
C ... IMAGE OF THE MODELED REAL PATH LINE POINT IN THE PERFECT FLUID
C ... VELOCITY PLANE.

```

COMPLEX*16 Q,CQ,EPF,ENPF
DOUBLE PRECISION VPF,RFPF,SEPF
CQ=DCONJG(Q)
VPF=CDABS(CQ)
EPF=CQ/VPF
RFPF=DBLE(REAL(EPF))
SEPF=DBLE(AIMAG(EPF))
ENPF=DCMPLX(-SEPF,RFPF)
VF=VPF*(PDP2*EPF-PDP1*ENPF)
RETURN
END

```

GENERAL PURPOSE SUBPROGRAMS, continued

```

SUBROUTINE DGCONS (AA,GXX,DGXX)

C ... THIS SUBROUTINE RETURNS GXX(1,...,6), THE MODEL COEFFICIENTS AND
C ... THEIR RESPECTIVE DERIVATIVES DGXX(1,...,6) WITH RESPECT TO THE
C ... MODELED REAL METAL PATH LINE.

      IMPLICIT REAL*8(A-H)
      DOUBLE PRECISION AA,PI,GC
      REAL*8 GXX(6),DPI(7),DGXX(6),GCC(6,7),X(6,7),Y(6,7)
      INTEGER ID(6)
      COMMON GCC,X,Y,ID
      DO 1 I=1,7
1      DPI(I)=X(1,I)
      J=6

C ... THE FOLLOWING CONDITIONAL STATEMENTS DETERMINE THE PROPER INTERVAL
C ... FOR THE SPLINE FITTED MODEL COEFFICIENTS AND THE DERIVATIVES
C ... WHICH ARE RETURNED BY DGCP2.

      IF (AA.GE.DPI(1).AND.AA.LT.DPI(2)) J=1
      IF (AA.GE.DPI(2).AND.AA.LT.DPI(3)) J=2
      IF (AA.GE.DPI(3).AND.AA.LT.DPI(4)) J=3
      IF (AA.GE.DPI(4).AND.AA.LT.DPI(5)) J=4
      IF (AA.GE.DPI(5).AND.AA.LT.DPI(6)) J=5
      DO 2 K=1,6
      CALL DGCP2 (K,J,AA,GC,DGC)
      GXX(K)=GC
2      DGXX(K)=DGC
      RETURN
      END

*****

SUBROUTINE DGCP2 (K,J,AA,GC,DGC)

C ... THIS SUBROUTINE USES THE INTERVAL DETERMINED BY DCONS TO CALCULATE
C ... THE SPLINE FITTED MODEL COEFFICIENTS AND THEIR DERIVATIVES WITH
C ... RESPECT TO THE REAL METAL PATH LINE, WHICH ARE RETURNED TO DCONS.

      IMPLICIT REAL*8(A-H)
      REAL*8 GCC(6,7),S(7),X(6,7),XX(7),Y(6,7),YY(7),HH(7)
      INTEGER ID(6)
      COMMON GCC,X,Y,ID
      M=ID(K)
      DO 1 I=1,M
      XX(I)=X(K,I)
      YY(I)=Y(K,I)
1      S(I)=GCC(K,I)
      DO 2 II=1,6
2      HH(II)=X(1,II+1)-X(1,II)
      L=J
      H=HH(L)

```

GENERAL PURPOSE SUBPROGRAMS, continued

```

      GC=(S(L)/(6*H))*(XX(L+1)-AA)**3+(S(L+1)/(6*H))*(AA-XX(L))**3+(YY(L
1+1)/H-H*(S(L+1)/6))*(AA-XX(L))+(YY(L)/H-H*(S(L)/6))*(XX(L+1)-AA)
      DGC=- (S(L)/(2*H))*(XX(L+1)-AA)**2+(S(L+1)/(2*H))*(AA-XX(L))**2+(YY
1(L+1)/H-H*(S(L+1)/6))-(YY(L)/H-H*(S(L)/6))
      RETURN
      END

```

SUBROUTINE PDPRM (BB,AA,GXX,DGXX,PDP1,PDP2)

C ... GIVEN THE COORDINATES OF A MODELED REAL METAL PATH LINE POINT,
C ... THIS SUBROUTINE RETURNS THE PARTIAL DERIVATIVES OF THE MODELED
C ... REAL METAL PATH LINE WITH RESPECT TO P1 AND P2 IN PDP1 AND PDP2
C ... RESPECTIVELY.

```

      IMPLICIT REAL*8(A-H,O-Z)
      REAL*8 GXX(6),DGXX(6)
      PI=3.14159265
      C1=2.5
      C2=C1+7
      C3=0.0
      A=BB-GXX(3)
      A1=A**2
      A2=-C1*A
      B=BB-GXX(6)
      A3=B**2
      A4=C2*B
      IF (A2.GT.70) A2=70
      IF (A2.LT.-70) A2=-70
      IF (A4.GT.70) A4=70
      IF (A4.LT.-70) A4=-70
      H1=1.0075
      BB1=A1*DLOG(GXX(2))
      H1=H1
      IF (BB1.LT.174.0) H1=GXX(2)**A1
      H2=DEXP(A2)
      BB3=A3*DLOG(GXX(5))
      H3=H1
      IF (BB3.LT.174.0) H3=GXX(5)**A3
      H4=DEXP(A4)
      DD1=1.0047
      D1=H1+H2
      DD1=2*DLOG(D1)
      D1=DD1
      IF (DD1.LT.174.0) D1=H1+H2
      D2=H3+H4
      DD2=2*DLOG(D2)
      D2=DD2
      IF (DD2.LT.174.0) D2=H3+H4
      F1=2*A*DLOG(GXX(2))*H1
      F2=C1*H2
      F3=2*B*DLOG(GXX(5))*H3
      F4=C2*H4
      H1=H2*(-C3*A+C1*DGXX(3))
      F2=A1*(GXX(2)**(A1-1))*DGXX(2)-2*H1*DLOG(GXX(2))*A*DGXX(3)

```

GENERAL PURPOSE SUBPROGRAMS, continued

```

F3=A3*(GXX(5)**(A3-1))*DGXX(5)-2*B3*DLNG(GXX(5))*B*DGXX(5)
F4=B4*(C3*B-C2*DGXX(6))
DNF=-C1*B2+2*B1*DLNG(GXX(2))*A
TW0=C2*B4+2*B3*DLNG(GXX(5))*B
PDP1=(GXX(1)*(DNF)/D1**2-GXX(4)*(TW0)/D2**2)/(1-(-DGXX(1)/D1+DGXX(
14)/D2)-(GXX(1)*(F1+F2)/D1**2-GXX(4)*(F3+F4)/D2**2))
PDP2=1/(1+DGXX(1)/D1-GXX(1)*(F1+F2)/(D1**2)-DGXX(4)/D2+GXX(4)*(F3+
1F4)/(D2**2))
RETURN
END

```

```

*****

```

ORTHOGONAL CURVILINEAR COORDINATE COMPUTATION AND PLOT

```

C ... THIS PROGRAM TOGETHER WITH *PLOTSYS (SEE REFERENCE 42) COMPUTES
C ... AND GENERATES THE PLOT DESCRIPTIONS FOR THE ORTHOGONAL CURVILINEAR
C ... COORDINATE SYSTEM SHOWN IN THE RIGHT HAND SIDE OF FIGURE 12.

      IMPLICIT REAL*8(A-H)
      DOUBLE PRECISION PI,VEL,TB
      COMPLEX*16 E,F,G,SF,ZF,Z,GG,HH
      DIMENSION X(4500), Y(4500)
      DATA H/0.549/,VEL/1.0/,GG/(-.70711,.70711)/,HH/(-.70711,-.70711)/,
      IE/(1.0,0.0)/,F/(0.0,1.0)/
      PI=3.14159265
      C=PI/12
      TB=0.41421
      TAAA=2.50
      TBBB=10.50
      TSS=1.095
      TRN=2*(PI*TSS+TAAA)
      B=-((1-H)*PI)/TB

C ... I IDENTIFIES THE STREAMLINE.

      DO 1 I=1,25
      CO=-(.001838)*(I-25)
      IF (I.EQ.1) CO=0.0
      A=((I-1)*PI)/24-CO

C ... J IDENTIFIES THE POTENTIAL LINE.

      DO 1 J=1,50
      D=-6.870+(J-1)*C

C ... ZF DEFINES THE POSITION OF A POINT (I,J) IN THE PHYSICAL PLANE.

      Z=ZF(SF(CDEXP(DCMPLX(D,A)/VEL),H,E),H,B,E,F,GG,HH)

C ... X AND Y ARE POSITIONS IN THE ABSOLUTE REFERENCE FRAME USED BY
C ... *PLOTSYS.

      X((I-1)*50+J)=AIMAG(Z)*TSS+TAAA
1      Y((I-1)*50+J)=RFAL(Z)*TSS+TBBB

C ... THE NESTED LOOPS TERMINATED AT STATEMENT NUMBER 2 CALCULATE THE
C ... MIRROR IMAGE NEEDED FOR A PLOT SYMMETRICAL TO ITS CENTER LINE.

      DO 2 K=1,25
      DO 2 J=1,50
      X((K-1)*50+1250+J)=-X((K-1)*50+J)+TRN
2      Y((K-1)*50+1250+J)=Y((K-1)*50+J)

C ... LOOPS 3 AND 4 PLOT STREAMLINES.

      DO 3 M=1,25

```

ORTHOGONAL CURVILINEAR COORDINATE COMPUTATION AND PLOT, continued

```
3   CALL PLINE (X((M-1)*50+1),Y((M-1)*50+1),50,1,0,0,0)
    DO 4 L=1,24
4   CALL PLINE (X((L-1)*50+1251),Y((L-1)*50+1251),50,1,0,0,0)

C ... LOOPS 5 AND 6 PLOT POTENTIAL LINES.

    DO 5 M=1,50
5   CALL PLINE (X(M),Y(M),25,50,0,0,0)
    DO 6 L=1,50
6   CALL PLINE (X(1250+L),Y(1250+L),25,50,0,0,0)
    CALL PLTEND
    STOP
    END
```

PERFECT FLUID DEFORMATION FIELD COMPUTATION AND PLOT

C ... THIS PROGRAM TOGETHER WITH *PLOTSYS (SEE REFERENCE 42) COMPUTES
 C ... AND GENERATES THE PLOT DESCRIPTIONS FOR THE SUPERIMPOSED PERFECT
 C ... FLUID DEFORMATION FIELD SHOWN IN FIGURE 35.

```

    IMPLICIT REAL*8(A-H)
    DOUBLE PRECISION PI,VEL,TB,RM
    INTEGER ID(6),IT(25,41)
    REAL*8 GC(6,25),XX(6,7),YY(6,7),GX(6),DGX(6),T(25,41),DGC(6,25)
    I ,DS(25)
    COMPLEX*16 E,F,G,SF,ZF,OF,GG,HH,P,W,S,Z(25,41),Q,VF,ZZ(2),VV(2),
    IZT(25,41),RINT,ZTT,VTT,V(25,41),VT(25,41),ERM,ENRM,ZEBAV,EBAV
    DIMENSION X(2400), Y(2400), XXX(2400), YYY(2400), XS(25), YS(25),
    IXXS(25), YYS(25)
    COMMON GC,XX,YY,ID
    DATA H/0.549/,VEL/1.0/,GG/(-.70711,.70711)/,HH/(-.70711,-.70711)/,
    IE/(1.0,0.0)/,F/(0.0,1.0)/
    DO 1 I=1,6
1   ID(I)=25
    WRITE (6,27) (ID(I),I=1,6)
2   READ (5,30) (DS(I),I=1,25)
    WRITE (6,29) (DS(I),I=1,25)
    PI=3.14159265
  
```

C ... (.942164) IS THE FORESHORTENING CORRECTION.

```

    DDT=(PI/12)*(.942164)
    C=PI/12
    TB=0.41421
    TAAA=2.50
    TBBB=10.50
    TSS=1.095
    TRN=2*(PI*TSS+TAAA)
    SPI=SNGL(PI)
  
```

C ... RO IS THE SCALED RADIUS FOR THE UNDEFORMED CIRCLES.

```

    RO=0.15*(SPI/1.2)*TSS/2.
    RADIAN=180./SPI
  
```

C ... I IDENTIFIES THE PERFECT FLUID PATH LINE.

```

    DO 3 I=1,25
    CO=-(.001838)*(I-25)
    IF (I.F0.1) CO=0.0
    A=((I-1)*PI)/24-CO
    ZZ(1)=0
    ZZ(2)=0
    VV(1)=0
    VV(2)=0
    T(I,1)=0
    IT(I,1)=0
3
  
```

PERFECT FLUID DEFORMATION FIELD COMPUTATION AND PLOT, continued

```

C ... J IDENTIFIES POSITIONS ALONG THE PERFECT FLUID PATH LINE.
      DO 3 J=1,41
      H=-((1-H)*PI)/TB
C ... DS(I) IDENTIFIES THE TIME EQUALS ZERO TIME LINE.
      D=DS(I)+(J-1)*C
C ... ZF IDENTIFIES A POSITION OF A POINT IN THE PHYSICAL PLANE.
      Z(I,J)=ZF(SF(CDEXP(DCMPLX(D,A)/VEL),H,E),H,B,E,F,GG,HH)
C ... X AND Y ARE POSITIONS IN THE ABSOLUTE REFERENCE FRAME USED BY
C ... *PLOTSYS.
      X((I-1)*41+J)=AIMAG(Z(I,J))*TSS+TAAA
      Y((I-1)*41+J)=REAL(Z(I,J))*TSS+TBHH
      IF (I.EQ.1.OR.I.EQ.25) GO TO 3
      Q=QF(SF(CDEXP(DCMPLX(D,A)/VEL),H,E),VEL,H)
C ... V(I,J) IS THE VELOCITY ASSOCIATED WITH EACH PERFECT FLUID PATH
C ... LINE POINT.
      V(I,J)=DCONJG(Q)
      ZZ(1)=ZZ(2)
      ZZ(2)=Z(I,J)
      VV(1)=VV(2)
      VV(2)=V(I,J)
      IF (J.EQ.1) GO TO 3
C ... T(I,J) IS THE VALUE OF THE TIME FUNCTION ALONG THE PERFECT FLUID
C ... PATH LINE, WHICH IS DETERMINED BY SUMMING THE DT'S.
      T(I,J)=T(I,J-1)+DT(ZZ(1),ZZ(2),VV(1),VV(2))
C ... T(I,J) IS CONVERTED TO AN INTEGER.
      ATT=T(I,J)/DDT
      TT=SNGL(ATT)
      IT(I,J)=IFIX(TT)
3     CONTINUE
C ... THE MIRROR IMAGE OF THE PATH LINES IS CALCULATED.
      DO 4 K=1,24
      DO 4 J=1,41
      X((K-1)*41+1025+J)=-X((K-1)*41+J)+TMM
4     Y((K-1)*41+1025+J)=Y((K-1)*41+J)
C ... LOOPS 5 AND 6 PLOT THE PATH LINES.
      DO 5 M=1,25,4
5     CALL PLINE (X((M-1)*41+1),Y((M-1)*41+1),41,1,0,0,0)
      DO 6 L=1,21,4
6     CALL PLINE (X((L-1)*41+1026),Y((L-1)*41+1026),41,1,0,0,0)
C ... LOOPS THROUGH 10 DETERMINE IF THERE ARE ZERO, ONE OR MORE TIME
C ... LINE POINTS BETWEEN TWO PATH LINE POINTS AND ASSURES AN EQUAL

```

PERFECT FLUID DEFORMATION FIELD COMPUTATION AND PLOT, continued

C ... NUMBER OF TIME LINES FOR THE DEFORMATION FIELD. THE VELOCITY
C ... AT EACH TIME LINE POINT IS DETERMINED.

```

      DO 10 I=2,24
      DO 10 J=2,41
      N=J
      L=I
      M=J-1
      IF (I.EQ.24.AND.J.EQ.41) GO TO 7
      GO TO 8
7     R=IT(I,J)
      R=R/2.
      KCH=IT(I,J)/2
      KLAST=IT(I,J)
      IF (R.GT.KCH) KLAST=KLAST-1
8     CONTINUE
      IF (IT(L,M).EQ.IT(L,N)) GO TO 10
      ITT=IT(L,N)-IT(L,M)
      DO 9 KL=1,ITT
      K=IT(L,M)+KL
      ZTT=RINT(Z(L,N),Z(L,M),T(L,N),T(L,M),DDT,K)
      ZT(I,K)=ZTT
      VTT=RINT(V(L,N),V(L,M),T(L,N),T(L,M),DDT,K)
9     VT(I,K)=VTT
10    CONTINUE
      WRITE (6,28) KLAST

```

C ... THE MAJOR AND MINOR DIAMETERS AND THEIR ORIENTATIONS ARE
C ... DETERMINED.

```

      DO 13 KR=1,2
      DO 13 I=3,23,4
      KLL=KLAST-1
      DO 13 K=1,KLL,2
      BEE=COAHS(VT(I,K))
      ERM=VT(I,K)/BEE
      FNRM=F*ERM
      ZEBAV=ZT(I+1,K)-ZT(I-1,K)
      FBAV=ZEBAV/COAHS(ZEBAV)
      FPFE1=DRFAL(ERM*DCONJG(FBAV))
      FPFE=DAFCOS(FPFE1)
      FEE=PI/2-FPFE
      AFE=DTAN(FEE)
      AE1=1/BFE**2
      AE2=-AFF*AE1
      AE3=(BFE**2+AFE**2/BFE**2)
      AE4=-R(I)**2
      AAF1=(AE1+AE3)
      AAE2=DSQRT((AAE1)**2-4.)
      HE1=(AAE1-AAE2)/2
      HE2=(AAE1+AAE2)/2
      DMM2=DSQRT(1./(HE1/(-AE4)))
      DMN2=DSQRT(1./(HE2/(-AE4)))
      ARG=2.*AE2/(AE1-AE3)
      DUTHT=(DATAN(ARG))
      DHFTA=DUTHT/2.
      DTT=DTAN(DHFTA)
      DNM=AE1+2.*AE2*DTT+AE3*DTT**2
      DCH1=-AE4/DNM
      DMQ=DC.H1*(1.+DTT**2)

```

PERFECT FLUID DEFORMATION FIELD COMPUTATION AND PLOT, continued

```

DCH=DSQRT(DM0)
C ... THE MAJOR DIAMETER DIRECTION IS CHECKED AND CORRECTED IF NEEDED.
      IF (SNGL(DCH).NE.SNGL(DMM2)) DHETA=PI/2.+DHETA
      DROT1=DIMAG(ERM)
      DROT2=DARSIN(DROT1)
      ROT=SNGL(DROT2)
      TTHET=SPI/2.-(SNGL(DHETA)+ROT)
      XO=AIMAG(ZT(I,K))*TSS+TAAA
      YO=REAL(ZT(I,K))*TSS+TBBB
      XALPHA=TTHET*RADIAN
      XAEE=SNGL(DMM2)
      XBEE=SNGL(DMM2)

C ... WHEN KR EQUALS TWO, THE SET OF ELLIPSES IN THE MIRROR IMAGE IS
C ... PLOTTED.
      GO TO (12,11), KR
11     XO=-XO+TRN
      XALPHA=-XALPHA

C ... THE STRAIN ELLIPSES ARE PLOTTED.
12     CALL PELIPS (XO,YO,XAEE,XBEE,XALPHA,0.0,360.0,0)
13     CONTINUE

C ... THE POSITIONS OF THE TIME LINE POINTS IN THE ABSOLUTE REFERENCE
C ... FRAME USED BY *PLOTSYS ARE DEFINED.
      DO 14 L=1,KLAST
      DO 14 M=2,24
      XXX((L-1)*23+M-1)=AIMAG(ZT(M,L))*TSS+TAAA
14     YYY((L-1)*23+M-1)=REAL(ZT(M,L))*TSS+TBBB

C ... THE MIRROR IMAGE OF THE TIME LINE POINTS IS DETERMINED.
      DO 15 L=1,KLAST
      DO 15 M=2,24
      XXX((L-1+KLAST)*23+M-1)=-XXX((L-1)*23+M-1)+TRN
15     YYY((L-1+KLAST)*23+M-1)=YYY((L-1)*23+M-1)

C ... PLOT DESCRIPTIONS OF THE TIME LINES ARE GENERATED HERE.
      DO 16 L=2,KLAST,2
16     CALL PLINE (XXX((L-1)*23+1),YYY((L-1)*23+1),23,1,0,0,0)
      DO 17 L=2,KLAST,2
17     CALL PLINE (XXX(23*(L-1+KLAST)+1),YYY(23*(L-1+KLAST)+1),23,1,0,0,0
1)

C ... PLOT DESCRIPTIONS OF THE TIME EQUALS ZERO LEVEL CURVE ARE
C ... GENERATED HERE.
      DO 18 I=2,24
      XS(I)=AIMAG(Z(I,1))*TSS+TAAA
18     YS(I)=REAL(Z(I,1))*TSS+TBBB
      DO 19 I=2,24
      XXS(I)=-XS(I)+TRN
19     YYS(I)=YS(I)
      CALL PLINE (XS(2),YS(2),23,1,0,0,0)

```

PERFECT FLUID DEFORMATION FIELD COMPUTATION AND PLOT, continued

```
      CALL PLINE (XXS(2),YYS(2),23,1,0,0,0)
      CALL PLTFND)

C ... SELECTED NUMERICAL OUTPUT IS PRINTED.

      DO 20 J=1,41
20     WRITE (6,23) (T(I,J),I=5,21,4)
      DO 21 J=1,41
21     WRITE (6,24) (IT(I,J),I=3,23,2)
      WRITE (6,25)
      DO 22 L=1,KLAST
22     WRITE (6,26) (ZT(M,L),M=5,21,4)
      GO TO 2
      STOP

23     FORMAT (5(2X,E13.6))
24     FORMAT (2X,11(2X,I2))
25     FORMAT(2X,'THE LEVEL CURVES OF THE TIME FUNC. FOLLOW')
26     FORMAT (2X,5(2X,E13.6))
27     FORMAT(2X,'ID(I), I=1,6 IS',6(2X,I2,', '))
28     FORMAT(2X,'KLAST IS',2X,I2)
29     FORMAT (1H ,6F13.6)
30     FORMAT (4(2X,E13.6))
      END
```

PERFECT FLUID DEFORMATION FIELD COMPUTATION AND PLOT, continued

Selected values of the time function, $T(I,J)$, are listed below in the following format:

$T(5,1)$, $T(9,1)$, $T(13,1)$, $T(17,1)$, $T(21,1)$

```

.      .      .      .      .
.      .      .      .      .
.      .      .      .      .

```

$T(5,41)$, $T(9,41)$, $T(13,41)$, $T(17,41)$, $T(21,41)$.

0.0	0.0	0.0	0.0	0.0
0.299	0.272	0.253	0.242	0.235
0.608	0.543	0.502	0.478	0.465
0.923	0.808	0.744	0.707	0.687
1.226	1.063	0.977	0.928	0.902
1.503	1.306	1.200	1.141	1.109
1.754	1.534	1.413	1.344	1.307
1.981	1.746	1.613	1.538	1.496
2.189	1.944	1.803	1.721	1.677
2.380	2.128	1.980	1.895	1.848
2.555	2.299	2.147	2.059	2.010
2.718	2.459	2.304	2.214	2.163
2.868	2.607	2.451	2.360	2.308
3.008	2.746	2.588	2.497	2.446
3.136	2.874	2.717	2.627	2.576
3.256	2.994	2.838	2.749	2.699
3.366	3.106	2.952	2.865	2.815
3.467	3.210	3.059	2.974	2.926
3.559	3.306	3.160	3.078	3.032
3.643	3.396	3.255	3.178	3.134
3.719	3.481	3.346	3.273	3.231
3.788	3.562	3.434	3.364	3.325
3.854	3.639	3.518	3.453	3.416
3.920	3.716	3.601	3.540	3.505
3.989	3.792	3.682	3.624	3.591
4.060	3.868	3.762	3.708	3.676
4.133	3.944	3.842	3.790	3.760
4.207	4.021	3.921	3.871	3.842
4.282	4.098	4.000	3.952	3.924
4.359	4.175	4.079	4.032	4.005
4.435	4.253	4.158	4.112	4.086
4.513	4.331	4.237	4.192	4.166
4.590	4.410	4.316	4.271	4.246
4.668	4.488	4.395	4.351	4.326
4.747	4.566	4.474	4.430	4.405
4.825	4.645	4.553	4.509	4.485
4.904	4.724	4.632	4.588	4.564
4.982	4.802	4.711	4.667	4.643
5.061	4.881	4.790	4.746	4.722
5.139	4.960	4.869	4.825	4.801
5.218	5.039	4.947	4.904	4.880

PERFECT FLUID DEFORMATION FIELD COMPUTATION AND PLOT, continued

Selected values of the time function after conversion to integers
are listed below in the following format:

IT(3,1) ,IT(5,1) , ... ,IT(21,1) ,IT(23,1)

.
.
.

IT(3,41),IT(5,41), ... ,IT(21,41),IT(23,41) .

0	0	0	0	0	0	0	0	0	0	0
1	1	1	1	1	1	1	0	0	0	0
2	2	2	2	2	2	1	1	1	1	1
4	3	3	3	3	3	2	2	2	2	2
5	4	4	4	4	4	3	3	3	3	3
6	6	5	5	5	4	4	4	4	4	4
7	7	6	6	5	5	5	5	5	5	5
8	8	7	7	6	6	6	6	6	6	6
9	8	8	7	7	7	7	6	6	6	6
10	9	9	8	8	8	7	7	7	7	7
11	10	9	9	8	8	8	8	8	8	8
11	11	10	9	9	9	9	8	8	8	8
12	11	11	10	10	9	9	9	9	9	9
12	12	11	11	10	10	10	10	10	9	9
13	12	12	11	11	11	10	10	10	10	10
13	13	12	12	11	11	11	11	11	10	10
14	13	13	12	12	11	11	11	11	11	11
14	14	13	13	12	12	12	12	11	11	11
15	14	13	13	13	12	12	12	12	12	12
15	14	14	13	13	13	13	12	12	12	12
15	15	14	14	13	13	13	13	13	13	13
16	15	14	14	14	13	13	13	13	13	13
16	15	15	14	14	14	14	14	13	13	13
16	15	15	15	14	14	14	14	14	14	14
16	16	15	15	15	14	14	14	14	14	14
17	16	16	15	15	15	15	15	14	14	14
17	16	16	15	15	15	15	15	15	15	15
17	17	16	16	16	15	15	15	15	15	15
17	17	16	16	16	16	16	16	15	15	15
18	17	17	16	16	16	16	16	16	16	16
18	17	17	17	17	16	16	16	16	16	16
18	18	17	17	17	17	17	16	16	16	16
19	18	18	17	17	17	17	17	17	17	17
19	18	18	18	17	17	17	17	17	17	17
19	19	18	18	18	18	18	17	17	17	17
20	19	19	18	18	18	18	18	18	18	18
20	19	19	19	18	18	18	18	18	18	18
20	20	19	19	19	19	18	18	18	18	18
21	20	20	19	19	19	19	19	19	19	19
21	20	20	20	19	19	19	19	19	19	19
21	21	20	20	20	20	19	19	19	19	19

PERFECT FLUID DEFORMATION FIELD COMPUTATION AND PLOT, continued

The points in the physical plane,

$$z(I,K) = z_1(I,K) + i z_2(I,K)$$

are on a time function level curve when K is constant. These points are listed below in the following format:

$z_1(5,1)$, $z_2(5,1)$, $z_1(9,1)$, $z_2(9,1)$, $z_1(13,1)$, $z_2(13,1)$,
 $z_1(17,1)$, $z_2(17,1)$, $z_1(21,1)$, $z_2(21,1)$

 $z_1(5,18)$, $z_2(5,18)$, $z_1(9,18)$, $z_2(9,18)$, $z_1(13,18)$, $z_2(13,18)$
 $z_1(17,18)$, $z_2(17,18)$, $z_1(21,18)$, $z_2(21,18)$.

-4.127	0.535	-4.110	1.093	-4.100	1.625
-4.100	2.139	-4.095	2.643		
-3.900	0.553	-3.869	1.116	-3.847	1.645
-3.841	2.154	-3.831	2.651		
-3.675	0.579	-3.626	1.144	-3.592	1.670
-3.577	2.171	-3.563	2.660		
-3.451	0.614	-3.380	1.180	-3.332	1.699
-3.308	2.192	-3.289	2.670		
-3.226	0.660	-3.129	1.223	-3.066	1.734
-3.033	2.215	-3.009	2.682		
-2.994	0.719	-2.872	1.273	-2.793	1.773
-2.751	2.242	-2.721	2.696		
-2.753	0.788	-2.607	1.330	-2.511	1.817
-2.459	2.272	-2.423	2.711		
-2.501	0.864	-2.330	1.394	-2.219	1.866
-2.155	2.305	-2.114	2.727		
-2.236	0.948	-2.040	1.464	-1.912	1.920
-1.839	2.341	-1.791	2.745		
-1.957	1.039	-1.736	1.539	-1.590	1.977
-1.507	2.379	-1.454	2.764		
-1.664	1.135	-1.413	1.620	-1.250	2.037
-1.156	2.418	-1.098	2.783		
-1.351	1.239	-1.069	1.705	-0.886	2.099
-0.785	2.457	-0.723	2.802		
-1.016	1.350	-0.698	1.793	-0.496	2.158
-0.390	2.492	-0.327	2.818		
-0.651	1.467	-0.289	1.875	-0.078	2.207
0.026	2.521	0.088	2.832		
-0.237	1.588	0.156	1.933	0.360	2.238
0.459	2.539	0.518	2.840		
0.241	1.660	0.613	1.959	0.807	2.254
0.901	2.549	0.958	2.845		
0.711	1.676	1.067	1.968	1.256	2.261
1.347	2.554	1.402	2.848		
1.169	1.681	1.518	1.973	1.705	2.265
1.795	2.557	1.849	2.849		

EXPERIMENTAL MODELING COEFFICIENTS COMPUTATION

C ... THIS PROGRAM SOLVES A SYSTEM OF 6 NONLINEAR EQUATIONS FOR THE 6
C ... MODEL COEFFICIENTS.

```

REAL*8 X(6),Y(6),Z(6),C1,C0,T2,PI
COMMON Y,Z,C1
PI=3.14159265
DO 1 I=1,5
  JJ=4*I+1
  C0=(.06872)*(1.-(JJ)/25.)
  T2=(PI/6)*I-C0
  C1=(6/PI)*T2+1
READ (5,2) X(1),X(2),X(3),X(4),X(5),X(6)
READ (5,2) Y(1),Y(2),Y(3),Y(4),Y(5),Y(6)
READ (5,2) Z(1),Z(2),Z(3),Z(4),Z(5),Z(6)
WRITE (6,2) X(1),X(2),X(3),X(4),X(5),X(6)
WRITE (6,2) Y(1),Y(2),Y(3),Y(4),Y(5),Y(6)
WRITE (6,2) Z(1),Z(2),Z(3),Z(4),Z(5),Z(6)
N=6
NUMSIG=3
MAXIT=40
IPRINT=1

```

C ... SEE REFERENCE 49 FOR SUBROUTINE NLSYS.

```

CALL NLSYS (N,NUMSIG,MAXIT,IPRINT,X)
WRITE (6,3)
WRITE (6,2) X(1),X(2),X(3),X(4),X(5),X(6)
WRITE (7,2) X(1),X(2),X(3),X(4),X(5),X(6)
1 CONTINUE
2 FORMAT (3(2X,F13.6)/3(2X,F13.6))
3 FORMAT(9X,'THE CALCULATED COEFFICIENTS ARE')
END

```

C ... THIS SUBROUTINE CONTAINS THE 6 NONLINEAR EQUATIONS TO BE SOLVED.
C ... INTEGER CONSTANT KK WHICH CAN HAVE VALUES OF 1 THROUGH 6
C ... DETERMINES THE PERTINENT EQUATION.

```

SUBROUTINE AUXFCN (XX,FF,KK)
REAL*8 FF,XX(6),YY(6),ZZ(6),C1,C2
COMMON YY,ZZ,C1
I=KK
C2=C1+4
IF (I.EQ.5.OR.I.EQ.6) GO TO 1
FF=XX(1)/(XX(2)**((YY(I)-XX(3))**2)+0)EXP(-C1*(YY(I)-XX(3))) - XX(4)
1/(XX(5)**((YY(I)-XX(6))**2)+0)EXP(C2*(YY(I)-XX(6)))+ZZ(I)

```

EXPERIMENTAL MODELING COEFFICIENTS COMPUTATION, continued

```
      GO TO 2
1     FF=-XX(1)*(2*(YY(I)-XX(3))*DLOG(XX(2))*XX(2)**((YY(I)-XX(3))**2)-C
11*DEXP(-C1*(YY(I)-XX(3))))/(XX(2)**((YY(I)-XX(3))**2)+DEXP(-C1*(YY
2(I)-XX(3))))**2+XX(4)*(2*(YY(I)-XX(6))*DLOG(XX(5))*XX(5)**((YY(I)-
3XX(6))**2)+C2*DEXP(C2*(YY(I)-XX(6))))/(XX(5)**((YY(I)-XX(6))**2)+D
4EXP(C2*(YY(I)-XX(6))))**2+ZZ(I)
2     RETURN
      END
```

EXPERIMENTAL FUNCTION DEFINITION USING A CUBIC SPLINE FIT

```

C ... THIS PROGRAM DETERMINES A CUBIC SPLINE THROUGH THE EXTRAPOLATED
C ... SETS OF MODEL COEFFICIENTS.

      IMPLICIT REAL*8(A-H,O-Z)
      INTEGER ID(6)
      DIMENSION S(50), A(50,50), Y(50), X(50), B(50), H(50), GD(7,6), XX
1(7)
      DO 1 I=1,6
1      ID(I)=7
      DO 2 I=2,6
2      READ (5,19) (GD(I,J),J=1,6)
      DO 3 I=2,6
3      WRITE (6,19) (GD(I,J),J=1,6)
      PI=3.14159265
      XX(1)=0.
      DO 4 I=2,7
4      CO=(.06872)*(1.-(4*(I-1)+1)/25.)
      XX(I)=PI*(I-1)/6-CO
      HHH=XX(2)/(XX(3)-XX(2))

C ... THE MODEL COEFFICIENTS ARE EXTRAPOLATED.

      GD(1,1)=0
      GD(1,2)=GD(2,2)
      GD(1,3)=(GD(2,3)-GD(3,3))*HHH+GD(2,3)
      GD(1,4)=0
      GD(1,5)=GD(2,5)
      GD(1,6)=(GD(2,6)-GD(3,6))*HHH+GD(2,6)
      GD(7,1)=0
      GD(7,2)=GD(6,2)
      GD(7,3)=GD(6,3)
      GD(7,4)=0
      GD(7,5)=GD(6,5)
      GD(7,6)=GD(6,6)
      DO 17 L=1,6
      N=ID(L)
      WRITE (6,20) N
      DO 5 I=1,N
5      M=1
      IF (ID(L).EQ.5) M=I+1
      X(I)=XX(M)
      WRITE (7,18) (X(I),I=1,N)
      WRITE (6,21) (X(I),I=1,N)
      DO 6 I=1,N
      M=1
      IF (ID(L).EQ.5) M=I+1
6      Y(I)=GD(M,L)
      WRITE (7,18) (Y(I),I=1,N)
      WRITE (5,22)
      WRITE (6,21) (Y(I),I=1,N)
      *DX=N-1

```

EXPERIMENTAL FUNCTION DEFINITION USING A CUBIC SPLINE FIT, continued

```

C ... THE LINEAR DIFFERENCE EQUATIONS ARE DETERMINED WITH TWO ADDITIONAL
C ... CONDITIONS BEING SET ON THE PARTICULAR MODEL COEFFICIENT'S SECOND
C ... DERIVATIVEVS WITH RESPECT TO THE PATH LINE AT THE POINTS ADJACENT
C ... TO THE DIE WALL AND CENTER LINE.

      DO 7 I=1,MAX
7     H(I)=X(I+1)-X(I)
      B(1)=((Y(3)-Y(2))/H(2)-(Y(2)-Y(1))/H(1))/(0.5*(H(1)+H(2)))
      B(N)=((Y(N)-Y(N-1))/H(N-1)-(Y(N-1)-Y(N-2))/H(N-2))/(0.5*(H(N-1)+H(
1N-2)))
      IF (L.EQ.2) B(1)=3*(Y(4)-2*Y(3)+Y(2))/H(3)**2
      DO 8 I=2,MAX
8     B(I)=(6.0/H(I))*((Y(I+1)-Y(I))/H(I)-(Y(I)-Y(I-1))/H(I-1))
      A(1,1)=0.
      A(1,2)=1.
      DO 9 J=3,N
9     A(1,J)=0.
      MAX2=N-2
      DO 10 J=1,MAX2
10    A(N,J)=0.
      A(N,MAX)=1.
      A(N,N)=0.
      DO 15 K=2,MAX
      K1=K-1
      I=K
      K2=K+1
      DO 15 J=1,N
      IF (J.EQ.K1) GO TO 11
      IF (J.EQ.K) GO TO 12
      IF (J.EQ.K2) GO TO 13
      GO TO 14
11    A(I,J)=H(I-1)/H(I)
      GO TO 15
12    A(I,J)=2*(H(I)+H(I-1))/H(I)
      GO TO 15
13    A(I,J)=1.
      GO TO 15
14    A(I,J)=0.
15    CONTINUE
      WRITE (6,23)
      DO 16 I=1,N
16    WRITE (6,21) (A(I,J),J=1,N)
      EPS=0.1E-19

C ... MINV INVERTS THE LINEAR DIFFERENCE MATRIX.

      CALL MINV (N,EPS,A,DEFER)
      WRITE (6,24) DEFER

C ... MATVFC DETERMINES THE UNKNOWN SECOND DERIVATIVES THAT DEFINE
C ... THE SPLINES USING THE OUTPUT OF MINV.

      CALL MATVFC (A,B,S,N,N)
      WRITE (5,25)
      WRITE (7,21) (S(I),I=1,N)
      WRITE (6,21) (S(I),I=1,N)
17    CONTINUE

18    FORMAT (4(2X,F13.6))

```

EXPERIMENTAL FUNCTION DEFINITION USING A CUBIC SPLINE FIT, continued

```
19  FORMAT (3(2X,F13.6))
20  FORMAT(1H1,'N IS',2X,I2//'THE X VECTOR IS'//)
21  FORMAT (4(2X,F13.6))
22  FORMAT(1H0,'THE Y VECTOR IS'/1H )
23  FORMAT(1H0,'THE LINEAR DIFFERENCE MATRIX IS'//)
24  FORMAT(1H0,'DETER IS',2X,F13.6)
25  FORMAT(1H0,'THE SECOND DERRIVATIVE VECTOR IS'//)
    END
```

```
*****
```

EXPERIMENTAL FUNCTION DEFINITION USING A CUBIC SPLINE FIT, continued

The following output is needed to plot the spline fitted model coefficient A shown in Figure 48. The x vector contains values of experimentally selected real metal path lines, while the y vector contains values of model coefficient A for these selected path lines. The second derivative vector defines the cubic splines, and similar output is generated for the remaining model coefficients.

N IS 7

THE X VECTOR IS

0.0	0.486839D 00	0.101779D 01	0.154874D 01
0.207969D 01	0.261064D 01	0.314159D 01	

THE Y VECTOR IS

0.0	0.186677D 00	0.263787D 00	0.283377D 00
0.247806D 00	0.147152D 00	0.0	

THE LINEAR DIFFERENCE MATRIX IS

0.0	0.100000D 01	0.0	0.0
0.0	0.0	0.0	
0.916919D 00	0.383384D 01	0.100000D 01	0.0
0.0	0.0	0.0	
0.0	0.100000D 01	0.400000D 01	0.100000D 01
0.0	0.0	0.0	
0.0	0.0	0.100000D 01	0.400000D 01
0.100000D 01	0.0	0.0	
0.0	0.0	0.0	0.100000D 01
0.400000D 01	0.100000D 01	0.0	
0.0	0.0	0.0	0.0
0.100000D 01	0.400000D 01	0.100000D 01	
0.0	0.0	0.0	0.0
0.0	0.100000D 01	0.0	

DETER IS 0.513475D 02

THE SECOND DERIVATIVE VECTOR IS

-0.825438D 00	-0.468107D 00	-0.140464D 00	-0.194264D 00
-0.256497D 00	-0.164940D 00	-0.733827D-01	

MODELED REAL METAL AND PERFECT FLUID VELOCITY HODOGRAPH PLOTS

```

C ... THIS PROGRAM TOGETHER WITH *PLOTSYS COMPUTES AND GENERATES THE
C ... PLOT DESCRIPTIONS FOR THE MODELED REAL METAL VELOCITIES AND THE
C ... PERFECT FLUID VELOCITIES AS A FUNCTION OF INCREMENTAL STEPS DOWN
C ... THE MODELED REAL METAL PATH LINE.

      IMPLICIT REAL*8(A-H)
      DOUBLE PRECISION PI,VEL,TH
      INTEGER ID(6)
      REAL*8 GC(6,7),XX(6,7),YY(6,7),GX(6),DGX(6)
      COMPLEX*16 E,F,G,SF,ZF,OF,GG,HH,P,W,S,Z,Q,VF,V
      DIMENSION X(1200), Y(1200), XXX(1200), YYY(1200)
      COMMON GC,XX,YY,ID
      DATA H/0.724/,VEL/1.0/,GG/(-.70711,.70711)/,HH/(-.70711,-.70711)/,
      LF/(1.0,0.0)/,F/(0.0,1.0)/
      DO 1 I=1,6
1      ID(I)=7
      WRITE (6,9) (ID(I),I=1,6)
      DO 2 I=1,6
      READ (5,10) (XX(I,J),J=1,7)
      READ (5,10) (YY(I,J),J=1,7)
2      READ (5,10) (GC(I,J),J=1,7)
      DO 3 I=1,6
3      WRITE (6,11) (XX(I,J),J=1,7)
      DO 4 I=1,6
4      WRITE (6,11) (YY(I,J),J=1,7)
      DO 5 I=1,6
5      WRITE (6,11) (GC(I,J),J=1,7)
      TAAA=-2
      TAA=TAAA
      TBBB=3
      TBB=13
      TSS=8
      PI=3.14159265

C ... I IDENTIFIES THE MODELED REAL METAL PATH LINE.

      DO 6 I=3,11,2
      CO=(.068/2)*(1.0-I/13.)*(26/25.)
      A=((I-1)*PI)/12-CO

C ... DCONS DETERMINES THE APPROPRIATE MODEL COEFFICIENTS AND THEIR
C ... DERIVATIVES.

      CALL DDCONS (A,GX,DGX)

C ... J IDENTIFIES A POSITION ON A PATH LINE.

      DO 6 J=1,81
      TB=0.41421
      B=-((1-H)*PI)/TB
      C=PI/24

```

MODELED REAL METAL AND PERFECT FLUID VELOCITY HODOGRAPH PLOTS, continued

```

D=-6.500+(J-1)*C
C ... RM DETERMINES THE POSITION OF THE MODELED REAL METAL PATH LINE
C ... POINT IN THE POTENTIAL PLANE.
      AA=RM(A,D,GX)
C ... QF DETERMINES THE PERFECT FLUID VELOCITY.
      Q=QF(SF(CDEXP(DCMPLX(D,AA)/VEL),H,E),VEL,H)
C ... P DPRM DETERMINES THE PARTIAL DERIVATIVES REQUIRED TO CALCULATE
C ... THE MODELED REAL METAL VELOCITY.
      CALL P DPRM (D,A,GX,DGX,PDP1,PDP2)
C ... VF DETERMINES THE MODELED REAL METAL VELOCITY.
      V=VF(Q,PDP1,PDP2)
      O=DCONJG(Q)
C ... X AND Y ARE THE POSITIONS OF THE FREE VECTOR TIP ASSOCIATED WITH
C ... MODELED REAL METAL VELOCITIES IN THE ABSOLUTE REFERENCE FRAME
C ... *PLOTSYS CAN USE.
      X((I-1)*R1+J)=REAL(V)*TSS+TAAA
      Y((I-1)*R1+J)=AIMAG(V)*TSS+TBBB
C ... XXX AND YYY ARE POSITIONS ASSOCIATED WITH THE PERFECT FLUID
C ... VELOCITIES IN THE ABSOLUTE REFERENCE FRAME *PLOTSYS CAN USE.
      XXX((I-1)*R1+J)=REAL(Q)*TSS+TAA
      YYY((I-1)*R1+J)=AIMAG(Q)*TSS+TBB
6
C ... THE PLOT DESCRIPTIONS ARE GENERATE HERE.
      CALL PFNHP (6.0,3.0)
      CALL PFNDN (10.0,3.0)
      CALL PFNHP (0.0,0.0)
      DO 7 M=3,11,2
7      CALL PLINE (X((M-1)*R1+1),Y((M-1)*R1+1),R1,1,0,0,0)
      CALL PFNHP (6.0,13.0)
      CALL PFNDN (10.0,13.0)
      CALL PFNHP (0.0,0.0)
      DO 8 L=3,11,2
8      CALL PLINE (XXX((L-1)*R1+1),YYY((L-1)*R1+1),R1,1,0,0,0)
      CALL PLTFND)
9      FORMAT(2X,'10(I), I=1,6 IS',6(2X,I2,', '))
10     FORMAT (4(2X,F13.6))
11     FORMAT (7(2X,F13.6))
      END)

```

```

*****

```


MODELED REAL METAL DEFORMATION FIELD COMPUTATION AND PLOT

```

C ... THIS PROGRAM TOGETHER WITH *PLOTSYS COMPUTES AND GENERATES THE
C ... PLOT DESCRIPTIONS FOR THE MODELED REAL METAL DEFORMATION FIELDS
C ... USING DASHED LINES.

      IMPLICIT REAL*8(A-H)
      DOUBLE PRECISION PI,VFL,TB,RM
      INTEGER ID(6),IT(25,41)
      REAL*8 GC(6,7),XX(6,7),YY(6,7),GX(6),DGX(6),T(25,41),DS(25)
      COMPLEX*16 E,F,G,SF,ZF,QF,GG,HH,P,W,S,Z(25,41),Q,VF,ZZ(2),VV(2),
      IZT(25,41),RINT,ZTT,VTT,V(25,41),VT(25,41),ERM,ENRM,7EBAV,EBAV
      DIMENSION X(2400), Y(2400), XXX(2400), YYY(2400), XS(25), YS(25),
      IXXS(25), YYS(25)
      COMMON GC,XX,YY,ID
      DATA VFL/1.0/,GG/(-.70711,.70711)/,HH/(-.70711,-.70711)/,E/(1.0,0.
      10)/,F/(0.0,1.0)/
      DO 1 I=1,6
1      ID(I)=7
      WRITE (6,33) (ID(I),I=1,6)
2      DO 3 I=1,6
      READ (5,35) (XX(I,J),J=1,7)
      READ (5,35) (YY(I,J),J=1,7)
3      READ (5,35) (GC(I,J),J=1,7)
      READ (5,27) H,ADDT
      READ (5,38) (DS(I),I=1,25)
      DO 4 I=1,6
4      WRITE (6,36) (XX(I,J),J=1,7)
      DO 5 I=1,6
      WRITE (6,36) (YY(I,J),J=1,7)
      DO 6 I=1,6
6      WRITE (6,36) (GC(I,J),J=1,7)
      WRITE (6,28) H,ADDT
      WRITE (6,37) (DS(I),I=1,25)
      PI=3.14159265

C ... ADDT IS THE FORESHORTENING CORRECTION.

      DDT=(PI/12)*ADDT
      C=PI/12
      TB=0.41421
      TAAA=2.50
      TBBB=10.50
      TSS=1.1013
      TRN=2*(PI*TSS+TAAA)
      SPI=SNGL(PI)

C ... R0 IS THE SCALED RADIUS FOR THE UNDEFORMED CIRCLES.

      R0=0.15*(SPI/1.2)*TSS/2.
      RADIAN=180./SPI

C ... I IDENTIFIES THE MODELED REAL METAL PATH LINE.

```

MODELED REAL METAL DEFORMATION FIELD COMPUTATION AND PLOT, continued

```

      DO 7 I=1,25
      CO=-(.001838)*(I-25)
      IF (I.EQ.1) CO=0.0
      A=((I-1)*PI)/24-CO

C ... DCONS DETERMINES THE APPROPRIATE MODEL COEFFICIENTS AND THEIR
C ... DERIVATIVES.

      CALL DGCONS (A,GX,DGX)
      ZZ(1)=0
      ZZ(2)=0
      VV(1)=0
      VV(2)=0
      T(I,1)=0
      IT(I,1)=0

C ... J IDENTIFIES THE POSITIONS ALONG THE MODELED REAL METAL PATH LINE.

      DO 7 J=1,41
      B=-((1-H)*PI)/TB

C ... DS(I) IDENTIFIES THE TIME EQUALS ZERO TIME LINE.

      D=DS(I)+(J-1)*C

C ... RM DETERMINES THE POSITION OF THE MODELED REAL METAL PATH LINE
C ... POINT IN THE POTENTIAL PLANE.

      AA=RM(A,D,GX)
      IF (I.EQ.1.OR.I.EQ.25) AA=A

C ... ZF IDENTIFIES A POSITION OF A POINT IN THE PHYSICAL PLANE.

      Z(I,J)=ZF(SF(CDEXP(DCMPLX(D,AA)/VEL),H,F),H,B,F,F,GG,HH)

C ... X AND Y ARE POSITIONS IN THE ABSOLUTE REFERENCE FRAME USED BY
C ... *PLOTSYS.

      X((I-1)*41+J)=A[MAG(Z(I,J))*TSS+TAAA
      Y((I-1)*41+J)=REAL(Z(I,J))*TSS+TBHH
      IF (I.EQ.1.OR.I.EQ.25) GO TO 7

C ... QF DETERMINES THE PERFECT FLUID VELOCITY.

      QF=QF(SF(CDEXP(DCMPLX(D,AA)/VEL),H,F),VEL,H)

C ... PDP1M DETERMINES THE PARTIAL DERIVATIVES REQUIRED TO CALCULATE
C ... THE MODELED REAL METAL VELOCITY.

      CALL PDP1M (D,A,GX,DGX,PDP1,PDP2)

C ... V(I,J) IS THE VELOCITY ASSOCIATED WITH EACH MODELED REAL METAL
C ... PATH LINE POINT.

      V(I,J)=VF(Q,PDP1,PDP2)
      ZZ(1)=ZZ(2)
      Z(2)=Z(I,J)
      VV(1)=VV(2)
      VV(2)=V(I,J)

```

MODELED REAL METAL DEFORMATION FIELD COMPUTATION AND PLOT, continued

```

      IF (J.EQ.1) GO TO 7
C ... T(I,J) IS THE VALUE OF THE TIME FUNCTION ALONG THE MODELED REAL
C ... METAL PATH LINE, WHICH IS DETERMINED BY SUMMING THE DT'S.
      T(I,J)=T(I,J-1)+DT(ZZ(1),ZZ(2),VV(1),VV(2))
C ... T(I,J) IS CONVERTED TO AN INTEGER.
      ATT=T(I,J)/DDT
      TT=SNGL(ATT)
      IT(I,J)=IFIX(TT)
7      CONTINUE
C ... THE MIRROR IMAGE OF THE PATH LINES IS CALCULATED.
      DO 8 K=1,24
      DO 8 J=1,41
      X((K-1)*41+1025+J)=-X((K-1)*41+J)+TRN
8      Y((K-1)*41+1025+J)=Y((K-1)*41+J)
C ... LOOPS 9 AND 10 PLOT THE PATH LINES.
      DO 9 M=1,25,4
9      CALL PDSHLN (X((M-1)*41+1),Y((M-1)*41+1),41,1,0.08,0)
      DO 10 L=1,21,4
10     CALL PDSHLN (X((L-1)*41+1026),Y((L-1)*41+1026),41,1,0.08,0)
C ... LOOPS THROUGH 14 DETERMINE IF THERE ARE ZERO, ONE OR MORE TIME
C ... LINE POINTS BETWEEN TWO PATH LINE POINTS AND ASSURES AN EQUAL
C ... NUMBER OF TIME LINES FOR THE DEFORMATION FIELD. THE VELOCITY
C ... AT EACH TIME LINE POINT IS DETERMINED.
      DO 14 I=2,24
      DO 14 J=2,41
      N=J
      L=1
      M=J-1
      IF (I.EQ.24.AND.J.EQ.41) GO TO 11
      GO TO 12
11     R=IT(I,J)
      R=R/2.
      KCH=IT(I,J)/2
      KLAST=IT(I,J)
      IF (R.GT.KCH) KLAST=KLAST-1
12     CONTINUE
      IF (IT(L,M).EQ.IT(L,N)) GO TO 14
      ITT=IT(L,N)-IT(L,M)
      DO 13 KL=1,ITT
      K=IT(L,M)+KL
      ZTT=RINT(Z(L,N),Z(L,M),T(L,N),T(L,M),DDT,K)
      ZT(I,K)=ZTT
      VTT=RINT(V(L,N),V(L,M),T(L,N),T(L,M),DDT,K)
13     VT(I,K)=VTT
14     CONTINUE
      WRITE (6,34) KLAST
C ... THE MAJOR AND MINOR DIAMETERS AND THEIR ORIENTATIONS ARE
C ... DETERMINED.

```

MODELED REAL METAL DEFORMATION FIELD COMPUTATION AND PLOT, continued

```

DO 17 KR=1,2
DO 17 I=3,23,4
KLL=KLAST-1
DO 17 K=1,KLL,2
BEE=CDABS(VT(I,K))
ERM=VT(I,K)/BEE
ENRM=F*ERM
ZEBAV=ZT(I+1,K)-ZT(I-1,K)
EBAV=ZEBAV/CDABS(ZEBAV)
FP EE1=DREAL(ERM*DCONJG(EBAV))
FP EE2=DARCOS(FP EE1)
FEE=PI/2-FP EE2
AEE=DTAN(FEE)
AE1=1/BEE**2
AE2=-AEE*AE1
AE3=(BEE**2+AEE**2/BEE**2)
AE4=-R0**2
AAE1=(AE1+AE3)
AAE2=DSQRT((AAE1)**2-4.)
BE1=(AAE1-AAE2)/2
BE2=(AAE1+AAE2)/2
DMM2=DSQRT(1./(BE1/(-AE4)))
DMN2=DSQRT(1./(BE2/(-AE4)))
ARG=2.*AE2/(AE1-AE3)
DUTHET=(DATAN(ARG))
DHETA=DUTHET/2.
DTT=DTAN(DHETA)
DNM=AE1+2.*AE2*DTT+AE3*DTT**2
DCH1=-AE4/DNM
DMQ=DCH1*(1.+DTT**2)
DCH=DSQRT(DMQ)

C ... THE MAJOR DIAMETER DIRECTION IS CHECKED AND CORRECTED IF NEEDED.
IF (SNGL(DCH).NE.SNGL(DMM2)) DHETA=PI/2.+DHETA
DR0T1=DIMAG(ERM)
DR0T2=DARSIN(DR0T1)
ROT=SNGL(DR0T2)
TTHFT=SPI/2.-(SNGL(DHETA)+ROT)
X0=AIMAG(ZT(I,K))*TSS+TAAA
Y0=REAL(ZT(I,K))*TSS+TBBB
XALPHA=TTHFT*RADIAN
XAEE=SNGL(DMM2)
XBEE=SNGL(DMN2)

C ... WHEN KR EQUALS TWO, THE SET OF ELLIPSES IN THE MIRROR IMAGE IS
C ... PLOTTED.
GO TO (16,15), KR
15 X0=-X0+TRN
XALPHA=-XALPHA

C ... THE STRAIN ELLIPSES ARE PLOTTED.
16 CALL PFLIPS (X0,Y0,XAEE,XBEE,XALPHA,0.0,360.0,0)
17 CONTINUE

C ... THE POSITIONS OF THE TIME LINE POINTS IN THE ABSOLUTE REFERENCE
C ... FRAME USED BY *PLOTSYS ARE DEFINED.

```

MODELED REAL METAL DEFORMATION FIELD COMPUTATION AND PLOT, continued

```

      DO 18 L=1,KLAST
      DO 18 M=2,24
      XXX((L-1)*23+M-1)=AIMAG(ZT(M,L))*TSS+TAAA
18   YYY((L-1)*23+M-1)=REAL(ZT(M,L))*TSS+TBBB
C ... THE MIRROR IMAGE OF THE TIME LINE POINTS IS DETERMINED.
      DO 19 L=1,KLAST
      DO 19 M=2,24
      XXX((L-1+KLAST)*23+M-1)=-XXX((L-1)*23+M-1)+TRN
19   YYY((L-1+KLAST)*23+M-1)=YYY((L-1)*23+M-1)
C ... PLOT DESCRIPTIONS OF THE TIME LINES ARE GENERATED HERE.
      DO 20 L=2,KLAST,2
20   CALL PDSHLN (XXX((L-1)*23+1),YYY((L-1)*23+1),23,1,0.08,0)
      DO 21 L=2,KLAST,2
21   CALL PDSHLN (XXX(23*(L-1+KLAST)+1),YYY(23*(L-1+KLAST)+1),23,1,0.08
      1,0)
C ... PLOT DESCRIPTIONS OF THE TIME EQUALS ZERO LEVEL CURVE ARE
C ... GENERATED HERE.
      DO 22 I=2,24
      XS(I)=AIMAG(Z(I,1))*TSS+TAAA
22   YS(I)=REAL(Z(I,1))*TSS+TBBB
      DO 23 I=2,24
      XXS(I)=-XS(I)+TRN
23   YYS(I)=YS(I)
      CALL PDSHLN (XS(2),YS(2),23,1,0.08,0)
      CALL PDSHLN (XXS(2),YYS(2),23,1,0.08,0)
      CALL PLTFND
C ... SELECTED NUMERICAL OUTPUT IS PRINTED.
      DO 24 J=1,41
24   WRITE (6,29) (T(I,J),I=5,21,4)
      DO 25 J=1,41
25   WRITE (6,30) (IT(I,J),I=2,24)
      WRITE (6,31)
      DO 26 L=1,KLAST
26   WRITE (6,32) (ZT(M,L),M=5,21,4)
      GO TO 2
      STOP
27   FORMAT (2X,E13.6,2X,F13.6)
28   FORMAT(1X,/, 'H IS',1X,E13.6,/,1X, 'A0DT IS',1X,E13.6,/)
29   FORMAT (5(2X,E13.6))
30   FORMAT (2X,23(2X,I2))
31   FORMAT(2X, 'THE LEVEL CURVES OF THE TIME FUNC. FOLLOW')
32   FORMAT (2X,5(2X,E13.6))
33   FORMAT(2X, 'ID(I), I=1,6 IS',6(2X,I2,','))
34   FORMAT(2X, 'KLAST IS',2X,I2)
35   FORMAT (4(2X,F13.6))
36   FORMAT (7(2X,F13.6))
37   FORMAT (1H ,6F13.6)
38   FORMAT (4(2X,F13.6))
      END)

```

MODELED REAL METAL DEFORMATION FIELD COMPUTATION AND PLOT, continued

Selected values of the time function, $T(I,J)$, used to determine the modeled real metal deformation field shown in Figure 42 are listed below in the following format:

T(5,1) ,T(9,1) ,T(13,1) ,T(17,1) ,T(21,1)

 T(5,41),T(9,41),T(13,41),T(17,41),T(21,41)

0.0	0.0	0.0	0.0	0.0
0.271	0.258	0.254	0.248	0.247
0.552	0.518	0.506	0.494	0.490
0.841	0.775	0.752	0.734	0.727
1.120	1.023	0.989	0.966	0.958
1.377	1.259	1.213	1.189	1.180
1.614	1.480	1.424	1.398	1.392
1.834	1.688	1.621	1.593	1.590
2.040	1.885	1.808	1.775	1.773
2.233	2.070	1.985	1.946	1.942
2.413	2.246	2.153	2.107	2.096
2.584	2.413	2.314	2.258	2.237
2.745	2.573	2.466	2.400	2.365
2.897	2.725	2.610	2.531	2.481
3.043	2.869	2.745	2.652	2.588
3.181	3.003	2.869	2.763	2.690
3.311	3.126	2.983	2.866	2.789
3.432	3.237	3.089	2.964	2.886
3.541	3.337	3.187	3.058	2.981
3.638	3.428	3.280	3.150	3.075
3.723	3.513	3.368	3.239	3.168
3.799	3.593	3.454	3.326	3.259
3.870	3.670	3.537	3.411	3.348
3.939	3.746	3.618	3.495	3.435
4.009	3.822	3.699	3.579	3.521
4.081	3.897	3.778	3.661	3.606
4.154	3.974	3.858	3.743	3.689
4.229	4.050	3.937	3.824	3.772
4.305	4.128	4.016	3.904	3.853
4.381	4.205	4.095	3.985	3.934
4.458	4.283	4.174	4.065	4.015
4.535	4.361	4.253	4.144	4.095
4.613	4.439	4.332	4.224	4.175
4.691	4.518	4.411	4.303	4.255
4.769	4.596	4.490	4.382	4.334
4.848	4.675	4.569	4.462	4.414
4.926	4.753	4.648	4.541	4.493
5.005	4.832	4.726	4.620	4.572
5.083	4.911	4.805	4.699	4.651
5.162	4.990	4.884	4.778	4.730
5.241	5.068	4.963	4.857	4.809

MODELED REAL METAL DEFORMATION FIELD COMPUTATION AND PLOT, continued

The time function after conversion to integers used to determine the modeled real metal deformation field shown in Figure 42 is listed below in the following format:

```

IT(3,1) ,IT(5,1) , ... ,IT(21,1) ,IT(23,1)
.           .           ...           .           .
.           .           ...           .           .
.           .           ...           .           .
IT(3,41),IT(5,41), ... ,IT(21,41),IT(23,41) .
    
```

0	0	0	0	0	0	0	0	0	0	0
1	1	1	1	1	1	1	1	1	1	1
2	2	2	2	2	2	2	2	1	1	1
3	3	3	3	3	3	3	2	2	2	2
4	4	4	4	4	4	3	3	3	3	3
5	5	5	5	4	4	4	4	4	4	4
6	6	6	5	5	5	5	5	5	5	5
7	7	7	6	6	6	6	6	6	6	6
8	8	7	7	7	7	7	7	7	7	7
9	9	8	8	8	8	7	7	7	7	7
10	9	9	9	8	8	8	8	8	8	8
10	10	10	9	9	9	9	9	9	9	9
11	11	10	10	10	9	9	9	9	9	9
12	11	11	11	10	10	10	10	10	10	10
12	12	11	11	11	11	10	10	10	10	10
13	12	12	12	11	11	11	11	11	10	10
13	13	13	12	12	12	11	11	11	11	11
14	13	13	13	12	12	12	12	11	11	11
14	14	13	13	13	12	12	12	12	12	12
15	14	14	13	13	13	13	12	12	12	12
15	15	14	14	13	13	13	13	12	12	12
15	15	14	14	14	14	13	13	13	13	13
16	15	15	14	14	14	14	13	13	13	13
16	15	15	15	14	14	14	14	14	13	13
16	16	15	15	15	14	14	14	14	14	14
16	16	16	15	15	15	15	14	14	14	14
17	16	16	16	15	15	15	15	15	14	14
17	17	16	16	16	15	15	15	15	15	15
17	17	17	16	16	16	16	15	15	15	15
18	17	17	17	16	16	16	16	16	15	15
18	18	17	17	17	16	16	16	16	16	16
18	18	17	17	17	17	17	16	16	16	16
18	18	18	17	17	17	17	17	16	16	16
19	19	18	18	18	17	17	17	17	17	17
19	19	18	18	18	18	17	17	17	17	17
19	19	19	18	18	18	18	17	17	17	17
20	19	19	19	19	18	18	18	18	18	18
20	20	19	19	19	19	18	18	18	18	18
20	20	20	19	19	19	19	19	18	18	18
21	20	20	20	20	19	19	19	19	19	19
21	21	20	20	20	20	19	19	19	19	19

MODELED REAL METAL DEFORMATION FIELD COMPUTATION AND PLOT, continued

The points in the physical plane,

$$z(I,K) = z_1(I,K) + i z_2(I,K)$$

are on a time function level curve when K is a constant, in Figure 42.

These points are listed below in the following format:

$z_1(5,1)$, $z_2(5,1)$, $z_1(9,1)$, $z_2(9,1)$, $z_1(13,1)$, $z_2(13,1)$,
 $z_1(17,1)$, $z_2(17,1)$, $z_1(21,1)$, $z_2(21,1)$

 $z_1(5,18)$, $z_2(5,18)$, $z_1(9,18)$, $z_2(9,18)$, $z_1(13,18)$, $z_2(13,18)$,
 $z_1(17,18)$, $z_2(17,18)$, $z_1(21,18)$, $z_2(21,18)$.

-4.099	0.467	-4.090	1.009	-4.095	1.546
-4.104	2.081	-4.107	2.612		
-3.846	0.476	-3.835	1.020	-3.843	1.555
-3.853	2.087	-3.858	2.615		
-3.596	0.504	-3.580	1.046	-3.590	1.572
-3.601	2.097	-3.607	2.620		
-3.349	0.554	-3.325	1.091	-3.333	1.603
-3.345	2.115	-3.352	2.628		
-3.103	0.626	-3.067	1.156	-3.070	1.654
-3.083	2.145	-3.093	2.640		
-2.854	0.715	-2.806	1.239	-2.798	1.725
-2.809	2.192	-2.823	2.662		
-2.600	0.810	-2.538	1.329	-2.517	1.805
-2.523	2.255	-2.539	2.695		
-2.341	0.908	-2.263	1.418	-2.228	1.887
-2.222	2.324	-2.232	2.737		
-2.074	1.006	-1.982	1.509	-1.931	1.973
-1.906	2.402	-1.894	2.789		
-1.798	1.108	-1.695	1.605	-1.627	2.068
-1.569	2.483	-1.510	2.837		
-1.515	1.214	-1.404	1.708	-1.308	2.158
-1.195	2.535	-1.083	2.846		
-1.227	1.325	-1.100	1.809	-0.952	2.215
-0.778	2.538	-0.648	2.835		
-0.933	1.439	-0.759	1.888	-0.550	2.230
-0.340	2.530	-0.220	2.832		
-0.620	1.548	-0.355	1.929	-0.116	2.234
0.101	2.534	0.208	2.837		
-0.252	1.636	0.097	1.948	0.329	2.244
0.542	2.543	0.643	2.842		
0.203	1.674	0.558	1.961	0.778	2.255
0.987	2.551	1.085	2.846		
0.670	1.678	1.013	1.968	1.227	2.261
1.433	2.555	1.531	2.848		
1.127	1.681	1.464	1.972	1.677	2.264
1.881	2.557	1.978	2.849		

BIBLIOGRAPHY

1. R. Hill, The Mathematical Theory of Plasticity, Oxford, (1950).
2. O. Richmond (private communication, 1958) published by M.L. Devenbeck and A.S. Weinstein, "Experimental Investigation of Workhardening Effects in Wedge Flattening with Relation to Non-hardening Theory", *Journal of the Mechanics and Physics of Solids*, 1970, Vol. 18, p. 233 to 243.
3. L. Prandtl and O. Tietjens, Fundamentals of Hydro and Aeromechanics, McGraw-Hill, (1934), p. 71.
4. M.H. Tresca, "Mémoire sur l'écoulement corps solides soumis à de fortes pressions," *Comptes Rendus*, 59:754, (1864).
5. M.H. Tresca, "Sur l'écoulement des corps solides soumis à de fortes pressions", *Comptes Rendus*, 64:809, (1867).
6. M. de Saint-Venant, "Sur l'établissement des équations des mouvements intérieurs opérés dans les corps solides ductiles au delà des limites où l'élasticité pourrait les ramener à leur premier état", *Comptes Rendus*, (March 1870), p. 474.
7. M.M. Levy, "Mémoire sur les équations générales des mouvements intérieurs des corps solides ductiles au delà des limites où l'élasticité pourrait les ramener à leur premier état;" *Comptes Rendus*, 76:1323 (1870).
8. J.J. Guest, "On the Strength of Ductile Materials under Combined Stress", *Phil. Mag. S.5 Vol. 50, No. 302*, p. 69, (July 1900).
9. R. v. Mises, "Mechanik der festen Korper in plastisch-deformablen Zustand", *Goettinger Nachr., Math.-Phys. kl.*, (1913), p. 582-592.
10. M. Hencky, "Uber langsame stationare Stromungen in plastischem Massen mit Rucksicht auf die Vorgange beim Walzen, Pressen und Ziehen von Metallen", *zeitschrift fur Angewandte Mathematik and Mechanik*, Band 5, Heft 2, (April 1925), p. 115-124.
11. A. Nadai, Theory of Flow and Fracture of Solids, McGraw-Hill, 1st Edition, (1931), 2nd Edition, (1950).
12. W. Lode, "Versuche uber den Einfluss der mittleren Hauptspannung auf Fliessen der Metalle, Essen, Kupfer, and Nickel", *Z. Physik* 36:913, (1926).
13. G.I. Taylor and H. Quinney, "The Plastic Distortion of Metals", *Phil. Trans. Roy. Soc. A*, 230 (1931), 323.
14. M. Reiner and D. Abir, Ed.'s, Second-Order Effects in Elasticity, Plasticity, and Fluid Dynamics, Pergamon, (1964), X. Yoshimura and Y. Takenaka, "Strain History Effects in Plastic Deformation of Metals", p. 729-750.

15. Metals Handbook, Vol. 1, 8th Edition, American Society for Metals, (1961).
16. L. Prandtl and Nadai, Zeitschrift für angew. Math. u. Mech., Bd. I, 1921, p. 15 through 28.
17. H. Hencky, "Über einige statisch bestimmte Falle des Gleichgewichts in plastischen Körpern", Zeitschrift für Angewandte Mathematik and Mechanik, Band 3, Heft 4, (August 1923), p. 241-251.
18. Th. Von Karman, Zeits. ang. Math. Mech. 5, (1925), 139.
19. E. Siebel, The Plastic Forming of Metals, Verlag Stahleisen, Dusseldorf, (1932).
20. G. Sachs, Chipless Forming of Metals, Springer Verlag, Berlin (1931).
21. P. Ludwik, Elemente der Technologischen Mechanik, Verlag von Julius Springer, Berlin (1909).
22. B.R. Seth, "Generalized Strain Measure with Applications to Physical Problems", Second-Order Effects in Elasticity, Plasticity, and Fluid Dynamics, MacMillan, (1964), p. 162-172.
23. A.E.H. Love, A Treatise on the Mathematical Theory of Elasticity, (4th Ed.), Dover, p. 8, (1927).
24. A.E. Green and W. Zerna, Theoretical Elasticity, Oxford, (1968).
25. A. Reuss, "Berücksichtigung der elastischen Formänderung in der Plastizitätstheorie," ztschr. f. angew. Math. and Mech., Band 10, Heft 3, (June 1930), p. 266-274.
26. H. Pollaczek-Geiringer, "Beitrag zum Vollständigen Eben Plastizität Problem", Proc. 3rd Int. Cong. App. Mech., Stockholm, 2(1930), 185.
27. E.G. Thomsen and S. Kobayashi, "Indicated Directions of Materials - Forming Research," (1965), p. 211-224.
28. W. Johnson, "Estimation of Upper-Bound Loads for Extrusion and Coining Operations", Proc. Inst. Mech. Eng., (1959)61 173.
29. H. Kudo, "Study of Forging and Extrusion Processes", Part I - Analysis on Plain Strain Problems", Koku Kenkyu-sho Shuko, Tokyo, Japan, (1958), 36.
30. S. Kobayashi, "Upper-Bound Solution of Axi-Symmetric Forming Problem I", ASME Paper, (May 1963).
31. E.G. Thomsen and J.T. Lapley, Jr., "Experimental Stress Determination within a Metal During a Plastic Flow", Proc. Sci. Expt. Stress Anal. 11, No. 2, (1954), 59.

32. P.W. Bridgman, Studies in Large Plastic Flow and Fracture, Harvard University Press, (1964).
33. F.A. Hodierne, "A torsions Test for Use in Metalworking Studies", *Journal of the Institute of Metals*, Vol. 91, (1962-1963), p. 267-273.
34. W.F. Barclay, "Mechanisms of Deformation and Work Hardening in AISI Type 301 Stainless Steel", *ASTM-Special Tech. Publ.* 369, (1965), p. 26-9.
35. J. Datsko, *Material Properties and Manufacturing Processes*, John Wiley & Sons, (1966).
36. R.M. Caddell, A.G. Atkins, "The Influence of Redundant Work When Drawing Rods Through Conical Dies", *ASME Paper No.* 67-WA/Prod-11.
37. A.G. Atkins, R.M. Caddell, "The Incorporation of Work Hardening and Redundant Work in Rod-Drawing Analysis", *Int. J. Mech. Sci.*, Vol.10, (1968), p. 15-28.
38. R.M. Caddell, G. Needham, W. Johnson, "Yield Strength Variation in Ring Rolled Aluminum", *Int. J. Mech. Sci.*, Vol. 10, (1968), p. 749-756.
39. B. Avitzur, "Strain Hardening and Strain-Rate Effects in Plastic Flow Through Conical Converging Dies", *Journal of Engineering for Industry*, p. 556-562, (August 1967).
40. S. Keeler, "Circular Grids by Electrochemical Marking", *Research and Development*, National Steel Corp., Detroit, Mi.
41. MTS Volume I, MTS and the Computing Center; The University of Michigan Computing Center; Ann Arbor, Michigan.
42. MTS Volume II, Plot Description System, The University of Michigan Computing Center, Ann Arbor, Michigan.
43. W. Johnson and P.B. Mellor, Plasticity for Mechanical Engineers, D. Van Nostrand Co., Ltd., (1962).
44. A. Shabaik, S. Kobayashi, E.G. Thomsen, "Application of Potential Flow Theory to Plane-Strain Extrusion", *Journal of Engineering for Industry*, August 1967, p. 503-513.
45. A.H. Shabaik, E.G. Thomsen, "Comparisons of Two Complete Solutions in an Axisymmetric Extrusion with Experiment", *ASME Paper No.* 68-WA/Prod.-12.
46. R.V. Churchill, Complex Variables and Applications, McGraw-Hill Book Co., (1960), 234.
47. L.V. Ahlfors, Complex Analysis, McGraw-Hill, (1966) 170.

48. B. Carnahan, H. Luther, J. Wilkes, Applied Numerical Methods, John Wiley & Sons, (1969).
49. K. Brown and S. Conti, "The Solution of Simultaneous Nonlinear Equations", Proc. of the 22nd Nat. Conf. of A.C.M., p. 111-114.

UNIVERSITY OF MICHIGAN



3 9015 02826 1108